Available online at www.sciencedirect.com
ScienceDirect
Comput. Methods Appl. Mech. Engrg. 343 (2019) 368–406
Computer methods in applied mechanics and engineering
www.elsevier.com/locate/cma

Finite element procedure and simulations for a multiphase phase field approach to martensitic phase transformations at large strains and with interfacial stresses

Anup Basak[a], Valery I. Levitas[a,b,c,*]

[a] Department of Aerospace Engineering, Iowa State University, Ames, IA 50011, USA
[b] Departments of Mechanical Engineering, and Material Science and Engineering, Iowa State University, Ames, IA 50011, USA
[c] Division of Materials Science and Engineering, Ames Laboratory, Ames, IA 50011, USA

Received 30 April 2018; received in revised form 30 July 2018; accepted 7 August 2018
Available online 16 August 2018

Highlights

- Presented a rigorous FEM for a multiphase phase field method for martensitic transformation.
- Derived consistent tangent modulus due to elastic and structural stresses.
- Studied simple shear problem with single variant and two variant-based twinning problem.
- Obtained complex microstructures under nanoindentation.

Abstract

A detailed finite element procedure for a new phase field approach (Basak and Levitas, 2018) to temperature- and stress induced multivariant martensitic transformations at large strains and with interfacial stresses is developed. A system with austenite and N martensitic variants is considered. $N + 1$ order parameters related to the transformation strains are used, one of which describes the austenite↔martensite transformation; the other N order parameters describe N martensitic variants. Evolution of the order parameters is governed by coupled Ginzburg–Landau and mechanics equations. Assuming a non-monolithic strategy for solving the governing equations by using Newton's iterative method, a weak formulation with emphasis on the derivation of the tangent modulus has been presented. Notably, the fourth order tangent modulus for the equilibrium equations has a contribution not only from the elastic stresses but also from the structural interfacial stresses, which appears here for the first time. A second order backward difference scheme is used to discretize the time derivative in the Ginzburg–Landau equations. An adaptive time stepping is considered. A finite element code has been developed within an open source package deal.II for a system with austenite and two martensitic variants and used to solve three problems: (i) simple shear deformation of a rectangular parallelepiped with evolution of austenite and single martensitic variant; (ii) twinning in martensite and the effect of sample size on the twinned microstructures; (iii) a rectangular block under nanoindentation. The results for the first two problems describe the well-known analytical solutions. Two kinematic models (KMs) for the transformation deformation gradient tensor are used and the corresponding results are compared: KM-I represents a linear transformation rule in the Bain tensors and KM-II is an exponential-logarithmic type of transformation rule in the Bain tensors. The algorithm can naturally be extended for the study of phase transformations in

* Corresponding author at: Department of Aerospace Engineering, Iowa State University, Ames, IA 50011, USA.
E-mail address: vlevitas@iastate.edu (V.I. Levitas).

https://doi.org/10.1016/j.cma.2018.08.006

multiphase solids, solidification, diffusive phase transitions, interaction between phase transformations and plasticity and/or fracture, etc.

Keywords: Martensitic transformations; Multiphase phase field approach; Finite element method; Twinning; Large strains; Interfacial stresses

1. Introduction

The phase field (PF) approach to phase transformations (PTs) dates back to Landau, who introduced the order parameters related to the symmetry of the phases, and also to Ginzburg, who introduced a gradient-based interfacial energy (see e.g. [1] for a review). This approach is popularly known as the Ginzburg–Landau theory, which is also similar to the Allen–Cahn approach [2]. The PF approaches of the Ginzburg–Landau type have been extensively used to study a wide range of physical problems such as solid↔melt transitions (see [3–10] and the references therein), grain growth (see [11–16] and the references therein), evolution of domain structures (see e.g. [12,17,18]), martensitic transformations (MTs) [19–34], and interaction between MTs and plasticity [35–37]. Our focus in this paper will be mainly on MT, which is a diffusion-less, displacive process with dominating shear deformation. Such transformation yields the shape memory effect, ferroelectricity, and magnetoelasticity in various alloys [38,39]. Complex microstructures are formed within the materials undergoing MTs, which usually include laminated structures consisting of martensitic (M) plates of alternative variants called twinned martensite, as well as twins within twins, wedge, etc. [38,40], which usually consist of austenite (A) and all possible martensitic variants M_i ($i = 1, 2, \ldots, N$, and N is the number of variants).

One should also note that all of the A-M and variant–variant interfaces possess finite energy and are subjected to biaxial stresses, which act in a plane tangential to the interface [41]; the schematic is shown in Fig. 1 when the elastic stresses are neglected. Such stresses play a very important role in the nucleation and propagation of the interfaces [42,43]. According to the Shuttleworth equation, the total interfacial stress tensor $\bar{\boldsymbol{\sigma}} = \bar{\boldsymbol{\sigma}}_{st} + \bar{\boldsymbol{\sigma}}_{e} = \gamma(\boldsymbol{I} - \boldsymbol{n} \otimes \boldsymbol{n}) + \partial\gamma/\partial\bar{\boldsymbol{\varepsilon}}$ (a tangential tensor) is composed of an elastic part $\bar{\boldsymbol{\sigma}}_{e} = \partial\gamma/\partial\bar{\boldsymbol{\varepsilon}}$ that depends on the strain tensor within the interface, $\bar{\boldsymbol{\varepsilon}}$, and a structural part, $\bar{\boldsymbol{\sigma}}_{st} = \gamma(\boldsymbol{I} - \boldsymbol{n} \otimes \boldsymbol{n})$, where $\boldsymbol{n}$ is the unit normal to the interface, γ is the interfacial energy, $\boldsymbol{I}$ is the identity tensor, and $\otimes$ denotes the dyadic product. Within the phase field models where the interfaces are finite-width regions, the elastic part of the interfacial stresses arises naturally due to the elastic strains. To introduce the other part, i.e. the structural stress tensor, Levitas and coworkers [20,21,29,44] multiplied the double-well barrier energy and the gradient energy in the Helmholtz's free energy by the determinant of the total deformation gradient tensor, and considered the gradient of the order parameters in the deformed configuration. When the structural stresses are considered, the tangent modulus for the mechanical equilibrium equations would obviously have contributions from both the elastic response and the structural stresses in both finite strain and small strain models [21,45]. The structural stresses obviously depend on nontraditional mechanics parameters (gradient of the order parameters in the deformed configuration). We are not aware of any algorithmic treatment for the models with structural interfacial stresses as it is done in the current paper. Note that it is very important to have the correct expressions for the tangent modulus for both mechanics and PF problems, at least for a good convergence within the Newton's iterations.

All the PF approaches introduce order parameters which describe the phases. The interfaces are of finite width and have well-defined structures. The volume fraction (e.g. [4,24,26,46]) or transformation strain-based order parameters (e.g. [30,32]) are usually used. In this paper, the transformation strain-related order parameters, which describe the change in symmetries (the PT process) in a continuous way, are considered. A system of Ginzburg–Landau equations governs the evolution of the order parameters, which are highly-nonlinear parabolic partial differential equations (PDEs). When the PT phenomenon is stress- and temperature-induced, the mechanical equilibrium equations also play a non-trivial role and are coupled to the system of Ginzburg–Landau equations.

The finite element method (FEM) has been used in this paper to solve the coupled PF and equilibrium equations. FEM is preferred over the finite difference method (see e.g. [3,7,47], where this approach was used), as FEM can efficiently handle any arbitrary domain shape, whereas the other method cannot. Pioneering work in the simulations of PF equations for MTs was done by Khachaturyan and coworkers [32,33], who used the Fourier Transform method

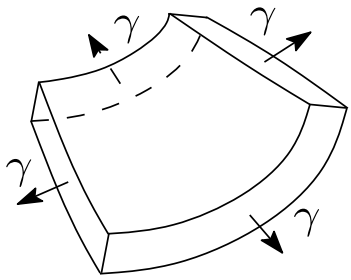

Fig. 1. Schematic of an arbitrary finite-width interface subjected to biaxial interfacial structural stresses, where γ is the magnitude of the stress acting in the tangent plane of the interface. The elastic interfacial stresses are not shown here.

to numerically solve the coupled PDEs. Other groups of researchers used similar approaches; see e.g. Roytburd and coworkers [18], Chen and coworkers [12,34], Lei et al. [22], Vidyasagar et al. [48], Kundin et al. [37] etc. The spectral methods are much faster, but they can only handle problems with periodic boundary conditions. Hence, the Fourier method cannot be used for models which consider the surface effects; see e.g. [44], where FEM was used.

In solving the PF equations for MTs, FEM has been used by a limited number of groups, e.g. Levitas and coworkers [20,21,44,49–51], Clayton and Knap [27,28], Stupkiewicz and coworkers [25,26], Hildebrand and Miehe [24], She at al. [52], Paranjape et al. [35]. Finite strain theories were considered in [24–28,50,51], but the rest of the works dealt with small strain theories. A detailed FE formalism for stress- and temperature-induced MTs at finite strains and with interfacial stresses is still missing. Even a coherent FE procedure for the models considering small strain and/or neglecting the interfacial stresses is not yet available, to the best of our knowledge.

Our *goal* in this paper is to present a rigorous FE formalism for the coupled PF equations and the mechanics equations related to the model developed in [45] for multivariant MTs induced by stresses and temperature at finite strains and with interfacial stresses. To illustrate the formalism, we solve some problems showing complex microstructure evolutions and compare the numerical results for two problems with the known analytical solutions. Formulations for a system with A and N martensitic variants have been presented. The weak forms for the equilibrium equation and the Ginzburg–Landau equations, where a non-monolithic approach is used, are established using the variational method. The time derivative in the PF equations is discretized mainly by using a backward difference scheme of order two (BDF2). The mechanics problem and the PF equations have been solved using the Newton's iterative methods, for which the weak forms are linearized and the corresponding tangent moduli for the mechanics and PF problems are obtained. The tangent modulus related to the mechanics problem is a fourth order tensor that is decomposed into two parts, which are related to the elastic and structural stresses, respectively. An adaptive time stepping has been used to integrate the PF equations. Based on the FE formulation, we have developed an FE code in an open source deal.II and solved the following three problems: (i) Evolution of microstructure in a system with A and single M variant in a rectangular parallelepiped. (ii) Twinning in a system with A and two variants M_1 and M_2 under the generalized plane strain condition. The effect of sample size on the twinned microstructure is also studied. (iii) Nanoindentation of a rectangular sample under plane stress condition. Two different kinematic models (KMs) for the transformation deformation gradient tensor $\boldsymbol{F}_t$ are considered: in KM-I, $\boldsymbol{F}_t$ is taken as a linear combination of the Bain strains, which are multiplied by the interpolations functions [29,31], and in KM-II, we take $\boldsymbol{F}_t$ as the exponential of a linear combination of the natural logarithm of the Bain tensors multiplied by the interpolation functions [25,26]. For each problem, the results for both KM-I and KM-II are presented and compared. We have also compared the elastic stresses within the twin boundaries for these two KMs. We report that the elastic stress component in the longitudinal direction of the twin boundaries is much larger for KM-II than KM-I, which is in agreement with our recent analytical and numerical study on interfacial stresses in [53]. The performance of our adaptive time stepping scheme is also analyzed.

The content of the paper is as follows: the system of governing equations is listed in Section 2; the weak forms of the governing PDEs and their linearizations are presented in Section 3; FE discretization details and the computational algorithm are given in Section 4; various material parameters are derived and listed in Section 5; Section 6 presents the numerical examples; finally, the conclusions of the study are drawn in Section 7.

Notation. We denote the inner product and multiplication between two second order tensors as $\boldsymbol{A} : \boldsymbol{B} = A_{ab}B_{ba}$ and $(\boldsymbol{A} \cdot \boldsymbol{B})_{ab} = A_{ac}B_{cb}$, respectively, where the repeated indices denote Einstein's summation, and A_{ab} and B_{ab} are

the components of the tensors in a right-handed orthonormal Cartesian basis $\{\boldsymbol{e}_1, \boldsymbol{e}_2, \boldsymbol{e}_3\}$. The Euclidean norm of $\boldsymbol{A}$ is denoted as $|\boldsymbol{A}| = \sqrt{\boldsymbol{A} : \boldsymbol{A}^T}$; $\boldsymbol{I}$ denotes the second order identity tensor; δ_{ab} denotes the Kronecker delta; $\boldsymbol{A}^{-1}$, $\boldsymbol{A}^T$, $det\,\boldsymbol{A}$, $tr\,\boldsymbol{A}$, $sym(\boldsymbol{A})$, and $skew(\boldsymbol{A})$ denote the inversion, transposition, determinant, trace, symmetric part, and skew part of $\boldsymbol{A}$, respectively. The symbols ∇_0 and ∇ represent the gradient operators in the reference (undeformed) Ω_0 and current (deformed) Ω configurations, respectively; $\nabla_0^2 := \nabla_0 \cdot \nabla_0$ and $\nabla^2 := \nabla \cdot \nabla$ are the Laplacian operators in Ω_0 and Ω, respectively. The symbol := stands for equality by definition.

2. System of coupled mechanics and phase field equations

Recently, Basak and Levitas [45] developed a novel multiphase phase field model for studying stress and temperature-induced MTs for a system with austenite and N martensitic variants considering $N+1$ order parameters $\eta_0, \eta_1, \ldots, \eta_i, \eta_j, \ldots, \eta_N$. The order parameter η_0 describes $\mathsf{A} \leftrightarrow \mathsf{M}$ transformations such that $\eta_0 = 0$ in A and $\eta_0 = 1$ in M. The order parameter η_i (for $i = 1, \ldots, N$) describes the variant M_i such that $\eta_i = 1$ in M_i and $\eta_i = 0$ in M_j for all $j \neq i$. Also, $\eta_1, \ldots, \eta_N$ satisfy the constraint (see [45] for details)

$$\sum_{i=1}^{N} \eta_i = 1. \tag{2.1}$$

In this section we enlist the system of coupled elasticity and phase field equations for an N-variant system; see [45] for their derivation. The reference, stress-relaxed intermediate, and current configurations are denoted by Ω_0, Ω_t, and Ω, respectively. The external boundaries in Ω_0 and Ω are denoted by S_0 and S, respectively. We designate the traction boundary (Neumann boundary) in Ω_0 by S_{0T} and the displacement boundary (Dirichlet boundary) by S_{0u}, such that $S_0 = S_{0u} \cup S_{0T}$. Similarly, for the PF equations $S_0 = S_{0\eta_k} \cup S_{0T_k}$ for all $k = 0, 1, \ldots, N$, where $S_{0\eta_k}$ is the Dirichlet boundary where η_k is specified, and S_{0T_k} is the Neumann boundary corresponding to the order parameter η_k.

2.1. Kinematics

We denote the position vector of a particle in Ω by $\boldsymbol{r}(\boldsymbol{r}_0, t)$, where $\boldsymbol{r} = \boldsymbol{r}_0 + \boldsymbol{u}(\boldsymbol{r}_0, t)$, $\boldsymbol{r}_0$ is the position vector in Ω_0, $\boldsymbol{u}$ is the displacement vector, and t denotes time. We assume that both $\boldsymbol{u}$, and hence, $\boldsymbol{r}$ are sufficiently smooth functions of $\boldsymbol{r}_0$ and t. The total deformation gradient $\boldsymbol{F}$ is decomposed into [29]

$$\boldsymbol{F} := \nabla_0 \boldsymbol{r} = \boldsymbol{F}_e \cdot \boldsymbol{F}_t = \boldsymbol{V}_e \cdot \boldsymbol{R} \cdot \boldsymbol{U}_t, \tag{2.2}$$

where the subscripts e and t denote elastic and transformational parts, respectively; $\boldsymbol{F}_e = \boldsymbol{V}_e \cdot \boldsymbol{R}_e$ and $\boldsymbol{F}_t = \boldsymbol{R}_t \cdot \boldsymbol{U}_t$ are, respectively, the elastic and transformational parts of $\boldsymbol{F}$; $\boldsymbol{U}_t$ is the right transformation stretch tensor (symmetric); $\boldsymbol{V}_e$ is the left elastic stretch tensor (symmetric); $\boldsymbol{R}_t$ and $\boldsymbol{R}_e$ are the rotation tensors; and $\boldsymbol{R} = \boldsymbol{R}_e \cdot \boldsymbol{R}_t$ is the lattice rotation tensor. We also define $J = det\,\boldsymbol{F} := dV/dV_0$, $J_t = det\,\boldsymbol{F}_t := dV_t/dV_0$, and $J_e = det\,\boldsymbol{F}_e := dV/dV_t$, where dV_0, dV_t, and dV are infinitesimal volume elements in Ω_0, Ω_t, and Ω, respectively. Hence by Eq. (2.2), $J = J_t J_e$. The Lagrangian total and elastic strains are defined as

$$\boldsymbol{E} := 0.5(\boldsymbol{C} - \boldsymbol{I}), \quad \text{and} \quad \boldsymbol{E}_e := 0.5(\boldsymbol{C}_e - \boldsymbol{I}), \tag{2.3}$$

respectively, where $\boldsymbol{C} = \boldsymbol{F}^T \cdot \boldsymbol{F}$ and $\boldsymbol{C}_e = \boldsymbol{F}_e^T \cdot \boldsymbol{F}_e$ are the right Cauchy–Green total strain and elastic strain tensors, respectively. Also, the Eulerian total and elastic strain tensors are $\boldsymbol{b} = 0.5(\boldsymbol{B} - \boldsymbol{I})$ and $\boldsymbol{b}_e = 0.5(\boldsymbol{B}_e - \boldsymbol{I})$, respectively, where $\boldsymbol{B} = \boldsymbol{F} \cdot \boldsymbol{F}^T = \boldsymbol{V}^2$ and $\boldsymbol{B}_e = \boldsymbol{F}_e \cdot \boldsymbol{F}_e^T = \boldsymbol{V}_e^2$ are the left Cauchy–Green total strain and elastic strain tensors, respectively. Note that $\boldsymbol{V} = \sqrt{\boldsymbol{B}}$ is the left total stretch tensor.

Kinematic models for $\boldsymbol{F}_t$. Two KMs for the transformation deformation gradient tensor $\boldsymbol{F}_t$ have been assumed. In KM-I we express $\boldsymbol{F}_t$ as (see [45] for details)

$$\text{for KM-I:} \qquad \boldsymbol{F}_t = \boldsymbol{U}_t = \boldsymbol{I} + \sum_{i=1}^{N} \boldsymbol{\varepsilon}_{ti} \varphi(a_\varepsilon, \eta_0) \phi_i(\eta_i); \tag{2.4}$$

where $\boldsymbol{\varepsilon}_{ti} = \boldsymbol{U}_{ti} - \boldsymbol{I}$ and $\boldsymbol{U}_{ti}$ are the Bain strain tensor and Bain stretch tensor, respectively, for M_i. The interpolation functions $\varphi(a_\varepsilon, \eta_0)$ and $\phi_i(\eta_i)$ are taken as [45]

$$\varphi(a_\varepsilon, \eta_0) = a_\varepsilon \eta_0^2 + (4 - 2a_\varepsilon)\eta_0^3 + (a_\varepsilon - 3)\eta_0^4, \quad \text{and} \quad \phi_i(\eta_i) = \eta_i^2(3 - 2\eta_i), \tag{2.5}$$

respectively, and $0 \leq a_\varepsilon \leq 6$ is a constant parameter. The interpolation function $\varphi(a_\varepsilon, \eta_0)$ satisfies the conditions $\varphi(a_\varepsilon, 0) = 0$, $\varphi(a_\varepsilon, 1) = 1$, and $\frac{\partial \varphi(a_\varepsilon,0)}{\partial \eta_0} = \frac{\partial \varphi(a_\varepsilon,1)}{\partial \eta_0} = 0$; and ϕ_i satisfies $\phi_i(0) = 0$, $\phi_i(1) = 1$, and $\frac{\partial \phi_i(\eta_i=0)}{\partial \eta_i} = \frac{\partial \phi_i(\eta_i=1)}{\partial \eta_i} = 0$ for all $i = 1, 2, \ldots, N$. This KM (Eq. (2.4)) was introduced and used in [20,21,29,31,45,50,51]. It should be noted that although the specific volumes of the variants are the same, each variant $\leftrightarrow$ variant transformation path, i.e. $\mathsf{M}_i \leftrightarrow \mathsf{M}_j$ for all $i \neq j$, is not isochoric in KM-I [45].

In the other model KM-II, we take $\boldsymbol{F}_t$ as (see [45] for details)

$$\text{for KM-II:} \qquad \boldsymbol{F}_t = \boldsymbol{U}_t = \exp\left[\varphi(a_\varepsilon, \eta_0) \sum_{i=1}^{N} \phi_i(\eta_i) \ln \boldsymbol{U}_{ti}\right]. \tag{2.6}$$

The definitions and properties of the exponential and logarithm of a second order tensor can be found in, e.g., [54,55]. It was proved in [45] that each $\mathsf{M}_i \leftrightarrow \mathsf{M}_j$ transformation (for all $i \neq j$) given by Eq. (2.6) is isochoric for the entire transformation path.

Note that in KM-I and KM-II, $\boldsymbol{F}_t$ are symmetric and taken to be identical to the symmetric tensor $\boldsymbol{U}_t$ and $\boldsymbol{R}_t$ is assumed to be $\boldsymbol{R}_t = \boldsymbol{I}$. There are cases where the transformation deformation gradient can be nonsymmetric, such as the simple shear-based kinematic model considered in [45,53]. Thus to derive a general FE formulation which is applicable for both symmetric and nonsymmetric $\boldsymbol{F}_t$, we would continue to designate the transformation rules (2.4) and (2.6) for KM-I and KM-II as $\boldsymbol{F}_t$.

2.2. Free energy

We consider the Helmholtz free energy per unit mass of the body in the following form [29,45]:

$$\begin{aligned}\psi(\boldsymbol{F}, \theta, \eta_0, \eta_i, \nabla\eta_0, \nabla\eta_i) = \frac{J_t}{\rho_0}\psi_e(\boldsymbol{F}_e, \theta, \eta_0, \eta_i) + J\breve{\psi}^\theta(\theta, \eta_0, \eta_i) + \tilde{\psi}^\theta(\theta, \eta_0, \eta_i) \\ + \psi_p(\eta_0, \eta_i) + J\psi^\nabla(\eta_0, \nabla\eta_0, \nabla\eta_i)\end{aligned} \tag{2.7}$$

for all $i = 1, 2, \ldots, N$, where ψ^e is the elastic strain energy per unit volume of Ω_t, $\breve{\psi}^\theta$ is the barrier energy related to $\mathsf{A} \leftrightarrow \mathsf{M}$ and all the $\mathsf{M}_i \leftrightarrow \mathsf{M}_j$ transformations, $\tilde{\psi}^\theta$ is the thermal energy, ψ^∇ is the interfacial energy, and ψ^p penalizes various junctions between A and the variants. It should be noted that in Eq. (2.7) the barrier energy and the gradient energy are multiplied by J and the gradients of η_0 and η_i are expressed in the deformed configuration. This yields the desired form of the structural stresses (here given by Eqs. (2.17) and (2.18)) as discussed in Section 1; see [29] for further details. The material properties at each material point are determined using [45]

$$M(\eta_0, \eta_i, \theta, \boldsymbol{F}) = M_0(1 - \varphi(a, \eta_0)) + \varphi(a, \eta_0) \sum_{i=1}^{N} M_i \phi_i(\eta_i), \tag{2.8}$$

where M_0 and M_i are the properties of the phases A and M_i, respectively, $\varphi(a, \eta_0)$ is an interpolation function and has the same functional form of $\varphi(a_\varepsilon, \eta_0)$ given by Eq. $(2.5)_1$ when a_ε is replaced by the constant parameter a. Note that $\varphi(a, \eta_0)$ also satisfies the conditions similar to those of $\varphi(a_\varepsilon, \eta_0)$ discussed above. Evidently, the interpolation Eq. (2.8) yields the property of the corresponding phase (A or M_i) when the appropriate values of the order parameters are assigned.

The explicit form of all of the energies is [45]

$$\psi_e = \frac{1}{2}\boldsymbol{E}_e : \hat{\boldsymbol{\mathcal{C}}}_e(\eta_0, \eta_i) : \boldsymbol{E}_e, \quad \text{where } \hat{\boldsymbol{\mathcal{C}}}_e(\eta_0, \eta_i) = (1 - \varphi(a, \eta_0))\hat{\boldsymbol{\mathcal{C}}}_{(e)0} + \varphi(a, \eta_0) \sum_{i=1}^{N} \phi_i(\eta_i)\hat{\boldsymbol{\mathcal{C}}}_{(e)i}; \tag{2.9}$$

$$\breve{\psi}^\theta = [A_{0M}(\theta) + (a_\theta - 3)\Delta\psi^\theta(\theta)]\,\eta_0^2(1 - \eta_0)^2 + \tilde{A}\varphi(a_b, \eta_0) \sum_{i=1}^{N-1} \sum_{j=i+1}^{N} \eta_i^2\,\eta_j^2; \tag{2.10}$$

$$\tilde{\psi}^\theta = \psi_0^\theta(\theta) + \eta_0^2(3 - 2\eta_0)\,\Delta\psi^\theta(\theta) \quad \text{where } \Delta\psi^\theta = -\Delta s_{0M}(\theta - \theta_e); \tag{2.11}$$

$$\psi_p = \sum_{i=1}^{N-1} \sum_{j=i+1}^{N} K_{ij}(\eta_i + \eta_j - 1)^2\eta_i^2\eta_j^2 + [1 - \varphi(a_K, \eta_0)] \sum_{i=1}^{N-1} \sum_{j=i+1}^{N} K_{0ij}\eta_0^2\eta_i^2\eta_j^2$$

$$+\sum_{i=1}^{N-2}\sum_{j=i+1}^{N-1}\sum_{k=j+1}^{N} K_{ijk}\eta_i^2\eta_j^2\eta_k^2 +$$
$$[1-\varphi(a_K,\eta_0)]\sum_{i=1}^{N-2}\sum_{j=i+1}^{N-1}\sum_{k=j+1}^{N} K_{0ijk}\eta_0^2\eta_i^2\eta_j^2\eta_k^2 + \sum_{i=1}^{N-3}\sum_{j=i+1}^{N-2}\sum_{k=j+1}^{N-1}\sum_{l=k+1}^{N} K_{ijkl}\eta_i^2\eta_j^2\eta_k^2\eta_l^2, \quad \text{where}$$

$$K_{ii} = K_{0ii} = K_{iji} = K_{iik} = K_{0iji} = K_{0iik} = K_{ijil} = K_{iikl} = K_{ijjl} = K_{ijki} = K_{ijkk} = 0; \tag{2.12}$$

$$\psi^{\nabla} = \frac{\beta_{0M}}{2\rho_0}|\nabla\eta_0|^2 + \frac{1}{8\rho_0}\tilde{\varphi}(\eta_0,a_\beta,a_c)\sum_{i=1}^{N-1}\sum_{j=i+1}^{N}\beta_{ij}\left(|\nabla\eta_i|^2 - 2\nabla\eta_i\cdot\nabla\eta_j + |\nabla\eta_j|^2\right),$$
$$\text{where } \beta_{ii} = 0, \tag{2.13}$$

$$\tilde{\varphi}(a_\beta,a_c,\eta_0) = a_c + a_\beta\eta_0^2 - 2[a_\beta - 2(1-a_c)]\eta_0^3 + [a_\beta - 3(1-a_c)]\eta_0^4. \tag{2.14}$$

All of the symbols used in Eqs. (2.9) to (2.14) are now defined. $\hat{\boldsymbol{\mathcal{C}}}_e(\eta_0,\eta_i)$ is the fourth-order elastic modulus tensor for a material point; $\hat{\boldsymbol{\mathcal{C}}}_{(e)0}$ and $\hat{\boldsymbol{\mathcal{C}}}_{(e)i}$ are the elastic modulus tensors of A_{0M} and M_i, respectively; $A_{0M} > 0$ is the barrier height between A and M; $\tilde{A} > 0$ is the barrier height between M_i and M_j for all $i \neq j$; ψ_0^θ is the thermal energy of A; $\Delta\psi^\theta = \psi_M^\theta - \psi_0^\theta$ is the thermal energy difference between M and A; $\Delta s_{0M} = s_M - s_0$ is the change in entropy due to A to M transformation (s_0 and s_M denoting the entropy of A and M, respectively); $\theta > 0$ is the absolute temperature; θ_e is the thermodynamic equilibrium temperature between A and M; $K_{ij} \geq 0$ is a controlling parameter for penalizing the deviation of the transformation path (i.e. $\mathsf{M}_j \leftrightarrow \mathsf{M}_i$ path) from the straight line $\eta_j + \eta_i = 1$ for all $\eta_k = 0$ and $k \neq j, i$; $K_{0ij} \geq 0$, $K_{ijk} \geq 0$, $K_{0ijk} \geq 0$, and $K_{ijkl} \geq 0$ are the constant coefficients for penalizing the junctions between A-M_i-M_j, M_i-M_j-M_k, A-M_i-M_j-M_k, and M_i-M_j-M_k-M_l, respectively; $\beta_{0M} > 0$ and $\beta_{ij} > 0$ are the energy coefficients for A-M and M_i-M_j interfaces, respectively; ρ_0 is the density of the solid in Ω_0; and a_b, a_K, a_β, a_c are the material parameters.

2.3. Mechanical equilibrium equations and stresses

Neglecting the body forces and inertia we write the mechanical equilibrium equations as [29,45]

$$\nabla_0\cdot\boldsymbol{P} = \boldsymbol{0} \quad \text{in } \Omega_0, \quad \text{or} \quad \nabla\cdot\boldsymbol{\sigma} = \boldsymbol{0} \quad \text{in } \Omega, \tag{2.15}$$

where $\boldsymbol{P}$ is the total first Piola–Kirchhoff stress tensor and $\boldsymbol{\sigma}$ is the total Cauchy stress tensor. These tensors are decomposed into their elastic and structural parts [45] $\boldsymbol{P} = \boldsymbol{P}_e + \boldsymbol{P}_{st}$ and $\boldsymbol{\sigma} = \boldsymbol{\sigma}_e + \boldsymbol{\sigma}_{st}$. Here, the subscripts e and st denote elastic and structural parts, respectively. In general, the elastic first Piola–Kirchhoff and Cauchy stresses are given by [29,45]

$$\boldsymbol{P}_e = J_t\boldsymbol{F}_e\cdot\hat{\boldsymbol{S}}_e\cdot\boldsymbol{F}_t^{-T}; \qquad \boldsymbol{\sigma}_e = J_e^{-1}\boldsymbol{F}_e\cdot\hat{\boldsymbol{S}}_e\cdot\boldsymbol{F}_e^T, \quad \text{where } \hat{\boldsymbol{S}}_e = \frac{\partial\psi_e(\boldsymbol{E}_e)}{\partial\boldsymbol{E}_e}. \tag{2.16}$$

For isotropic elastic response, $\boldsymbol{P}_e$ and $\boldsymbol{\sigma}_e$ can alternatively be expressed as $\boldsymbol{P}_e = J_t\boldsymbol{V}_e^2\cdot\frac{\partial\psi_e(\boldsymbol{b}_e)}{\partial\boldsymbol{b}_e}\cdot\boldsymbol{F}^{-T}$ and $\boldsymbol{\sigma}_e = J_e^{-1}\boldsymbol{V}_e^2\cdot\frac{\partial\psi_e(\boldsymbol{b}_e)}{\partial\boldsymbol{b}_e}$, respectively. The first Piola–Kirchhoff structural stress tensor is [45]

$$\boldsymbol{P}_{st} = J\rho_0(\breve{\psi}^\theta + \psi^{\nabla})\boldsymbol{F}^{-T} - J\beta_{0M}\nabla\eta_0\otimes\nabla\eta_0\cdot\boldsymbol{F}^{-T} - J\tilde{\varphi}\sum_{i=1}^{N}\sum_{j=1}^{N}\frac{\beta_{ij}}{4}\nabla\eta_i\otimes(\nabla\eta_i - \nabla\eta_j)\cdot\boldsymbol{F}^{-T}. \tag{2.17}$$

Noticing that [45] $\beta_{ij} = \beta_{ji}$ and $\beta_{ii} = 0$ (for all $i \neq j$), the structural part of $\boldsymbol{\sigma}$ is expressed as

$$\boldsymbol{\sigma}_{st} = \rho_0(\breve{\psi}^\theta + \psi^{\nabla})\boldsymbol{I} - \beta_{0M}\nabla\eta_0\otimes\nabla\eta_0 - \tilde{\varphi}\sum_{i=1}^{N-1}\sum_{j=i+1}^{N}\frac{\beta_{ij}}{4}[\nabla\eta_i\otimes\nabla\eta_i + \nabla\eta_j\otimes\nabla\eta_j$$
$$- 2sym(\nabla\eta_i\otimes\nabla\eta_j)]. \tag{2.18}$$

When A-M and M_i-M_j interfaces are considered, Eq. (2.18) simplifies as

$$\boldsymbol{\sigma}_{st} = \sigma_{(st)0M}(\boldsymbol{I} - \boldsymbol{k}_{0M}\otimes\boldsymbol{k}_{0M}), \quad \text{and} \quad \boldsymbol{\sigma}_{st} = \sigma_{(st)ij}(\boldsymbol{I} - \boldsymbol{k}_{ij}\otimes\boldsymbol{k}_{ij}), \quad \text{respectively, where}$$

$$\sigma_{(st)0M} = \beta_{0M}|\nabla\eta_0|^2 = 2\rho_0\breve{\psi}^{\theta},\ \sigma_{(st)ij} = \beta_{ij}|\nabla\eta_i|^2 = 2\rho_0\breve{\psi}^{\theta},\ \boldsymbol{k}_{0M} = \frac{\nabla\eta_0}{|\nabla\eta_0|},\ \text{ and } \boldsymbol{k}_{ij} = \frac{\nabla\eta_i}{|\nabla\eta_i|}, \tag{2.19}$$

i.e. for each interface, Eq. (2.18) yields biaxial tension where the resultant force is equal to the interface energy γ (see [29] for the proof), similar to that in the sharp interface theory [41].

2.4. Ginzburg–Landau equations

The Ginzburg–Landau equations for all $N+1$ order parameters are (see [45] for the derivation)

$$\dot{\eta}_0 = L_{0M}X_0, \quad \text{and} \quad \dot{\eta}_i = \sum_{j=1,\neq i}^{N} L_{ij}(X_i - X_j) \quad \text{for } i = 1, 2, \ldots, N, \tag{2.20}$$

where L_{0M} and L_{ij} are the kinetic coefficients for A-M and M_i-M_j interfaces, respectively, and X_0 and X_i are the conjugate forces for the evolution of the order parameters η_0 and η_i, respectively:

$$\begin{aligned}
X_0 = {} & \left(\boldsymbol{P}_e^T\cdot\boldsymbol{F} - J_t\psi_e\boldsymbol{I}\right) : \boldsymbol{F}_t^{-1}\cdot\frac{\partial\boldsymbol{F}_t}{\partial\eta_0} - J_t\left.\frac{\partial\psi_e}{\partial\eta_0}\right|_{\boldsymbol{F}_e} - \rho_0(6\eta_0 - 6\eta_0^2)\Delta\psi^{\theta} \\
& - J\rho_0\tilde{A}\sum_{i=1}^{N-1}\sum_{j=i+1}^{N}\eta_i^2\eta_j^2\frac{\partial\varphi(a_b,\eta_0)}{\partial\eta_0} - \\
& J\rho_0[A_{0M}(\theta) + (a_\theta - 3)\Delta\psi^{\theta}(\theta)](2\eta_0 - 6\eta_0^2 + 4\eta_0^3) - \frac{J}{8}\frac{\partial\tilde{\varphi}(a_\beta,a_c,\eta_0)}{\partial\eta_0}\sum_{i=1}^{N-1}\sum_{j=i+1}^{N}\beta_{ij}|\nabla\eta_i - \nabla\eta_j|^2 - \\
& \rho_0\left(\sum_{i=1}^{N-1}\sum_{j=i+1}^{N}K_{0ij}\eta_i^2\eta_j^2 + \sum_{i=1}^{N-2}\sum_{j=i+1}^{N-1}\sum_{k=j+1}^{N}K_{0ijk}\eta_i^2\eta_j^2\eta_k^2\right) \\
& \times\left[2(1-\varphi(a_K,\eta_0))\eta_0 - \frac{\partial\varphi(a_K,\eta_0)}{\partial\eta_0}\eta_0^2\right] + \\
& \nabla_0\cdot\left(J\beta_{0M}\boldsymbol{F}^{-1}\cdot\nabla\eta_0\right);
\end{aligned} \tag{2.21}$$

$$\begin{aligned}
X_i = {} & \left(\boldsymbol{P}_e^T\cdot\boldsymbol{F} - J_t\psi_e\boldsymbol{I}\right) : \boldsymbol{F}_t^{-1}\cdot\frac{\partial\boldsymbol{F}_t}{\partial\eta_i} - J_t\left.\frac{\partial\psi_e}{\partial\eta_i}\right|_{\boldsymbol{F}_e} \\
& - 2J\rho_0\tilde{A}\sum_{j=1,\neq i}^{N}\eta_i\eta_j^2\varphi(a_b,\eta_0) - 2\rho_0\sum_{j=1}^{N}K_{ij}(\eta_i + \eta_j - 1)\times \\
& (2\eta_i + \eta_j - 1)\eta_j^2\eta_i - 2\rho_0\left(\sum_{j=1}^{N}K_{0ij}\eta_j^2 + \sum_{j=1}^{N-1}\sum_{k=j+1}^{N}K_{0ijk}\eta_j^2\eta_k^2\right) \\
& \times\eta_0^2\eta_i(1-\varphi(a_K,\eta_0)) - 2\rho_0\sum_{j=1}^{N-1}\sum_{k=j+1}^{N}K_{ijk}\times \\
& \eta_i\eta_j^2\eta_k^2 - 2\rho_0\sum_{j=1}^{N-2}\sum_{k=j+1}^{N-1}\sum_{l=k+1}^{N}K_{ijkl}\eta_i\eta_j^2\eta_k^2\eta_l^2 + \nabla_0\cdot\left(\tilde{\varphi}(a_\beta,a_c,\eta_0)J\sum_{j=1}^{N}\frac{\beta_{ij}}{4}\boldsymbol{F}^{-1}\cdot(\nabla\eta_i - \nabla\eta_j)\right) \\
& \text{for all } i = 1, 2, 3, \ldots, N.
\end{aligned} \tag{2.22}$$

Note that X_0 and X_i, which are given by Eqs. (2.21) and (2.22), respectively, are the functions of all of the $N+1$ order parameters $\eta_0, \eta_1, \eta_2, \ldots, \eta_N$. Because the N order parameters $\eta_1, \ldots, \eta_N$ are related through the constraint (2.1), out of the N Ginzburg–Landau equations in Eq. $(2.20)_2$, only $N-1$ are independent. This can be verified simply by taking the time derivative in Eq. (2.1). Thus, it is sufficient to solve $N-1$ Ginzburg–Landau equations for the order parameters related to the variants, and the other order parameter can be determined by using Eq. (2.1). The modified N independent Ginzburg–Landau equations are listed in Appendix A.

2.5. Boundary conditions

Mechanics problem. On the traction boundary S_{0T}, the traction is specified (denoted by $\boldsymbol{p}^{sp}$), and on the displacement boundary S_{0u}, the displacements are specified (denoted by $\boldsymbol{u}^{sp}$): $\boldsymbol{P}\cdot\boldsymbol{n}_0 = \boldsymbol{p}^{sp}$ on S_{0T}, and $\boldsymbol{u} = \boldsymbol{u}^{sp}$ on S_{0u}. The mixed boundary conditions where, on a single surface, some components of displacements are specified and some components of the traction are specified, are used in some cases.

Phase field problem. For the order parameters, we consider the homogeneous Neumann boundary conditions on S_{0T_k} and specify the order parameter η_k on the respective Dirichlet boundary $S_{0\eta_k}$ [29,45]: $\nabla\eta_k\cdot\boldsymbol{n} = 0$ on S_{0T_k}, and $\eta_k = \eta_k^{sp}$ on $S_{0\eta_k}$ for all $k = 0, 1, 2, \ldots, N$. The homogeneous Neumann boundary conditions in a sample are the consequence of the assumption that the external surface energy does not change during phase transformation [29]. The exact boundary conditions for each problem at hand will be specified in Section 6, where they will be discussed in detail.

3. Weak forms of the governing equations and their linearizations

Assuming the total Lagrangian approach (see e.g. Chapter 8 of [56]), we now derive the weak forms for the equilibrium equation given by Eq. (2.15)$_1$ or (2.15)$_2$ and N independent Ginzburg–Landau equations listed in Appendix A. A non-monolithic strategy has been considered, and the equilibrium equations and all of the phase field equations are solved in a decoupled manner. While solving for the displacements, the order parameters are assumed to remain constant, and while solving for the order parameters during a time step, the total deformation gradient tensor is kept constant. We denote the weighting function (also called the test function or virtual displacements) for the displacements by $\delta\boldsymbol{u}$, which is sufficiently smooth and satisfies $\delta\boldsymbol{u} = \boldsymbol{0}$ on the displacement boundary S_{0u}. The sufficiently smooth test function for each of the order parameters is denoted by $\delta\eta_k$ such that $\delta\eta_k = 0$ on the corresponding order parameter boundary $S_{0\eta_k}$ for all $k = 0, 1, 2, \ldots, N$. Only the main results are discussed in this section. The detailed derivation is shown in Appendix B.

3.1. Equilibrium equations: weak form and linearization

The weak form of the mechanical equilibrium equation Eq. (2.15) is (see for example, [57,58])

$$\mathscr{R}(\boldsymbol{u},\delta\boldsymbol{u}) = -\int_{\Omega_0}(\nabla_0\cdot\boldsymbol{P})\cdot\delta\boldsymbol{u}\,dV_0 = 0, \tag{3.1}$$

which is also known as the principle of virtual work (see e.g. Chapter 3 of [57]). For a given material and the displacement and traction boundary conditions, our objective is to solve for the displacements satisfying the weak form given by Eq. (3.1), which can be rewritten as (see Appendix B for derivation)

$$\mathscr{R}(\boldsymbol{u},\delta\boldsymbol{u}) = \int_{\Omega_0}\boldsymbol{S}:\delta\boldsymbol{E}\,dV_0 - \int_{S_{0T}}\boldsymbol{p}^{sp}\cdot\delta\boldsymbol{u}\,dA_0 = \int_{\Omega_0}\boldsymbol{\tau}:\delta\boldsymbol{\varepsilon}\,dV_0 - \int_{S_{0T}}\boldsymbol{p}^{sp}\cdot\delta\boldsymbol{u}\,dA_0 = 0, \tag{3.2}$$

where $\boldsymbol{S}$ is the second Piola–Kirchhoff stress, $\boldsymbol{\tau} = J\boldsymbol{\sigma}$ is the Kirchhoff stress, $\boldsymbol{p}^{sp}$ is the specified traction on S_{0T}, and $\delta\boldsymbol{E}$ and $\delta\boldsymbol{\varepsilon}$ are the variations of $\boldsymbol{E}$ and $\boldsymbol{\varepsilon}$ given by $\delta\boldsymbol{E} = \boldsymbol{F}^T\cdot\delta\boldsymbol{\varepsilon}\cdot\boldsymbol{F}$ and $\delta\boldsymbol{\varepsilon} := 0.5(\nabla\delta\boldsymbol{u} + \nabla\delta\boldsymbol{u}^T)$; see Chapter 10 of [58].

We will use the Newton's iteration method to find the solution, and thus must linearize Eq. (3.2) in the direction of an increment of the displacement vector denoted by $\Delta\boldsymbol{u}$. Two approaches are generally used in this process [57,59]: (i) in one approach, the weak form, i.e. Eq. (3.2), is discretized and then linearized with respect to the nodal displacements; (ii) in the other approach, at first the weak form is linearized and the resulting equation is then discretized. We will adopt the latter approach here. Note that this latter approach may not work in some cases where nonstandard discretizations are used; see e.g. [59]. Assuming that the external loads are 'dead', i.e. $\boldsymbol{p}^{sp}$ is independent of $\boldsymbol{u}$, we linearize $\mathscr{R}$ (assumed to be a differentiable functional of $\boldsymbol{u}$) in Eq. (3.1) to obtain (see Appendix B for the derivation)

$$\Delta\mathscr{R}\cdot\Delta\boldsymbol{u} = \int_{\Omega_0}J\mathsf{C}:\Delta\boldsymbol{\varepsilon}:\delta\boldsymbol{\varepsilon}\,dV_0 + \int_{\Omega_0}\nabla\Delta\boldsymbol{u}\cdot\boldsymbol{\tau}:\nabla\delta\boldsymbol{u}^T\,dV_0, \quad \text{where} \tag{3.3}$$

$$\mathsf{C} = \mathsf{C}_e + \mathsf{C}_{st} \tag{3.4}$$

is the fourth order total modulus tensor in the deformed configuration composed of the elastic part C_e and the structural part C_{st} which are given by

$$\mathsf{C}_e = \frac{1}{J}(\boldsymbol{F}\boxtimes\boldsymbol{F}):\boldsymbol{\mathcal{C}}_e:(\boldsymbol{F}\boxtimes\boldsymbol{F})^T = \frac{1}{J_e}(\boldsymbol{F}_e\boxtimes\boldsymbol{F}_e):\hat{\boldsymbol{\mathcal{C}}}_e:(\boldsymbol{F}_e\boxtimes\boldsymbol{F}_e)^T, \quad \text{and}$$
$$\mathsf{C}_{st} = \frac{1}{J}[\boldsymbol{\tau}_{st}\otimes\boldsymbol{I}+\boldsymbol{I}\otimes\boldsymbol{\tau}_{st}-2(\boldsymbol{\tau}_{st}\boxtimes\boldsymbol{I}+\boldsymbol{I}\boxtimes\boldsymbol{\tau}_{st}):\mathbb{S}+\rho_0 J(\breve{\psi}^{\theta}+\psi^{\nabla})(2\mathbb{S}-\boldsymbol{I}\otimes\boldsymbol{I})], \tag{3.5}$$

respectively. In Eq. (3.3), $\Delta(\cdot)$ denotes the increment of the function within the argument. Note that in Eq. (3.5)$_1$, $\hat{\boldsymbol{\mathcal{C}}}_e$ is the fourth order elastic modulus tensor with respect to Ω_t:

$$\hat{\boldsymbol{\mathcal{C}}}_e := \frac{\partial\hat{\boldsymbol{S}}_e}{\partial\boldsymbol{E}_e} = \frac{\partial^2\psi_e}{\partial\boldsymbol{E}_e\partial\boldsymbol{E}_e}. \tag{3.6}$$

In Eq. (3.5)$_2$, $\boldsymbol{\tau}_{st}$ denotes the structural part of $\boldsymbol{\tau}$; see Appendix B for the definitions of the products between the second order tensors denoted by $\otimes$ and $\boxtimes$, fourth order symmetrizer $\mathbb{S}$, and transpose of a fourth order tensor. The fourth order elasticity and structural tensors can be expressed in the indicial notations as

$$\mathsf{C}_{(e)abcd} = \frac{1}{J}F_{aA}F_{bB}F_{cC}F_{dD}\mathcal{C}_{(e)ABCD} = \frac{1}{J_e}F_{(e)a\hat{A}}F_{(e)b\hat{B}}F_{(e)c\hat{C}}F_{(e)d\hat{D}}\hat{\mathcal{C}}_{(e)\hat{A}\hat{B}\hat{C}\hat{D}}, \quad \text{and}$$
$$\begin{aligned} J\mathsf{C}_{(st)abcd} = {} & \tau_{(st)ab}\delta_{cd}+\delta_{ab}\tau_{(st)cd}-(\tau_{(st)ac}\delta_{bd}+\tau_{(st)ad}\delta_{bc}+\delta_{ac}\tau_{(st)bd}+\delta_{ad}\tau_{(st)bc})+ \\ & \rho_0 J(\breve{\psi}^{\theta}+\psi^{\nabla})(\delta_{ac}\delta_{bd}+\delta_{ad}\delta_{bc}-\delta_{ab}\delta_{cd}), \end{aligned} \tag{3.7}$$

respectively, where, following Zienkiewicz and Taylor [58], we use the indices in capital letters (i.e. A, B, C, D etc.) for Ω_0, and the indices in lower case (i.e. a, b, c, d etc.) for Ω. The indices with 'hat' (i.e. $\hat{A}$, $\hat{B}$, $\hat{C}$, $\hat{D}$ etc.) are used for Ω_t.

Notably, all of the elasticity tensors $\boldsymbol{\mathcal{C}}_e$, $\hat{\boldsymbol{\mathcal{C}}}_e$, and C_e and the structural tensor C_{st} possess both minor and major symmetries: e.g. $\mathcal{C}_{(e)ABCD}=\mathcal{C}_{(e)BACD}=\mathcal{C}_{(e)ABDC}$ (minor symmetry), and $\mathcal{C}_{(e)ABCD}=\mathcal{C}_{(e)CDAB}$ (major symmetry); see e.g. Chapter 6 of [56] for the definitions. Consequently, C also possess those symmetries. For solids, $\hat{\boldsymbol{\mathcal{C}}}_e$ is known either from experiments or from atomistic calculations, and hence it is considered as a material property (see Eq. (2.9)). Obviously, for any material point, $\boldsymbol{\mathcal{C}}_e$ and C_e depend not only on $\hat{\boldsymbol{\mathcal{C}}}_e$, but also on the present state of deformation. The relation between C_e and $\boldsymbol{\mathcal{C}}_e$ in Eq. (3.5)$_1$ is well-known in nonlinear elasticity (see e.g. Chapter 6 of [56]), but to the best of our knowledge, the relations between these tensors and $\hat{\boldsymbol{\mathcal{C}}}_e$ in Eq. (3.5)$_1$ appear here for the first time. Obviously, if the interfacial stresses are neglected, i.e. the barrier and gradient energies in the Helmholtz free energy given by Eq. (2.7) are not multiplied by J and the gradient of the order parameters are taken in Ω_0, $\boldsymbol{\sigma}_{st}$ identically vanishes and so does C_{st}.

The last integral in Eq. (3.3) contributes to the total tangent stiffness matrix, which is also called the geometric stiffness (see Section 4, as well as e.g. [57,58]). Note that the contribution of this integral has arisen due to the geometric nonlinearity, and it is thus neglected in the small strain FE formulations [60].

Note that the integrands of the weak form $\mathscr{R}$ (given by Eq. (3.2)$_2$) and its linearization $\Delta\mathscr{R}\cdot\Delta\boldsymbol{u}$ (given by Eq. (3.3)) are all expressed in terms of the stresses, strains, and tangent modulus in the deformed configuration Ω, whereas the integrations are performed in the reference body Ω_0. This approach has an advantage over the one in which the integrands are expressed in Ω in that the computation of the standard $\boldsymbol{B}^{fe}$ matrix (in FEM) is much simpler. In fact, the $\boldsymbol{B}^{fe}$ matrix in this case turns out to be identical to the matrix used in the small strain calculations (see [57] and Chapter 10 of [58] for details).

3.2. Ginzburg–Landau equations: time discretization, weak form, and linearization

We now derive the weak forms of N independent Ginzburg–Landau equations listed in Eq. (A.1), which were obtained using the original $N+1$ equations given by Eq. (2.20). We discretize the time derivative of the order parameters using a backward difference scheme over a time period $t\in[t^0,t^f]$ and then write the weak forms, where t^0 and t^f denote the initial and final time instances, respectively.

An A-stable backward difference scheme of order two (BDF2) is used to discretize the time derivatives (see [61] for details of the scheme). Such a scheme requires solutions from the two consecutive previous time steps. Thus, for the first time step, we use BDF1 scheme (first order backward difference scheme), which requires the solution from

the previous time step only (which will be provided by the initial conditions). Then, from the second step onwards, the BDF2 scheme is used. For the BDF1 or BDF2 scheme, $\dot{\eta}_k$ is discretized as [61]

$$\dot{\eta}_k = \frac{c_1\eta_k^n + c_2\eta_k^{n-1} + c_3\eta_k^{n-2}}{\Delta t^n} \quad \text{for } k = 0, 1, \ldots, N, \tag{3.8}$$

where for BDF1, $c_1 = 1$, $c_2 = -1$, and $c_3 = 0$, and for BDF2, $c_1 = 1.5$, $c_2 = -2$, and $c_3 = 0.5$. In Eq. (3.8), the superscript $n = 0, 1, 2, \ldots$ denotes the index for time such that the time instance after n^{th} time iteration is $t^{n+1} = t^n + \Delta t^n$, and Δt^n denotes the accepted time step size leading to the converged solutions for the order parameters in our adaptive time stepping scheme. Discretizing the N independent equations from Eq. (A.1) by using Eq. (3.8), the finite difference forms of the kinetic equations are obtained and are then multiplied by the weighted function $\delta\eta_k^n$, integrated over the entire domain to obtain the weak forms corresponding to N independent Ginzburg–Landau equations, which can be expressed in the following general form (see Appendix B.2 for derivation)

$$\begin{aligned}\mathcal{R}_k = c_1\int_{\Omega_0}\eta_k^n\delta\eta_k^n dV_0 + \Delta t^n\int_{\Omega_0}L_k^\beta J^n\chi_k^n\,(\boldsymbol{F}^{n-1}\cdot\boldsymbol{F}^{n-T}\cdot\nabla_0\eta_k^n)\cdot\nabla_0\delta\eta_k^n dV_0 + \Delta t^n\int_{\Omega_0}f_k^n\,\delta\eta_k^n dV_0 + \\ c_2\int_{\Omega_0}\eta_k^{n-1}\delta\eta_k^n dV_0 + c_3\int_{\Omega_0}\eta_k^{n-2}\delta\eta_k^n dV_0 = 0 \quad \text{for } k = 0, 1, \ldots, N-1.\end{aligned} \tag{3.9}$$

To obtain Eq. (3.9), we have used the Gauss divergence theorem and the Nanson's formula $\boldsymbol{n}\,dS = J\boldsymbol{F}^{-T}\cdot\boldsymbol{n}_0\,dS_0$ [56], applied the homogeneous Neumann boundary condition on the entire boundary (see Section 2.5), and assumed that all of the kinetic coefficients are spatially constants. In Eq. (3.9), $L_0^\beta = L_{0M}\beta_{0M}$, $\chi_0^n = 1$, $L_k^\beta = \sum_{m=1,\neq k}^{N} L_{km}\bar{\beta}_{km}/4$, and $\chi_k^n = \tilde{\varphi}(a_\beta, a_c, \eta_0)$ for all $k = 1, 2, \ldots, N-1$. The expressions for f_0^n and f_i^n (for all $i = 1, \ldots, N-1$) are listed in Appendix B.2 and given by Eqs. (B.28) and (B.40), respectively.

We use the Taylor expansion of the weak forms about η_k^n, i.e.

$$\mathcal{R}_k(\eta_k^n + \Delta_k\eta_k^n, \delta\eta_k^n) = \mathcal{R}_k(\eta_k^n, \delta\eta_k^n) + \Delta_k\mathcal{R}_k + o(\Delta_k\eta_k^n) = 0 \quad \text{for } k = 0, 1, \ldots, N-1, \tag{3.10}$$

to obtain the tangent matrix, where the increment of a function (or functional) with respect to η_k is denoted by Δ_k, and

$$\begin{aligned}\Delta_k\mathcal{R}_k = \left.\frac{\partial\mathcal{R}_k}{\partial\eta_k^n}\right|_{\boldsymbol{F}}\Delta_k\eta_k^n = c_1\int_{\Omega_0}\Delta_k\eta_k^n\delta\eta_k^n dV_0 \\ + \Delta t^n\int_{\Omega_0}L_k^\beta\chi_k^n J^n(\boldsymbol{F}^{n-1}\cdot\boldsymbol{F}^{n-T}\cdot\nabla_0\Delta_k\eta_k^n)\cdot\nabla_0\delta\eta_k^n dV_0 + \\ \Delta t^n\int_{\Omega_0}\left.\frac{\partial f_k^n}{\partial\eta_k^n}\right|_{\boldsymbol{F}}\Delta_k\eta_k^n\delta\eta_k^n dV_0 \qquad \text{for } k = 0, 1, \ldots, N-1.\end{aligned} \tag{3.11}$$

The complete expressions for $\left(\partial f_0^n/\partial\eta_0^n\right)_{\boldsymbol{F}}$ and $\left(\partial f_k^n/\partial\eta_k^n\right)_{\boldsymbol{F}}$ are given by Eqs. (B.41) and (B.42), respectively. Note that the derivatives of the weak forms have been calculated while keeping $\boldsymbol{F}$ fixed within our non-monolithic formulation, as we assume that the state of deformation within the body remains fixed while the order parameters are evolving.

4. Finite element implementation

We discretize the reference configuration Ω_0 (i.e. the initial body) into n_{el} number of isoparametric elements, i.e. $\Omega_0 \approx \cup_{el=1}^{n_{el}}\Omega_0^{el}$, and consider the following interpolations in element Ω_0^{el} (also see [57]):

$$\begin{aligned}&\boldsymbol{r}_0^{el} = \sum_{\iota=1}^{n_g}N_\iota(\boldsymbol{\xi})\tilde{\boldsymbol{r}}_{0\iota}, \quad \boldsymbol{r}^{el} = \sum_{\iota=1}^{n_g}N_\iota(\boldsymbol{\xi})\tilde{\boldsymbol{r}}_\iota, \quad \boldsymbol{u}^{el} = \sum_{\iota=1}^{n_g}N_\iota(\boldsymbol{u})\tilde{\boldsymbol{u}}_\iota, \quad \delta\boldsymbol{u}^{el} = \sum_{\iota=1}^{n_g}N_\iota(\boldsymbol{\xi})\delta\tilde{\boldsymbol{u}}_\iota,\\ &\Delta\boldsymbol{u}^{el} = \sum_{\iota=1}^{n_g}N_\iota(\boldsymbol{\xi})\Delta\tilde{\boldsymbol{u}}_\iota, \quad \eta_k^{el} = \sum_{\iota=1}^{n_g}N_\iota(\boldsymbol{\xi})\tilde{\eta}_{k\iota}, \quad \delta\eta_k^{el} = \sum_{\iota=1}^{n_g}N_\iota(\boldsymbol{\xi})\delta\tilde{\eta}_{k\iota}, \quad \Delta_k\eta_k^{el} = \sum_{\iota=1}^{n_g}N_\iota(\boldsymbol{\xi})\Delta_k\tilde{\eta}_{k\iota},\\ &\text{for all } k = 0, 1, \ldots, N-1,\end{aligned} \tag{4.1}$$

where N_ι ($\iota = 1, 2, \ldots, n_g$) are the shape functions corresponding to the element Ω_0^{el}; n_g is the number of grid points in each element; the quantities with tilde correspond to the nodal values, i.e., for example, $\tilde{\boldsymbol{u}}_\iota$ denotes the displacement vector at ι^{th} node; $\boldsymbol{\xi}$ denotes the coordinates of the isoparametric reference element (see e.g. Chapter 4 of [57]); and

the superscript el denotes the index for the finite elements. The deformation gradient tensor in Ω_0^{el} can hence be expressed as (see e.g. Chapter 4 of [57])

$$\boldsymbol{F}^{el} = \boldsymbol{j}^{el} \cdot \boldsymbol{J}^{el\,-1}, \quad \text{where } \boldsymbol{J}^{el} = \frac{\partial \boldsymbol{r}_0{}^{el}}{\partial \boldsymbol{\xi}} = \sum_{\iota=1}^{n_g} \tilde{\boldsymbol{r}_{0\iota}} \otimes \nabla_\xi N_\iota, \quad \boldsymbol{j}^{el} = \frac{\partial \boldsymbol{r}^{el}}{\partial \boldsymbol{\xi}} = \sum_{\iota=1}^{n_g} \tilde{\boldsymbol{r}_\iota} \otimes \nabla_\xi N_\iota, \tag{4.2}$$

and ∇_ξ denotes the gradient operator in the coordinate of the isoparametric element. Denoting the local coordinate system of the reference element in our isoparametric mapping by $\boldsymbol{\xi} = \{\xi_1, \xi_2, \xi_3\}^T$, we can write $\nabla_\xi N_\iota = [N_{\iota,\xi_1}, N_{\iota,\xi_2}, N_{\iota,\xi_3}]^T$, where the subscripts followed by a comma designate the derivative with respect to the corresponding isoparametric coordinate. The spatial gradients of the displacement and the order parameters, as well as the gradients of their weighting functions and increments take the form (see e.g. Chapter 4 of [57]):

$$\begin{aligned}
&\nabla \boldsymbol{u}^{el} = \sum_{\iota=1}^{n_g} \tilde{\boldsymbol{u}}_\iota \otimes \boldsymbol{j}^{el\,-T} \cdot \nabla_\xi N_\iota, \quad \nabla \delta \boldsymbol{u}^{el} = \sum_{\iota=1}^{n_g} \delta\tilde{\boldsymbol{u}}_\iota \otimes \boldsymbol{j}^{el\,-T} \cdot \nabla_\xi N_\iota, \quad \nabla \Delta \boldsymbol{u}^{el} = \sum_{\iota=1}^{n_g} \Delta\tilde{\boldsymbol{u}}_\iota \otimes \boldsymbol{j}^{el\,-T} \cdot \nabla_\xi N_\iota; \\
&\nabla \eta_k^{el} = \sum_{\iota=1}^{n_g} \tilde{\eta}_{k\,\iota} \boldsymbol{j}^{el\,-T} \cdot \nabla_\xi N_\iota, \quad \nabla \delta \eta_k^{el} = \sum_{\iota=1}^{n_g} \delta\tilde{\eta}_{k\,\iota} \boldsymbol{j}^{el\,-T} \cdot \nabla_\xi N_\iota, \quad \nabla \Delta_k \eta_k^{el} = \sum_{\iota=1}^{n_g} \Delta_k\tilde{\eta}_{k\,\iota} \boldsymbol{j}^{el\,-T} \cdot \nabla_\xi N_\iota.
\end{aligned} \tag{4.3}$$

4.1. Discretization of the equilibrium equation

We now use Eq. (3.2) in Eq. (B.3), discretize the resulting equations using Eqs. (4.1)–(4.3) while neglecting the higher order terms in $\Delta \boldsymbol{u}$ from Eq. (B.3), apply the standard assembly operation, and then use the arbitrariness of the global weighting vector (nodal) to finally obtain the system of algebraic equations given by Eq. (4.4) in Box-I (also see [57,59]). Note that $\Delta \boldsymbol{u}^p$ is the $n_u \times 1$ incremental displacement matrix at the p^{th} iteration; $\boldsymbol{K}$ and $\boldsymbol{r}_u$ are the $n_u \times n_u$ symmetric global tangent matrix and $n_u \times 1$ residual vector defined by Eqs. $(4.5)_1$ and Eq. $(4.5)_2$, respectively, (also see [57,58]), where $G_{\iota\kappa}\boldsymbol{I} = (\nabla N_\iota \cdot \boldsymbol{\tau}^{el} \cdot \nabla N_\kappa)\boldsymbol{I}$ is the geometric stiffness part of the total tangent matrix, and n_u is the total number of displacement degrees of freedom. In Eqs. $(4.5)_{1,2}$, ∇N_ι and $\boldsymbol{B}_\iota^{fe}$ are the standard matrices given by Eqs. $(4.5)_5$ and $(4.5)_6$, respectively, where the subscripts followed by a comma designate the derivative with respect to the corresponding spatial coordinate in the deformed configuration. In Eq. (4.4) , the dot implies the multiplication between the square matrix $\boldsymbol{K}$ and the column matrix $\Delta \boldsymbol{u}^p$. The geometric stiffness term does not appear in a small strain formulation; see e.g. [60]. C_e^{el} and C_{st}^{el} are the 6×6 elemental stiffness matrices whose elements are obtained using Eqs. $(3.7)_1$ and $(3.7)_2$, respectively, and $\{\boldsymbol{\tau}^{el}\} = \{\tau_{11}, \tau_{22}, \tau_{33}, \tau_{12}, \tau_{23}, \tau_{13}\}^T$ is a 6×1 elemental stress matrix whose elements are obtained using the standard $\boldsymbol{\tau}$ tensor; see e.g. Chapter 4 of [57]. The displacements after the p^{th} iteration are determined by using Eq. (4.6) (see Section 4.3 for a complete iterative procedure). We will solve Eq. (4.4) iteratively to update the displacements at every time step while keeping the order parameters constant. A step-by-step procedure to solve the mechanics problem is outlined in Section 4.3. The symbol $\cup$ designates the standard assembly operation in FE.

4.2. Discretization of the phase field equations

Similarly, we use Eq. (3.9) in Eq. (3.10), discretize the resulting equation by using Eqs. $(4.1)_{6,7,8}$, and perform the standard assembly operation to obtain the linear system of equations given by Eq. (4.7) in Box-I corresponding to each of the N independent phase field equations (see Eq. (A.1)). Note that $\boldsymbol{\eta}_i^{n,q}$ is the $n_i \times 1$ global matrix for the order parameter η_i^n after the q^{th} Newton's iteration, the global matrix $\Delta\boldsymbol{\eta}_i^{n,q}$ of size $n_i \times 1$ corresponds to the increment $\Delta\eta_i^{n,q}$ of the order parameters, $\boldsymbol{Q}_i$ is a $n_i \times n_i$ symmetric global matrix given by Eq. $(4.8)_1$, and n_i is the total number of degrees of freedom for the order parameter η_i. All of the order parameters are then updated using Eq. (4.9) . In Eq. (4.8) , $\boldsymbol{M}_i$, $\boldsymbol{H}_i$, and $\boldsymbol{G}_i$ are $n_i \times n_i$ symmetric global matrices, and $\boldsymbol{f}_i$ and $\boldsymbol{r}_i$ are $n_i \times 1$ global column matrices. The matrix $\boldsymbol{H}_i$ is also known as the Laplace matrix. We will solve Eq. (4.7) iteratively and update the order parameters at every time step using Eq. (4.9) while keeping the state of deformation of the body fixed. A step-by-step procedure to solve the phase field problem is given in Section 4.3. The order parameter η_N at each node is determined using Eq. (2.1).

Box-I. List of finite element equations

- System of algebraic equations for obtaining the nodal displacements

$$\boldsymbol{K}\cdot\Delta\boldsymbol{u}^{p}=-\boldsymbol{r}_{u},\quad \text{where} \tag{4.4}$$

$$\begin{aligned}
\boldsymbol{K}(\boldsymbol{u}^{p-1}) &= \bigcup_{el=1}^{n_{el}}\sum_{\iota=1}^{n}\sum_{\kappa=1}^{n}\int_{\Omega^{el}}(G_{\iota\kappa}\boldsymbol{I}+\boldsymbol{B}_{\iota}^{fe^{T}}\cdot\boldsymbol{C}^{el}\cdot\boldsymbol{B}_{\kappa}^{fe})\,dV_0;\\
\boldsymbol{r}_{u}(\boldsymbol{u}^{p-1}) &= \bigcup_{el=1}^{n_{el}}\sum_{\iota=1}^{n}\int_{\Omega^{el}}\boldsymbol{B}_{\iota}^{fe^{T}}\cdot\{\boldsymbol{\tau}^{el}\}\,dV_0;\\
\boldsymbol{C}^{el} &= \boldsymbol{C}_{e}^{el}+\boldsymbol{C}_{st}^{el};\\
G_{\iota\kappa}\boldsymbol{I} &= (\nabla N_{\iota}\cdot\boldsymbol{\tau}^{el}\cdot\nabla N_{\kappa})\,\boldsymbol{I};
\end{aligned}$$

$$\nabla N_{\iota}=\begin{bmatrix}N_{\iota,1}\\N_{\iota,2}\\N_{\iota,3}\end{bmatrix};\quad\text{and}\quad \boldsymbol{B}_{\iota}^{fe}=\begin{bmatrix}N_{\iota,1}&0&0\\0&N_{\iota,2}&0\\0&0&N_{\iota,3}\\N_{\iota,2}&N_{\iota,1}&0\\0&N_{\iota,3}&N_{\iota,2}\\N_{\iota,3}&0&N_{\iota,1}\end{bmatrix}. \tag{4.5}$$

The displacements after the pth iteration are updated using

$$\boldsymbol{u}^{p}=\boldsymbol{u}^{p-1}+\Delta\boldsymbol{u}^{p}. \tag{4.6}$$

- System of algebraic equations for obtaining the nodal order parameters

$$\boldsymbol{Q}_{i}\cdot\Delta_{i}\boldsymbol{\eta}_{i}^{n,q}=-\boldsymbol{r}_{i}\quad\text{for } i=0,1,\ldots,N-1,\quad\text{where} \tag{4.7}$$

$$\begin{aligned}
\boldsymbol{Q}_{i}(\eta_{k}^{n,p-1}) &= c_1\boldsymbol{M}_{i}+\Delta t^{n}\boldsymbol{H}_{i}+\Delta t^{n}\boldsymbol{G}_{i};\\
\boldsymbol{M}_{i} &= \bigcup_{el=1}^{n_{el}}\sum_{\iota=1}^{n_g}\sum_{\kappa=1}^{n_g}\int_{\Omega_0^{el}}N_{\iota}N_{\kappa}\,dV_0;\\
\boldsymbol{H}_{i}(\eta_{k}^{n,p-1}) &= \bigcup_{el=1}^{n_{el}}\sum_{\iota=1}^{n_g}\sum_{\kappa=1}^{n_g}\int_{\Omega_0^{el}}\chi_{i}^{n,p-1}L_{i}^{\beta}J^{n}\nabla N_{\iota}\cdot\nabla N_{\kappa}\,dV_0;\\
\boldsymbol{G}_{i}(\eta_{k}^{n,p-1}) &= \bigcup_{el=1}^{n_{el}}\sum_{\iota=1}^{n_g}\sum_{\kappa=1}^{n_g}\int_{\Omega_0^{el}}\left.\frac{\partial f_{i}^{n}(\eta_{i}^{n,p-1})}{\partial\eta_{i}^{n}}\right|_{\boldsymbol{F}}N_{\iota}N_{\kappa}\,dV_0;\\
\boldsymbol{r}_{i}(\eta_{k}^{n,p-1}) &= (c_1\boldsymbol{M}_{i}+\Delta t^{n}\boldsymbol{H}_{i})\cdot\boldsymbol{\eta}_{i}^{n,p-1}+c_2\boldsymbol{M}_{i}\cdot\boldsymbol{\eta}_{i}^{n-1}+c_3\boldsymbol{M}_{i}\cdot\boldsymbol{\eta}_{i}^{n-2}+\Delta t^{n}\boldsymbol{f}_{i};
\end{aligned}$$

$$\boldsymbol{f}_{i}(\eta_{k}^{n,p-1})=\bigcup_{el=1}^{n_{el}}\sum_{\iota=1}^{n_g}\int_{\Omega_0^{el}}f_{i}^{n}(\eta_{k}^{n,p-1})N_{\iota}\,dV_0; \tag{4.8}$$

for all $k=0,1,\ldots,N-1$. The order parameters are updated using

$$\boldsymbol{\eta}_{i}^{n,q}=\boldsymbol{\eta}_{i}^{n,q-1}+\Delta\boldsymbol{\eta}_{i}^{n,q}. \tag{4.9}$$

4.3. Computational algorithm

We now present the overall computational algorithm for solving the coupled mechanics and phase field equations (the line followed by # indicates comments). We define the symbols used in the algorithm below: t^n—time instance after the $(n-1)^{th}$ iteration (note that $t^0 = 0$); t^f—final time; ϵ_u- tolerance for the convergence of equilibrium equation; ϵ_η—tolerance for the convergence of all of the Ginzburg–Landau equations; Nsteps_η^{max}—maximum number of iterations for the phase field equations; ϵ_{time}—tolerance for the adaptive time stepping; Δt^{max}—maximum time step allowed; Δt^{min}—minimum time step allowed.

---

1. Input: initialize $n = 0$ with $\boldsymbol{F}^0 = \boldsymbol{I}$ in the given reference configuration, and initial distributions of η_i for $i = 0, 1, \ldots, N$; material properties and other parameters listed in the beginning of this Section 4.3.
2. WHILE $(t^n \leq t^f)$ {
   (a) #(Newton's iteration for displacements; p being the index for iteration)
   Take $p = 0$ and $\boldsymbol{u}^{n,0} = \boldsymbol{u}^n$
   DO{
   - Set $p \to p + 1$
   - Update $\boldsymbol{F}(\boldsymbol{u}^{n,p-1}) = \boldsymbol{I} + \nabla_0 \boldsymbol{u}^{n,p-1}$ (see Eq. $(2.2)_1$) and $\overline{\boldsymbol{F}}_t(\eta_j^n)$ (where $j = 0, 1, \ldots, N-1$) using Eq. (2.4) or (2.6) based on KM at hand
   - Compute $\boldsymbol{F}_e$ using Eq. $(2.2)_2$ and $\boldsymbol{\sigma}$ using $\boldsymbol{\sigma} = \boldsymbol{\sigma}_e + \boldsymbol{\sigma}_{st}$, $(2.16)_2$, and (2.18)
   - Compute $\boldsymbol{K}(\boldsymbol{u}^{n,p-1})$ and $\boldsymbol{r}_u(\boldsymbol{u}^{n,p-1})$ using Eqs. $(4.5)_1$ and $(4.5)_2$
   - Solve the linear system of Eq (4.4), i.e. $\boldsymbol{K}(\boldsymbol{u}^{n,p-1}) \cdot \Delta \boldsymbol{u}^{n,p} = -\boldsymbol{r}_u(\boldsymbol{u}^{n,p-1})$ to obtain $\Delta \boldsymbol{u}^{n,p}$
   - Update displacement field using Eq. (4.6), i.e. $\boldsymbol{u}^{n,p} = \boldsymbol{u}^{n,p-1} + \Delta \boldsymbol{u}^{n,p}$
   - Calculate the Euclidean norms $|\boldsymbol{r}_u(\boldsymbol{u}^{n,p})|$ and $|\boldsymbol{r}_u(\boldsymbol{u}^{n,1})|$

   }WHILE $(|\boldsymbol{r}_u(\boldsymbol{u}^{n,p})| \leq \epsilon_u \times |\boldsymbol{r}_u(\boldsymbol{u}^{n,1})|)$
   Set $n \to n + 1$
   (b) #(Newton's iteration for η_i for all $i = 0, 1, \ldots, N-1$; q being the index for iteration)
   Take $q = 0$, and $\boldsymbol{\eta}_i^{n,0} = \boldsymbol{\eta}_i^{n-1}$
   Compute $\boldsymbol{F}^n$ using Eq. $(2.2)_1$, i.e. $\boldsymbol{F}^n = \boldsymbol{I} + \nabla_0 \boldsymbol{u}^{n-1}$
   DO {
   i. Set $q \to q + 1$
   ii. IF $(q = \text{Nsteps}_\eta^{max})$ {
   Reject solutions of step vi;
   EXIT this DO loop (i.e. step (b)) and GOTO step (c) }
   iii. Compute $\overline{\boldsymbol{F}_t}(\eta_i^{n,q-1})$ using Eq. (2.4) or (2.6), $\boldsymbol{F}_e$ using Eq. $(2.2)_2$, and $\boldsymbol{\sigma}$ using $\boldsymbol{\sigma} = \boldsymbol{\sigma}_e + \boldsymbol{\sigma}_{st}$, $(2.16)_2$ and (2.18)
   iv. Compute the vectors and matrices $\boldsymbol{Q}_i^n(\eta_k^{n,q-1})$, $\boldsymbol{M}_i(\eta_k^{n,q-1})$, $\boldsymbol{H}_i(\eta_k^{n,q-1})$, $\boldsymbol{G}_i(\eta_k^{n,q-1})$, $\boldsymbol{r}_i(\eta_k^{n,q-1})$, and $\boldsymbol{f}_i(\eta_k^{n,q-1})$ for $k = 0, 1, \ldots, N-1$
   v. Solve Eq. (4.7) to obtain $\Delta_i \boldsymbol{\eta}_i^{n,q}$
   vi. Update $\boldsymbol{\eta}_i^{n,q} = \boldsymbol{\eta}_i^{n,q-1} + \Delta_i \boldsymbol{\eta}_i^{n,q}$
   vii. Calculate the Euclidean norms $|\boldsymbol{r}_i(\eta_k^{n,q})|$ for all $k = 0, 1, \ldots, N-1$

   }WHILE $(|\boldsymbol{r}_0(\eta_k^{n,q})| \leq \epsilon_\eta \times |\boldsymbol{r}_0(\eta_k^{n,1})|$ && $\ldots$ && $|\boldsymbol{r}_{N-1}(\eta_k^{n,q})| \leq \epsilon_\eta \times |\boldsymbol{r}_{N-1}(\eta_k^{n,1})|)$
   (c) # time step selection
   IF $(q = \text{Nstep}_\eta^{max})$ {
   Reject solutions $\boldsymbol{\eta}_i^n$ for all $i = 0, 1, \ldots, N-1$ of step (b)
   Reduce time step to $\Delta t^n = 0.5 \Delta t^n$ and repeat step (b)
   }
   ELSE {

- Compute the quantity $X^{max} = max(L_{0M}\overline{X}_{0M}, \sum_{m=1}^{N} L_{km}\overline{X}_{km})$ for all $k = 1, \ldots, N-1$ among all grid points; see Eqs. (A.2) and (B.29)
- Compute the next time step as $\Delta t^n = \dfrac{\epsilon_{\text{time}}}{X^{max}}$
- IF $(\Delta t^n > \Delta t^{max})\{$
  $\Delta t^n = \Delta t^{max}$ $\}$
  IF $(\Delta t^n < \Delta t^{min})$ $\{$
  $\Delta t^n = \Delta t^{min}$ $\}$
  $\}$

(d) Set $t^n = t^{n-1} + \Delta t^n$ and continue the loop in step (2)

$\}$

5. Material parameters identification

When we assume that the material is stress-free, the interfaces are planar, the order parameters spatially vary only with r_{01}, and the material parameters A_{0M}, β_{0M}, $\tilde{A}$ and β_{12} are constants, the Ginzburg–Landau equations in (A.1) for A-M (with $\eta_1 = 1$) and M_1-M_2 (with $\eta_0 = 1$) are simplified and yield the following solutions [45]:

$$\eta_0 = [1 + \exp(-\zeta_{0M})]^{-1}, \quad \text{where } \zeta_{0M} = \frac{6}{\delta_{0M}}(r_{01} - r_c - c_{0M}t), \quad \text{and}$$
$$\eta_1 = [1 + \exp(-\zeta_{12})]^{-1}, \quad \text{where } \zeta_{12} = \frac{6}{\delta_{12}}(r_{01} - r_c - c_{12}t), \tag{5.1}$$

respectively. In the respective cases of Eq. $(5.1)_{1,2}$, δ designates the width of the interface which is defined as the distance between the points with $\eta = 0.05$ and $\eta = 0.95$ [4], c denotes the interface propagation speed, and γ denotes the interfacial energy:

$$\delta_{0M} = \sqrt{\frac{18\beta_{0M}}{\rho_0[(a_\theta - 3)\Delta\psi^\theta(\theta) + A_{0M}(\theta)]}}, \qquad c_{0M} = L_{0M}\delta_{0M}\Delta\psi^\theta(\theta), \qquad \gamma_{0M} = \frac{\beta_{0M}}{\delta_{0M}},$$
$$\delta_{12} = \sqrt{\frac{18\beta_{12}}{\rho_0\tilde{A}}}, \qquad c_{12} = 0, \qquad \gamma_{12} = \frac{\beta_{12}}{\delta_{12}}, \tag{5.2}$$

where r_c is the coordinate of the point where $\eta_0 = 0.5$ and $\eta_1 = 0.5$ for the respective interfaces. The subscripts '$0M$' and '12'are used to indicate the A-M and M_1-M_2 interfaces, respectively.

We assume the isotropic St. Venant–Kirchhoff elastic response of the solid, and hence [56] $\hat{\mathcal{C}}_{(e)\hat{A}\hat{B}\hat{C}\hat{D}} = \lambda\,\delta_{\hat{A}\hat{B}}\delta_{\hat{C}\hat{D}} + \mu\,(\delta_{\hat{A}\hat{C}}\delta_{\hat{B}\hat{D}} + \delta_{\hat{A}\hat{D}}\delta_{\hat{B}\hat{C}})$, where λ and μ are the Lamé constants. Notably, the St. Venant–Kirchhoff energy is non-quasiconvex [62,63] (not even being rank-one convex), and spurious microstructures might appear as a consequence. However, the elastic strains are small in the problems considered here; hence, the quadratic energy given by Eq. $(2.9)_1$ is a convex function of $\boldsymbol{E}_e$ in the neighborhood of $\boldsymbol{E}_e = \boldsymbol{0}$. The microstructures in our problems have appeared due to the material instability related to the order parameters, and not due to the elastic instability. We would like to mention that, to avoid this problem for large elastic strains, several other isotropic elastic energies have been used to study microstructure evolutions in [64,65].

The material properties for NiAl alloy based on the atomistic simulations are taken (see [66,67] and the references therein). The alloy has a cubic lattice in A phase and a tetragonal lattice for all M_i phases. The energies and widths of the A-M and M_1-M_2 interfaces are taken to be $\gamma_{0M} = 0.2$ N/m, $\gamma_{12} = 0.1$ N/m, $\delta_{0M} = 2$ nm, and $\delta_{12} = 0.75$ nm, respectively (see e.g. [26] for their typical values). The following material parameters for NiAl are used [45,66,67]: $\lambda = 74.62$ GPa, $\mu = 72$ GPa, $L_{0M} = L_{12} = 2600$ (Pa-s)$^{-1}$, $\Delta s_{0M} = -1.47$ MPa/K, $\theta_e = 215$ K, $a_\theta = a_b = a_\beta = a_K = 3$, $a_c = 0.001$. The barrier heights and the interface energy coefficients are determined by using Eq. (5.2) for given widths and energies of the interfaces: $A_{0M} = 3.6$ GPa, $\beta_{0M} = 2 \times 10^{-10}$ N, $\tilde{A} = 2.4$ GPa, $\beta_{12} = 7.5 \times 10^{-11}$ N. In all of the examples we have taken $K_{012} = 0$, i.e. the energies of the triple junctions are not penalized here. The appropriate values of this coefficient should be calibrated by using the energy balance relation at the junction within the sharp interface model (e.g. see [68]), which is not perused in this paper. However, the consequence of penalizing the junctions can be seen in [45].

6. Numerical examples

We will now show the simulation results obtained through the formulation and algorithm presented above. The nonlinear FE codes have been developed and executed in an open source deal.II [69]. Three different problems have been solved:

(i) simple shear deformation of a 3D parallelepiped with evolution of austenite and single M variant (Section 6.1);

(ii) twinning in martensite, and the effect of sample size on the twinned microstructure in 2D samples using the generalized plane strain approach (Section 6.2);

(iii) microstructure evolution in a 2D block under nanoindentation using the plane stress condition (Section 6.3).

The list of simplified equations for a system with austenite and two variants M_1 and M_2 is presented in the supplementary material [70]. The performance of the adaptive time stepping is also analyzed. The following parameter values $\epsilon_u = 5 \times 10^{-6}$, $\epsilon_\eta = 10^{-3}$, $\text{Nsteps}_\eta^{max} = 10$ are used in all problems (see Section 4.3 for their definitions). However, the other parameters ϵ_{time}, Δt^{max}, and Δt^{min} are chosen differently in each problem and are reported while discussing the respective problems.

6.1. Simple shear in a rectangular parallelepiped with A and single variant M_1

We consider a rectangular parallelepiped as shown schematically in Fig. 3(a) for studying the simple shear problem. Our aim is to study the case which yields a homogeneous stress-free analytical stationary solution, and we will also determine if our heterogeneous non-stationary solution, which involves significant internal stresses and finite strains, converges to such a stress-free homogeneous solution.

6.1.1. Analytical solutions for simple shear in a rectangular parallelepiped

We assume a simple shear-based stress-free analytical homogeneous stationary solution with an invariant A-M interface:

$$\boldsymbol{F} = \boldsymbol{Q} \cdot \boldsymbol{U}_{t1} = \boldsymbol{I} + \gamma_t \boldsymbol{e}_2 \otimes \boldsymbol{e}_1 \tag{6.1}$$

(see Eq. (6.5) for a general form), where $\boldsymbol{U}_{t1}$ is the transformation stretch (or Bain stretch) tensor, $\boldsymbol{Q}$ is the rigid-body rotation, γ_t is the transformation shear strain, $\boldsymbol{e}_1$ is the unit normal to the invariant plane interface (fixed left end ABCD of the sample shown in Fig. 3(a)), and $\boldsymbol{e}_2$ is the direction of shear (see Fig. 3(a)). The transformation stretch tensor and the rotation tensor are calculated using $\boldsymbol{U}_{t1} = \sqrt{\boldsymbol{F}^T \cdot \boldsymbol{F}}$ and $\boldsymbol{Q} = (\boldsymbol{I} + \gamma_t \boldsymbol{e}_2 \otimes \boldsymbol{e}_1) \cdot \boldsymbol{U}_{t1}^{-1}$ (see Eq. (6.1)), respectively:

$$\boldsymbol{U}_{t1} = \begin{bmatrix} \alpha_1 & \alpha_2 & 0 \\ \alpha_2 & \alpha_3 & 0 \\ 0 & 0 & 1 \end{bmatrix}, \qquad \boldsymbol{Q} = \begin{bmatrix} \cos\vartheta & -\sin\vartheta & 0 \\ \sin\vartheta & \cos\vartheta & 0 \\ 0 & 0 & 1 \end{bmatrix}, \qquad \text{where} \tag{6.2}$$

$$\alpha_1 = \frac{q_2 q_4 + q_3 q_5}{2\sqrt{2} q_1}, \qquad \alpha_2 = \frac{q_5 - q_4}{\sqrt{2} q_1}, \qquad \alpha_3 = \frac{q_3 q_4 + q_2 q_5}{2\sqrt{2} q_1}, \qquad q_1 = \sqrt{4 + \gamma_t^2}, \qquad q_2 = q_1 - \gamma_t,$$
$$q_3 = q_1 + \gamma_t, \qquad q_4 = \sqrt{2 - q_2 \gamma_t}, \qquad q_5 = \sqrt{2 + q_3 \gamma_t}, \quad \text{and} \quad \tan\vartheta = \gamma_t/2. \tag{6.3}$$

We assume the austenite A is of a cubic lattice with the unit cell as shown in Fig. 2(a). From the Bain stretch tensor $\boldsymbol{U}_{t1}$ given by Eq. $(6.2)_1$, it is obvious that the martensitic variant M_1 is of monoclinic-II type (see Chapter 4 of [38] for details). The unit cells of A and M_1 are shown in Fig. 2(a) in an orthonormal basis $\{\boldsymbol{c}_1, \boldsymbol{c}_2, \boldsymbol{c}_3\}$, where the axes are parallel to three perpendicular sides of the A unit cell. The lattice parameters are also shown therein. Because the α_2 and α_3 given in Eq. (6.3) satisfy the condition $\alpha_2^2 + \alpha_3^2 = 1$, one of the sides of the unit cells of M_1 remains a_0 only as shown in Fig. 2(a). The cross-sections of the respective unit cells in the $\boldsymbol{c}_3$ direction are identical and their lengths in that direction are equal to a_0 (lattice parameter for cubic A). Fig. 2(b) shows the unit cells with respect to the basis $\{\boldsymbol{e}_1, \boldsymbol{e}_2, \boldsymbol{e}_3\}$, which is chosen for the sample shown in Fig. 3(a). The unit cells for this sample are obtained simply by rotating those of Fig. 2(a) counterclockwise about the $\boldsymbol{c}_3$-axis (or, equivalently, about the $\boldsymbol{e}_3$-axis) by an angle $\vartheta = \tan^{-1}(0.5\gamma_t)$; see Eq. $(6.3)_9$.

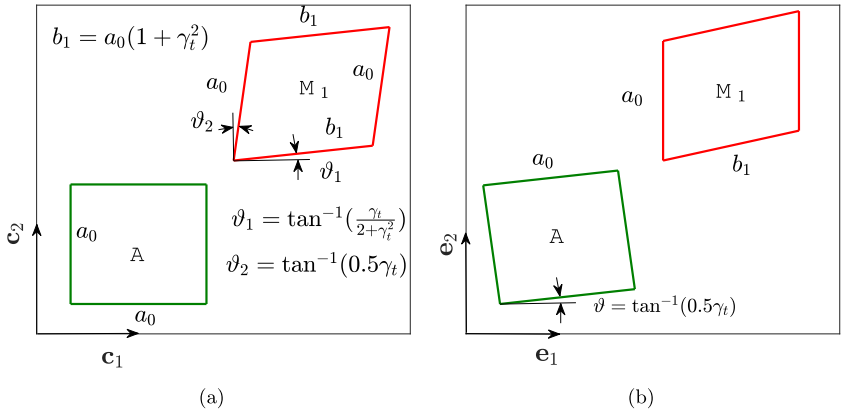

Fig. 2. Orientations of one of the faces of the unit cells of A and M_1 for the simple shear problem in Section 6.1 within a plane orthogonal to axes $\boldsymbol{c}_3$ or $\boldsymbol{e}_3$. Various lattice parameters are also shown as functions of the shear strain γ_t. (a) Cubic austenite and monoclinic-II martensite (M_1) unit cells with respect to an orthonormal basis $\{\boldsymbol{c}_1, \boldsymbol{c}_2, \boldsymbol{c}_3\}$ whose axes are parallel to three perpendicular sides of the A unit cell; (b) Orientations of the same unit cells in the basis $\{\boldsymbol{e}_1, \boldsymbol{e}_2, \boldsymbol{e}_3\}$ used in the computational domain, where both of the unit cells are obtained simply by rotating the unit cells of Fig. (a) counterclockwise by angle ϑ about $\boldsymbol{c}_3$, which is parallel to $\boldsymbol{e}_3$. The 3D unit cells in figures (a) and (b) both have similar cross-sections along the entire lengths in the out-of-plane direction ($\boldsymbol{c}_3$ or $\boldsymbol{e}_3$), and their lengths in that direction are equal to a_0.

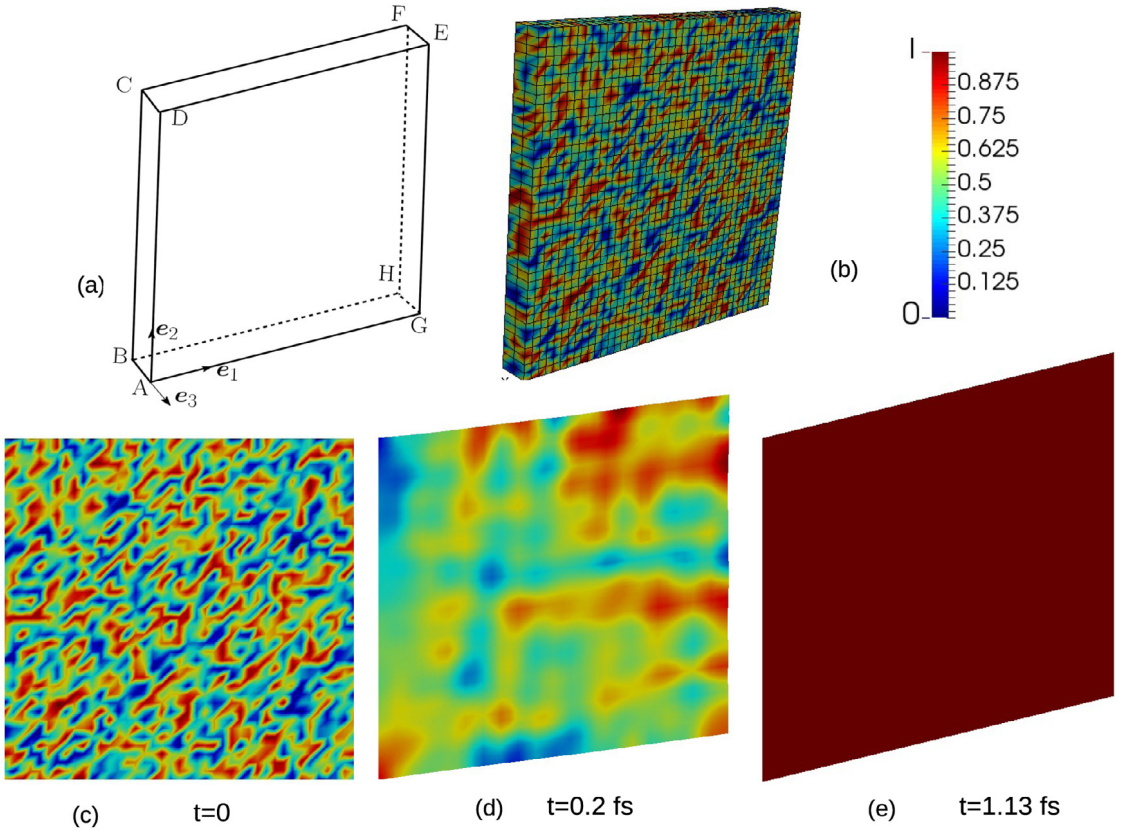

Fig. 3. Simple shear in a rectangular parallelepiped: (a) Schematic of the parallelepiped; (b) The undeformed 3D parallelepiped (Ω_0) showing the mesh density and the initial random distribution of η_0; (c) Front view (face ADEG) of the parallelepiped shown in (a) at $t = 0$; (d) Face ADEG in the deformed configuration Ω with a non-stationary intermediate solution of η_0 at an intermediate time step; (e) Face ADEG in Ω with a stationary distribution of $\eta_0 = 1$. The result is for $\boldsymbol{U}_t$ given by KM-I in Eq. (2.4).

6.1.2. Numerical results for simple shear in a parallelepiped

We now take a 10 nm $\times$10 nm $\times$1 nm parallelepiped as shown in 3(b) and use the Bain tensor given by Eq. $(6.2)_1$ in our phase field model to verify if this model can indeed yield a stress-free homogeneous fully martensitic sample within which $\boldsymbol{F}$ is given by Eq. (6.1). The transformations can obviously be described by a single order parameter η_0 in our phase field model. The Bain tensor given by Eq. $(6.2)_1$ is used in $\boldsymbol{F}_t$ corresponding to the respective kinematic models given by (derived from Eq. (2.4) and using $\eta_1 = 1$ therein), which are given as an input to the problem. The microstructure evolution can be determined by solving the Ginzburg–Landau equation $(2.20)_1$ and the equilibrium equations in (2.15) simultaneously. Note that the driving force X_0 (Eq. (2.21)) in the Ginzburg–Landau equation $(2.20)_1$ can be obtained in this case by substituting $\eta_1 = 1$ (since here M_1 is considered) in Eq. (2.21): Within the 3D parallelepiped, we take η_0 to be randomly distributed between 0 and 1 at $t = 0$; see Fig. 3(b) and (c), where the latter is the view of face ADEG at $t = 0$. The left end ABCD of the parallelepiped is fixed and all other faces are traction free, i.e. $u_1 = u_2 = u_3 = 0$ on ABCD; $P_{11} = P_{21} = P_{31} = 0$ on EFHG; $P_{13} = P_{23} = P_{33} = 0$ on ADEG and CFHB; $P_{12} = P_{22} = P_{32} = 0$ on CFED and ABHG. For η_0, the homogeneous Neumann boundary condition as discussed in Section 2.5 is used on the entire external boundary. The sample has been discretized uniformly with 400 quadratic 3D hexahedral elements (27-noded), which yield 15129 degrees of freedom (DOFs) for all of the displacements and 5043 DOFs for η_0, i.e. 20172 DOFs in total. We have taken $\Delta t^0 = 5$ fs, $\Delta t_{max} = 1$ µs, and $\Delta t_{min} = 5$ fs. The transformation stretch tensor Eq. $(6.2)_1$ is prescribed in the problem formulation considering $\gamma_t = 0.25$, while the rotation tensor $\boldsymbol{Q}$ is determined as a result of the solution. We take $\theta = 100$ K, which is constant in space and time. The adaptive time stepping described in Section 4.3 has been applied with the initial time step $\Delta t^0 = 5$ fs and the tolerance $\epsilon_{time} = 0.09$ (see Section 4.3).

We have shown the FE results in Fig. 3, where $\boldsymbol{U}_t$ is taken for the KM-I given by Eq. (2.4). Fig. 3(c) shows the front view (face ADEG) of the 3D parallelepiped with randomly distributed $0 \leq \eta_0 \leq 1$ at $t = 0$. Fig. 3(d) shows the same face of the sample in Ω at an intermediate time step depicting the inhomogeneous distribution of η_0. Fig. 3(e) shows the same face in Ω when η_0 has reached the stationary solution $\eta_0 = 1$ everywhere, yielding a fully martensite sample. A significant undercooling $\theta - \theta_e = -115$ K and the initial distribution of the elastic stresses promote martensite formation within the entire sample. The numerically-obtained components of the total deformation gradient $\boldsymbol{F}$ coincide with the analytical result discussed in Section 6.1.1, i.e.

$$\begin{aligned} &F_{11} = F_{22} = F_{33} = 1, \quad F_{12} = F_{13} = F_{31} = F_{23} = F_{32} = 0, \quad \text{and} \\ &F_{21} = 0.25 = \gamma_t \text{ for all } \boldsymbol{r}_0 \in \Omega_0. \end{aligned} \tag{6.4}$$

All of the stresses are vanishing, as expected within the crystallographic theory. While the stationary solution is trivial, the intermediate stages involve nontrivial microstructures, finite elastic strains, finite rotations, and large stresses; hence, the entire test is nontrivial. The simulation reached the stationary solution after 33 time stepping, where the final $\Delta t^{33} = 0.28$ ps and final time $t^f = 1.13$ ps. When the transformation rule given by KM-II is used, the same stationary solution is obtained, and the performance of the time stepping scheme is also approximately the same.

To analyze the performance of the adaptive time stepping scheme, we have solved this problem considering KM-I for three different values of the tolerance related to the adaptive time stepping: $\epsilon_{time} = 0.09,\ 0.06,\ 0.03$, where the same initial time step $\Delta t^0 = 5$ fs is used in all cases. We have also performed a simulation with constant time step $\Delta t = 5$ fs, which is obviously equal to Δt^0 taken for the simulations with variable Δt. In Fig. 4, the size of the time steps selected by the algorithm during the iterations is plotted against the time index n, which was introduced in Section 4.3. The number of iterations is the lowest when $\epsilon_{time} = 0.09$, increases as ϵ_{time} decreases, and is at its maximum when Δt is constant. From Fig. 4, it is clear that the maximum Δt^n attained in all of the variable time stepping chosen here are two orders of magnitude larger than the initial step size.

6.2. Twinning in martensite

We will now study twinning in a system with A and two martensitic variants M_1 and M_2. A brief review of the crystallographic equations will be presented in Section 6.2.1. The analytical solutions for these equations are listed in Section 3 of the supplementary material [70]; also see [38,71]. In Section 6.2.2, we will present the phase field results and compare them with the analytical solutions.

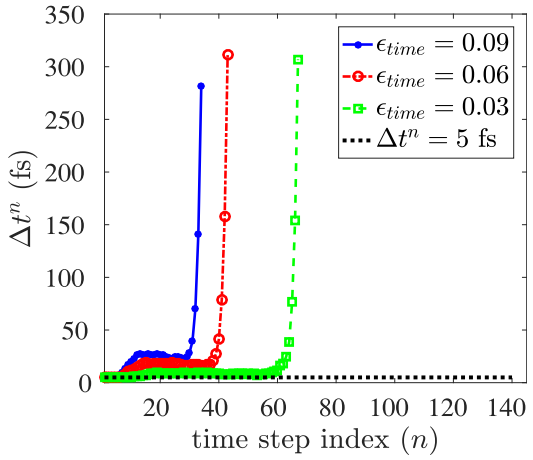

Fig. 4. A comparison of the time steps selected for different values of the tolerance for adaptive time stepping ϵ_{time} for the simple shear problem in Section 6.1. The time step index n was defined in Section 3.2, and the final value of the index represents the total number of iterations needed to obtain the stationary solutions.

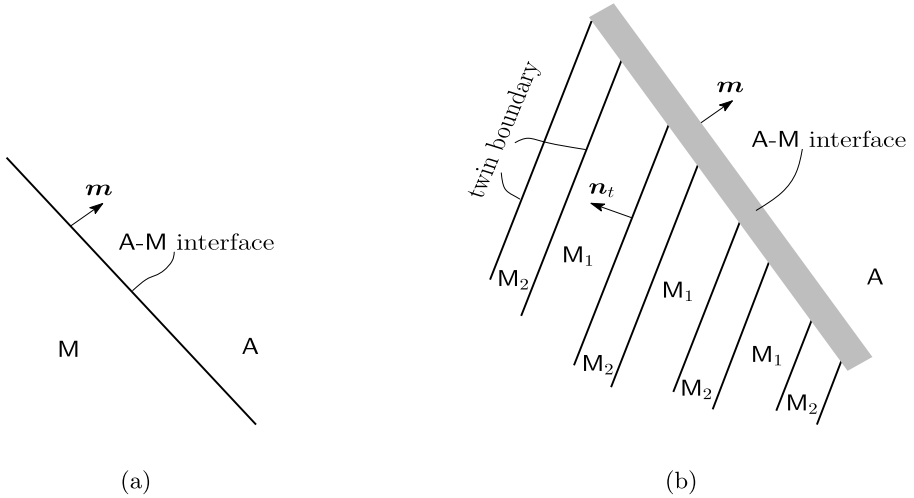

Fig. 5. A schematic of (a) austenite and single variant interface, where $\boldsymbol{m}$ is the unit normal to the A-M interface; (b) austenite–twinned martensite, where the shaded region is the A-M interface with unit normal $\boldsymbol{m}$, and $\boldsymbol{n}_t$ is the unit normal to the twin boundaries.

6.2.1. Crystallographic theory for twinning

According to the crystallographic theory, a sharp coherent interface between A and M (see Fig. 5(a) for a schematic) must satisfy the Hadamard's compatibility relation [38,71]

$$\boldsymbol{Q} \cdot \boldsymbol{U}_t - \boldsymbol{I} = \boldsymbol{c} \otimes \boldsymbol{m}, \tag{6.5}$$

where $\boldsymbol{U}_t$ is the transformation stretch tensor, $\boldsymbol{Q}$ is a rotation tensor, $\boldsymbol{c}$ is an arbitrary vector, and $\boldsymbol{m}$ is the unit normal to the A-M interface pointing into A. In Eq. (6.5), A is obviously assumed to be the reference stress-free crystal. The compatibility condition Eq. (6.5) requires one of the eigenvalues of $\boldsymbol{U}_t$ to be unity, which is too restrictive and is not satisfied in almost all materials [38]. Hence, we usually do not see an interface between A and a single M variant in experimental microstructures. Instead, the materials tend to form an austenite–twinned martensite interface; this is shown schematically in Fig. 5(b), which is the total elastic energy minimizer of the system [71]. Such an A-M interface has finite width and satisfies the Hadamard's compatibility condition in an average sense. The compatibility

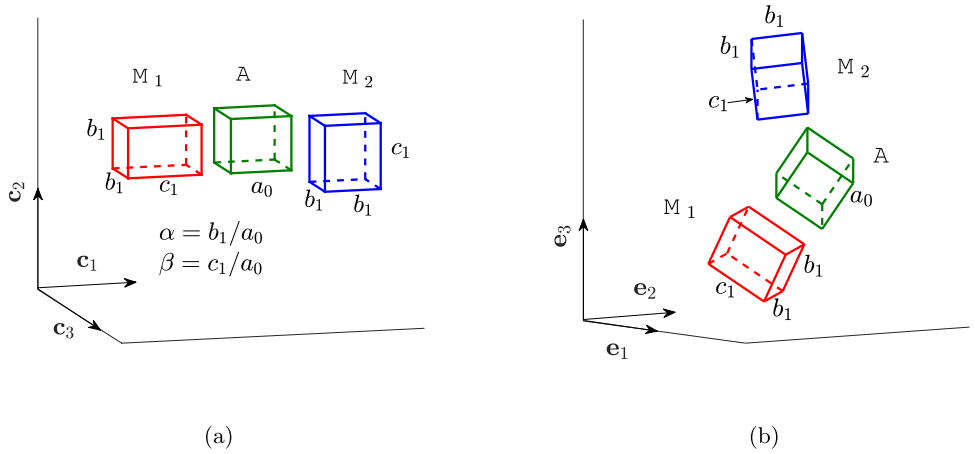

Fig. 6. Orientations of the unit cells of cubic A and tetragonal variants M_1 and M_2 for the twinning problem presented in Section 6.2. (a) The A, M_1, and M_2 unit cells in an orthonormal basis $\{\boldsymbol{c}_1, \boldsymbol{c}_2, \boldsymbol{c}_3\}$ with the axes parallel to three perpendicular sides of the A unit cell; (b) Orientations of the same unit cells in the orthonormal basis $\{\boldsymbol{e}_1, \boldsymbol{e}_2, \boldsymbol{e}_3\}$ (see Fig. 7).

equations for the twin boundaries and the A-twinned martensite interface shown in Fig. 5(b) are [38]

$$\boldsymbol{Q}_1 \cdot \boldsymbol{U}_{t2} - \boldsymbol{U}_{t1} = \boldsymbol{a} \otimes \boldsymbol{n}_t, \quad \text{and} \quad \boldsymbol{Q}_2 \cdot [\zeta \boldsymbol{Q}_1 \cdot \boldsymbol{U}_{t2} + (1-\zeta)\boldsymbol{U}_{t1}] = \boldsymbol{I} + \boldsymbol{b}_t \otimes \boldsymbol{m}, \tag{6.6}$$

respectively, where Eqs. $(6.6)_1$ and $(6.6)_2$ are also known as the twinning equation and the habit plane equation, respectively. In Eq. (6.6), $\boldsymbol{Q}_1$ and $\boldsymbol{Q}_2$ are two rotation tensors, $\boldsymbol{a}$ and $\boldsymbol{b}_t$ are two arbitrary vectors, $0 \leq \zeta \leq 1$ is the volume fraction of M_2 within the twins, and $\boldsymbol{n}_t$ and $\boldsymbol{m}$ are the unit normal vectors to the twin boundaries and A-M interface, respectively. Note that Eq. $(6.6)_2$ coincides with Eq. (6.5) when the variant M_2 is absent (i.e. $\zeta = 0, \boldsymbol{Q}_2 = \boldsymbol{Q}$, and $\boldsymbol{c} = \boldsymbol{b}_t$) or, alternatively, when M_1 is absent, i.e. $\zeta = 1, \boldsymbol{Q}_2 \cdot \boldsymbol{Q}_1 = \boldsymbol{Q}$, and $\boldsymbol{c} = \boldsymbol{b}_t$.

In Eq. (6.6), the Bain tensors $\boldsymbol{U}_{t1}$ and $\boldsymbol{U}_{t2}$ for any pairs of variants are known for a given material. Given these parameters, the other unknowns $\boldsymbol{a}$, $\boldsymbol{b}_t$, $\boldsymbol{n}_t$, $\boldsymbol{m}$, and ζ in Eq. (6.6) can be solved (see [38,71] for the derivation). For completeness, a list of the solutions is provided in Section 3 of the supplementary material [70]. The rotation tensors $\boldsymbol{Q}_1$ and $\boldsymbol{Q}_2$ can be determined by substituting the solutions from Section 3 of the supplementary material into Eqs. $(6.6)_{1,2}$. Obviously, all of the analytical solutions depend on the components of the Bain tensors which are the material parameters [38]. Noticing that the deformation gradients within the stress-free A, M_1, and M_2 are $\boldsymbol{F}_0 = \boldsymbol{I}$, $\boldsymbol{F}_1 = \boldsymbol{Q}_2 \cdot \boldsymbol{U}_{t1}$, and $\boldsymbol{F}_2 = \boldsymbol{Q}_2 \cdot \boldsymbol{Q}_1 \cdot \boldsymbol{U}_{t2}$, respectively, we write the average deformation gradient within a sample consisting of A and a mixture of M_1 and M_2 as [25]

$$\boldsymbol{F}_{av} = \zeta_0 \boldsymbol{F}_0 + (1-\zeta_0)[\zeta \boldsymbol{F}_2 + (1-\zeta)\boldsymbol{F}_1] = \boldsymbol{I} + (1-\zeta_0)\boldsymbol{b}_t \otimes \boldsymbol{m}, \tag{6.7}$$

where ζ_0 is the volume fraction of A within the sample and Eq. $(6.7)_2$ is obtained by applying Eq. $(6.6)_2$ in Eq. $(6.7)_1$. Note that Eq. (6.7) will be used in our numerical calculations in Section 6.2.2 to determine the boundary displacements that will be applied on a sample to obtain the desired twinned microstructures.

6.2.2. *Computational details and results for twinning*

We will now present the phase field simulation results and compare them with the analytical solutions. Material properties for NiAl, which has cubic austenite and tetragonal martensitic variants, will be used. The samples are at a constant temperature $\theta = \theta_e = 215$ K. Because we consider a two-variant system, the twinning phenomenon in our phase field approach can obviously be described using two independent order parameters η_0 and η_1. The governing coupled phase field and elasticity equations, which are listed in Section 2, simplify to those listed in Section 2 of the supplementary material [70]. Of the three Bain tensors for NiAl, we choose the following two without loss of generality (see Chapter 4 of [38]):

$$\boldsymbol{U}_{t1} = diag(\beta, \alpha, \alpha), \quad \text{and} \quad \boldsymbol{U}_{t2} = diag(\alpha, \beta, \alpha), \tag{6.8}$$

where $\alpha = 0.922$ and $\beta = 1.215$, as taken from the atomistic simulation results; see [67] and the references therein. The other material parameters are listed in Section 5. The unit cells of the cubic A and the two variants used here are shown in Fig. 6(a) in the basis $\{\boldsymbol{c}_1, \boldsymbol{c}_2, \boldsymbol{c}_3\}$, where the axes are parallel to three perpendicular sides of the A unit cell. The lattice parameters and their relations to the material constants α and β are also given therein (also see Chapter 4 of [38]). The solutions of $\boldsymbol{a}$, $\boldsymbol{b}_t$, $\boldsymbol{m}$, $\boldsymbol{n}_t$, and ζ for the Bain stretches given by Eq. (6.8) are listed in Section 3 of the supplementary material [70].

If the twinned microstructure is viewed within the plane made by the vectors $\boldsymbol{m}$ and $\boldsymbol{n}_t$ (see Section 3 of [70] their expressions), one can show that the microstructure is independent of the coordinate along the direction perpendicular to this plane. To verify this, let us consider another orthonormal basis $\{\boldsymbol{e}_1, \boldsymbol{e}_2, \boldsymbol{e}_3\}$ where the basis vectors $\boldsymbol{e}_1$ and $\boldsymbol{e}_2$ lie in the plane made by $\boldsymbol{m}$ and $\boldsymbol{n}_t$ and the twin boundary normal is parallel to $\boldsymbol{e}_1$, i.e. $\boldsymbol{n}_t' = \boldsymbol{R}' \cdot \boldsymbol{n}_t = \boldsymbol{e}_1$ (see Fig. 7), where the rotation

$$\boldsymbol{R}' = \begin{bmatrix} -0.7071 & 0.7071 & 0 \\ -0.5105 & -0.5105 & -0.6920 \\ -0.4893 & -0.4893 & 0.7219 \end{bmatrix} \quad \text{in } \{\boldsymbol{c}_1, \boldsymbol{c}_2, \boldsymbol{c}_3\} \text{ basis.} \tag{6.9}$$

Using the vectors $\boldsymbol{b}_t$ and $\boldsymbol{m}$ from Table 1 and rotating them by $\boldsymbol{R}'$ we calculate the average distortion within the mixture by using Eq. (6.7) for a NiAl sample shown schematically in Fig. 7:

$$\begin{aligned} (\nabla \boldsymbol{u})'_{av} &= \boldsymbol{F}'_{av} - \boldsymbol{I} = (1-\zeta_0)\, \boldsymbol{R}' \cdot \boldsymbol{b}_t \otimes \boldsymbol{R}' \cdot \boldsymbol{m} \\ &= (1-\zeta_0) \begin{bmatrix} 0.0414 & 0.0765 & 0 \\ -0.0046 & -0.0086 & 0 \\ 0.0847 & 0.1564 & 0 \end{bmatrix} \quad \text{in } \{\boldsymbol{c}_1, \boldsymbol{c}_2, \boldsymbol{c}_3\} \text{ basis,} \end{aligned} \tag{6.10}$$

where we recall that ζ_0 is the volume fraction of A. If we now consider the position vector of a particle lying in the $\boldsymbol{m}$-$\boldsymbol{n}_t$ plane with respect to the basis $\{\boldsymbol{e}_1, \boldsymbol{e}_2, \boldsymbol{e}_3\}$, its average deformation would be independent of the coordinate along the $\boldsymbol{e}_3$-direction, although the displacement in that direction is non-trivial. The orientations of all of the unit cells with respect to the basis $\{\boldsymbol{e}_1, \boldsymbol{e}_2, \boldsymbol{e}_3\}$ are shown in Fig. 6(b). The orientations are obtained by rotating the unit cells from Fig. 6(a) by using the rotation matrix $\boldsymbol{R}'$ given by Eq. (6.9).

Based on this observation, we performed our numerical calculations in the domain designated by ABCD as shown in Fig. 7 with the basis $\{\boldsymbol{e}_1, \boldsymbol{e}_2, \boldsymbol{e}_3\}$. The microstructure is obviously expected to be independent on r_{03}, i.e. all of the displacement components are functions of r_{01} and r_{02} only: $\boldsymbol{u} = u_a(r_{01}, r_{02})\boldsymbol{e}_a$. The generalized plane strain approach has been used here for solving the system of equations (also see e.g. [26]). Such a 2D computational domain allows us to consider a larger sample without sacrificing the accuracy of the solutions. The stress and strain tensors are obviously full 3×3 matrices. The Bain tensors of Eq. (6.8) transformed by the tensor $\boldsymbol{R}'$ are used in FE calculations $\boldsymbol{U}'_{ti} = \boldsymbol{R}' \cdot \boldsymbol{U}_{ti} \cdot \boldsymbol{R}'^T$:

$$\boldsymbol{U}'_{t1} = \begin{bmatrix} 1.0685 & 0.1058 & 0.1014 \\ 0.1058 & 0.9983 & 0.0732 \\ 0.1014 & 0.0732 & 0.9922 \end{bmatrix}, \quad \text{and} \quad \boldsymbol{U}'_{t2} = \begin{bmatrix} 1.0685 & -0.1058 & -0.1014 \\ -0.1058 & 0.9983 & 0.0732 \\ -0.1014 & 0.0732 & 0.9922 \end{bmatrix}. \tag{6.11}$$

Recall that KM-II involves the exp-ln transformation stretch tensor. Thus the Ginzburg–Landau equations and the linearizations listed in Section 3 and Appendix B involve the derivatives of the logarithm and exponential of the nondiagonal tensors. The explicit forms of the first and second derivatives of $\boldsymbol{F}_t$ with respect to the order parameters for KM-II are listed in the supplementary material [70]. The derivation of the same for KM-I is straightforward and hence not shown.

We have controlled the microstructures in our numerical calculations by applying the displacements at all external boundaries corresponding to the average $\nabla \boldsymbol{u}'_{av}$

$$\boldsymbol{u}|_{S_0} = \boldsymbol{u}_{av} = (\nabla \boldsymbol{u})'_{av} \cdot \boldsymbol{r}_0 \qquad \text{for all } \boldsymbol{r}_0 \in S_0, \tag{6.12}$$

where $(\nabla \boldsymbol{u})'_{av}$ is taken from Eq. (6.10). Simulations have been performed for both KM-I and KM-II, where the Bain tensors are given by Eq. (6.11). Because AB and CD are the invariant planes, the twin plates are expected to occupy the entire slab, i.e. there would be almost no residual austenite. Thus we take $\zeta_0 = 0$ in Eqs. (6.10) and (6.12) and obtain the boundary displacements accordingly. There is obviously no traction boundary condition for this problem. The homogeneous Neumann boundary conditions for the order parameters as discussed in Section 2.5 are used on the

Table 1
Crystallographic solutions for NiAl in cubic lattice coordinate with basis $\{\boldsymbol{c}_1, \boldsymbol{c}_2, \boldsymbol{c}_3\}$.

$\boldsymbol{n}_t$	$-0.7071\,\boldsymbol{c}_1 + 0.7071\,\boldsymbol{c}_2$
$\boldsymbol{a}$	$0.4625\,\boldsymbol{c}_1 + 0.3510\,\boldsymbol{c}_2$
ξ	0.3046
$\boldsymbol{b}_t$	$-0.1436\,\boldsymbol{c}_1 - 0.0205\,\boldsymbol{c}_2 + 0.1351\,\boldsymbol{c}_3$
$\boldsymbol{m}$	$-0.7855\,\boldsymbol{c}_1 - 0.1122\,\boldsymbol{c}_2 - 0.6085\,\boldsymbol{c}_3$

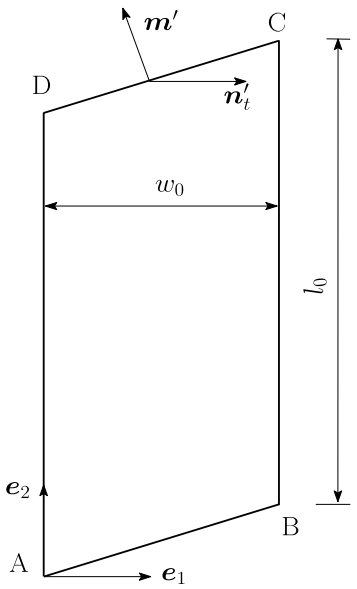

Fig. 7. Schematic of the sample in Ω_0 considered for the twinning problem.

surfaces AB, BC, CD, and AD. In all samples η_0 and η_1 are assumed to initially be distributed randomly between 0 and 1.

An effective order parameter $\eta_{eq} = 2\eta_0(\eta_1 - 0.5)$ is defined, which obviously satisfies $\eta_{eq} = 0$ in A, $\eta_{eq} = 1$ in M_1, and $\eta_{eq} = -1$ in M_2. The initial samples have been discretized using 9-noded 2D quadratic elements in a manner such that at least four grid points are present within the A-M interfaces and twin interfaces (see Section 5 for their widths). We have used $\epsilon_{time} = 0.07$ for all of the simulations with samples in (i)–(iv) of Figs. 8 and 9 and $\epsilon_{time} = 0.04$ was used for samples in (v). In all simulations we have chosen $\Delta t^0 = 2$ fs, $\Delta t_{max} = 1\,\mu$s, and $\Delta t_{min} = 2$ fs.

In Figs. 8 and 9 the color plots of stationary η_{eq} in different size samples are shown in the deformed configuration Ω. The color dark red ($\eta_{eq} = 1$) indicates M_1 plates and dark blue ($\eta_{eq} = -1$) indicates M_2 plates. The color green with $\eta_{eq} = 0$ may indicate either a point on the M_1-M_2 interface (i.e. $\eta_1 = 0.5$) or within A (i.e. $\eta_0 = 0$). The laminated twin plates are formed between the invariant planes. The austenite phase is absent from the stationary microstructures except in very small regions between the martensitic plates and the invariant planes (shown in green in Figs. 8 and 9).

We now present a comparison between the analytical and numerical results. The volume fraction of the variants has been calculated along a line which passes through the middle of the sample and is parallel to the side AB, where the particles are martensite. We have measured the total length ℓ_1 of the segments within which $0.95 \leq \eta_1 \leq 1$, i.e. the phase is M_1, and have also measured the total length ℓ_2 of the segments within which $0 \leq \eta_1 \leq 0.05$, i.e. the phase is M_2. The volume fraction of M_2 in the mixture of M_1 and M_2 is then calculated using $\ell_2/(\ell_1 + \ell_2)$. The volume fraction of M_2 within the twinned samples shown in both Fig. 8(V) and 9(V) is calculated to be approximately 0.27, which is close to the crystallographic solution for sharp interfaces 0.3 (see Table 1). Consideration of the larger sample with a smaller area of the interfaces should reduce the deviation. We have also determined the normal vectors to the twin boundaries in the middle of the samples, and the maximum deviation of alignment of these normals from the $\boldsymbol{e}_1$-direction is less than 1° . The twin boundary widths are also close to the analytical value $\delta_{12} = 0.75$ nm. For both

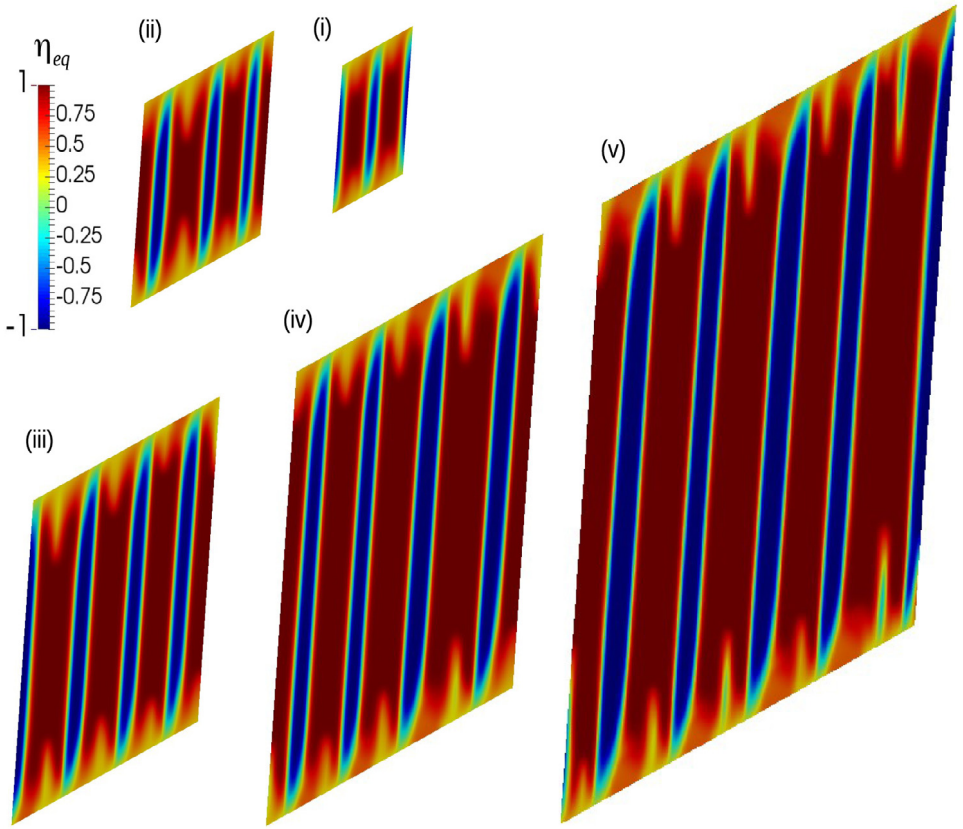

Fig. 8. Twining in martensite solution (plots for η_{eq}) for KM-I in samples of size (i) $w_0 = 5$ mm, $l_0 = 10$ mm, (ii) $w_0 = 10$ mm, $l_0 = 15$ mm, (iii) $w_0 = 15$ mm, $l_0 = 25$ mm, (iv) $w_0 = 20$ mm, $l_0 = 35$ mm, and (v) $w_0 = 30$ mm, $l_0 = 50$ mm. The results are plotted in the deformed configuration Ω. $\eta_{eq} = 1$ and $\eta_{eq} = -1$ signify M_1 and M_2, respectively. (For interpretation of the references to color in this figure legend, the reader is referred to the web version of this article.)

KM-I and KM-II, we see from Figs. 8 and 9 that the number of martensitic plates generally increases as the sample size increases. The number of martensitic plates (N_{plate}) and the average width of these plates (w_p) are proportional to the square root of the sample size w_0, i.e. $N_{plate} \sim \sqrt{w_0}$ and $w_p \sim \sqrt{w_0}$; see Stupkiewicz and coworkers [25,26]. As the sample size increases, there is a rising tendency to form twin branches within the A-M interfaces, which is clearly observed in cases (v) of Figs. 8 and 9 (also see [25,26]). Such twin branching reduces the effective twin plate size and increases the total twin interface area. This results in a decrease of the elastic energy and an increase of the total twin boundary energy. Obviously, in the process of branching, the reduction of the elastic energy is more prominent and the overall energy of the system thus reduces. The maximum time step sizes attained in all cases lie between 10 ns to 100 ns, i.e. the step size increases up to *eight orders of magnitude* from the initial value.

In Figs. 10(a) and 10(b), we show the variation of normal elastic $\sigma_{(e)22}$ and structural stresses $\sigma_{(st)22}$ along a line which is parallel to the side AB (see Fig. 7) and passing through the middle of the sample, both for KM-I and II (samples (v) from Figs. 8 and 9 are taken). These stresses obviously act along the twin boundaries, i.e. parallel to the $\boldsymbol{e}_2$-direction. Notably, the elastic stress is much larger than the structural stress in both cases, and the magnitude of $\sigma_{(e)22}$ is also much larger for KM-II than for KM-I. The origin of the elastic stress $\sigma_{(e)22}$ within the twin boundaries and the reason for larger elastic stress for KM-II than KM-I have been already studied by the authors in [53], both analytically and numerically. Note that the elastic stress within the twin boundaries is vanishing according to the crystallographic theory which is a purely geometrical theory and considers twin boundaries to be sharp interfaces. However, in the phase field approach such interfaces have finite width and the transformation strains within them are inhomogeneous. In Figs. 10(a) and 10(b), note that $\sigma_{(e)22}$ is in fact much smaller within the variants. Furthermore, it was shown in [53] that, although the elastic stress obtained by using our two kinematic models is large within the twin

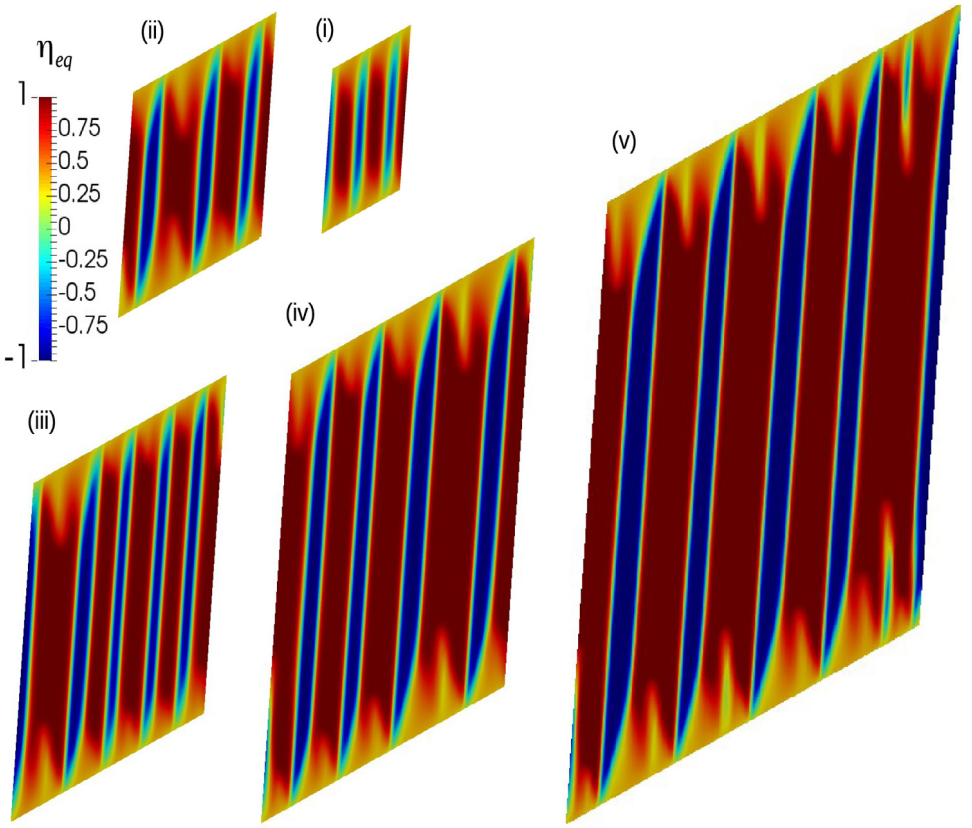

Fig. 9. Twinning in martensite (plots for η_{eq}) for KM-II in samples of size (i) $w_0 = 5$ mm, $l_0 = 10$ mm, (ii) $w_0 = 10$ mm, $l_0 = 15$ mm, (iii) $w_0 = 15$ mm, $l_0 = 25$ mm, (iv) $w_0 = 20$ mm, $l_0 = 35$ mm, and (v) $w_0 = 30$ mm, $l_0 = 50$ mm. The results are plotted in the deformed configuration Ω. $\eta_{eq} = 1$ and $\eta_{eq} = -1$ signify M_1 and M_2, respectively. (For interpretation of the references to color in this figure legend, the reader is referred to the web version of this article.)

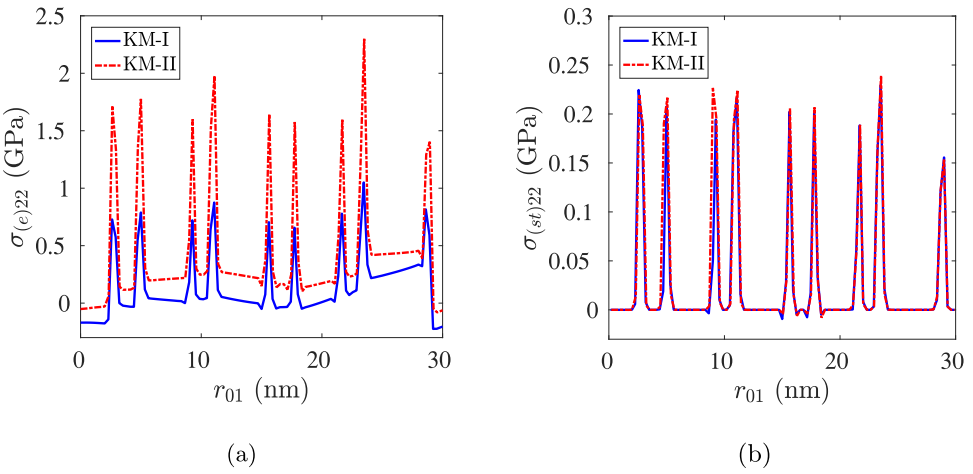

Fig. 10. Elastic and structural stress components $\sigma_{(e)22}$ and $\sigma_{(st)22}$ along a line, which is parallel to the invariant planes AB and CD passing through the middle of the reference sample, both for KM-I and KM-II.

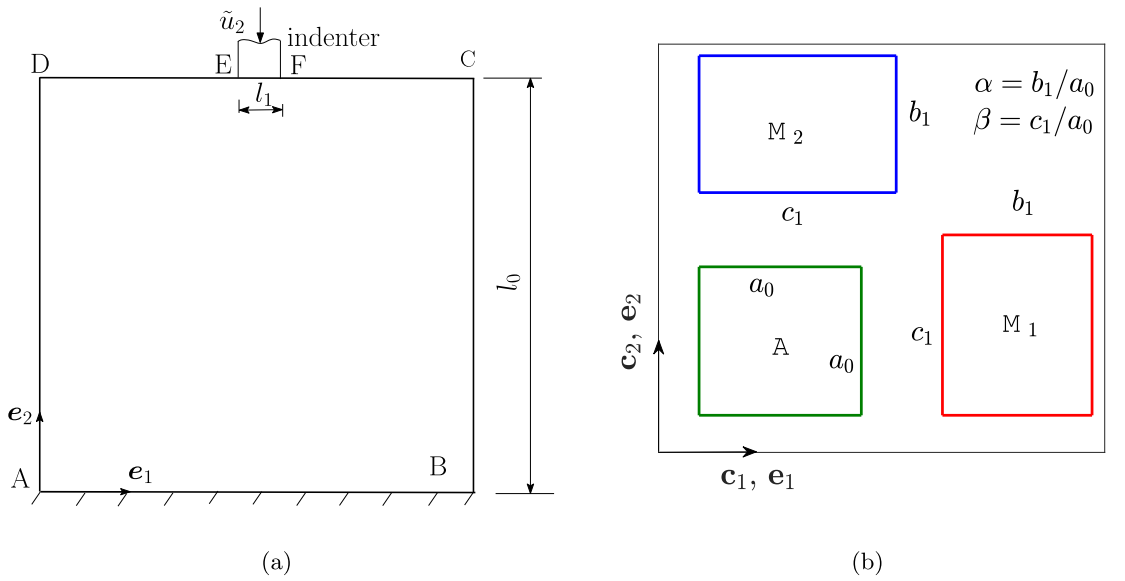

Fig. 11. Sample under indentation by a flat and rigid indenter: (a) Schematic of the sample; (b) The A, M_1, M_2 unit cell orientations in an orthonormal basis $\{\boldsymbol{c}_1, \boldsymbol{c}_2\}$ with the axes parallel to the sides of the A unit cell. The basis $\{\boldsymbol{e}_1, \boldsymbol{e}_2\}$ taken within the reference sample Ω_0 coincides with $\{\boldsymbol{c}_1, \boldsymbol{c}_2\}$.

boundaries, the net interfacial tension vanishes in the sharp interface limit. The nature of elastic stresses within the realistic twin interfaces is yet to be verified, either experimentally or by using the atomistic simulations.

In physical and material literature, the spectral methods are usually used to study martensitic microstructure evolution [18,32,34,48]. The problem formulation naturally includes periodic boundary conditions, and applying other types of boundary conditions is problematic. Because any boundary conditions can be applied in the finite element method, we choose a non-periodic condition for the displacements given by Eq. (6.12) for an isolated sample and the homogeneous Neumann boundary conditions for the order parameters. However, if one considers a periodic cell, the condition given by [26] $\boldsymbol{u}|_{S_0} = (\boldsymbol{F}_{av} - \boldsymbol{I}) \cdot \boldsymbol{r}_0 + \hat{\boldsymbol{u}}$ for all $\boldsymbol{r}_0$ on S_0 and the periodic boundary condition for the order parameters should be used, where $\hat{\boldsymbol{u}}$ is the fluctuation of the displacement vector on corresponding periodic boundaries. Both the cases yield laminated microstructures, but the solutions would obviously be different. Examples of microstructures with the boundary condition given by Eq. (6.12) can also be found in [26], and the microstructures using the periodic boundary condition can be seen in [25].

6.3. Indentation problem

We will now study the microstructure evolution in a 40 nm×40 nm 2D rectangular block ABCD subjected to nanoindentation by a flat and rigid indenter as shown in Fig. 11(a). Evolution of austenite and two martensitic variants is studied. The governing equations for a two-variant system listed in [70] are used, assuming the plane stress condition. The specialized elasticity equations under the plane stress condition can be found in a recent paper by the authors [45]. The bottom surface of the sample AB is held fixed ($u_1 = u_2 = 0$), and a downward uniform vertical indentation displacement of magnitude $\hat{u}_2 = 1.5$ nm is applied at the middle of the top surface (at region EF) over a span of $l_1 = 8$ nm. Within this indenting region, the tangential component of the traction vector is zero (i.e. $P_{12} = 0$). The rest of this boundary (regions DE and FC) is traction-free, i.e. $P_{12} = P_{22} = 0$ therein. The vertical surfaces AD and BC are both traction free, i.e. $P_{11} = P_{21} = 0$. The homogeneous Neumann boundary conditions for η_0 and η_1 on all external surfaces are applied (see Section 2.5). The Bain tensors for the variants M_1 and M_2 in NiAl are taken to be $\boldsymbol{U}_{t1} = diag(\alpha, \beta, \alpha)$ and $\boldsymbol{U}_{t2} = diag(\beta, \alpha, \alpha)$, where $\alpha = 0.922$ and $\beta = 1.215$ [53]; and the material properties in Section 5 are used. The temperature is taken to be $\theta = 0$. The orientations of the unit cells of A, M_1, and M_2 with respect to the basis $\{\boldsymbol{c}_1, \boldsymbol{c}_2\}$ (the axes coincide with the perpendicular sides of the cubic A) and the basis $\{\boldsymbol{e}_1, \boldsymbol{e}_2\}$ (taken for the 2D sample and coincident with the basis $\{\boldsymbol{c}_1, \boldsymbol{c}_2\}$) are shown in Fig. 11(b). We consider a semi-circular

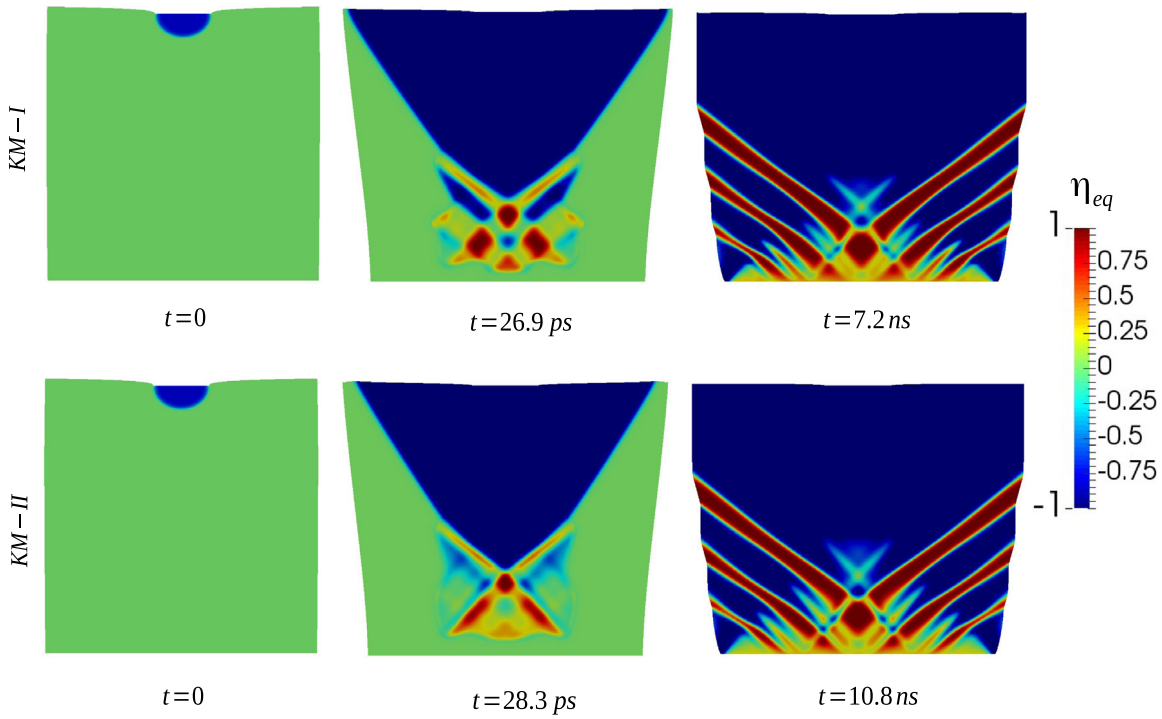

Fig. 12. The plot of η_{eq} for the indentation problem for KM-I (first row) and KM-II (second row) in the deformed configuration Ω.

M nucleus (i.e. $\eta_0 = 1$) in the middle of the top surface at $t = 0$, and A (i.e. $\eta_0 = 0$) in the rest of the sample; see the first column in Fig. 12, where η_{eq} color plots are shown. The initial value of η_1 is taken to be 0.1 everywhere, $\Delta t^0 = 10$ fs, $\Delta t_{max} = 1\,\mu$s, and $\Delta t_{min} = 10$ fs. The microstructure evolution for KM-I and for KM-II are shown in Fig. 12. The color scheme is the same as that considered for the twinning problem in Section 6.2. The second column shows the microstructure in an intermediate time instance, and the last column shows the stationary microstructures. Although the intermediate microstructures for KM-I and for KM-II differ, the stationary solutions for both models are almost identical. Because the applied displacement yields a compressive load in the sample and the direction of the compressive load coincides with the compression axis of the variant M_2 (see Fig. 11(b)), the variant M_2 is promoted and it spreads over a broad region, as reflected in the figures of column 2. As it approaches the bottom surface, which is fixed, the other variant M_1 also appears. In the stationary microstructures, plates of alternating variants are formed in the lower halves of the samples, whereas the upper halves are fully M_2.

7. Concluding remarks

A rigorous and detailed FE procedure for solving a new coupled system of mechanical equilibrium equations and Ginzburg–Landau equations has been derived for studying the multivariant MTs induced by stresses and temperature at finite strains and with interfacial stresses. The formulation considers austenite and N martensitic variants. A non-monolithic strategy has been used for solving the mechanical equilibrium equations and N independent Ginzburg–Landau equations using the implicit methods. To this end, the weak forms for the equilibrium equations and each of the Ginzburg–Landau equations are derived, and they are linearized to obtain the tangent matrices. The correct tangent modulus tensor for the mechanical equilibrium equation has been obtained and consists of the parts due to the elastic stresses and the structural stresses. An adaptive time stepping, for which the time step sizes can increase by several orders of magnitude, is implemented. Using the present algorithm, a nonlinear FE code has been developed and used to study (i) the simple shear deformation in a 3D parallelepiped with austenite and a single variant, (ii) the twinning in martensite and sample size dependency of the twinned microstructure, and (iii) the microstructure evolution under nanoindentation. The numerical results for the first two problems are in agreement with the analytical solutions, which

are well known. Two different kinematic models for the transformation deformation gradient tensor are used to study the microstructure evolutions. The elastic and structural parts of the interfacial stresses within the twin boundaries are also analyzed. The advantage of the present non-monolithic scheme is that a large number of M variants can be handled easily; however, with a monolithic scheme, the complexity in the algorithm and procedure would increase significantly with an increasing number of variants.

It should be mentioned that the detailed computational procedures for some of our other phase field models [21,29,31,50] were not provided. The present study can be easily used to develop the detailed FE algorithms for those models. Furthermore, our FE procedure to PF can be extended for studies of grain growth, solidification, crack propagation, diffusive PTs, interaction between MTs, plasticity, and/or fracture etc. Also note that a more detailed model for single-variant martensitic PTs has recently been developed [73] with a focus on the lattice instability conditions [30,31]. These conditions, under a general loading with all six components of the stress tensor, are found using the molecular dynamics simulations (see [73] and the references therein). That model must be generalized for multivariant martensitic PTs, and the corresponding finite element algorithm should be developed by a method similar to the approach used here.

Acknowledgments

The support from ARO (W911NF-17-1-0225), NSF (CMMI-1536925 and DMR-1434613), ONR (N00014-16-1-2079), and Iowa State University (Vance Coffman Faculty Chair Professorship) is gratefully acknowledged. The simulations were performed at Extreme Science and Engineering Discovery Environment (XSEDE), allocations TG-MSS140033 and MSS170015.

Appendix A. N independent Ginzburg–Landau equations

Because we use a fully implicit non-monolithic scheme to solve the coupled Ginzburg–Landau equations in Eq. (2.20), it is necessary to differentiate the right-hand side (which may be a function of all N order parameters related to the variants) of the corresponding equation, say, the equation for $\dot{\eta}_i$ with respect to η_i, to determine the tangent matrix for Newton's iteration. Thus, it is necessary to express all of the conjugate forces X_i $(i = 0, 1, \ldots, N)$ as functions of $N-1$ independent order parameters related to the variants. Without loss of generality, we eliminate η_N from those expressions by using $\eta_N = 1 - \sum_{j=1}^{N-1} \eta_j$ and express $(2.20)_1$ and the first $N-1$ Ginzburg–Landau equations from $(2.20)_2$ in their equivalent forms:

$$\dot{\eta}_0 = L_{0M}\overline{X}_0, \qquad \dot{\eta}_i = \sum_{j=1,\neq i}^{N} L_{ij}(\overline{X}_i - \overline{X}_j) \quad \text{for } i = 1, 2, \ldots, N-1, \tag{A.1}$$

where all of the functions (scalar, vector, and tensor) with over-bar are expressed in terms of the $N-1$ independent order parameters $\eta_0, \eta_1, \ldots, \eta_{N-1}$, i.e. $\overline{g}(\eta_0, \eta_1, \ldots, \eta_{N-1}) = g\left(\eta_0, \eta_1, \ldots, 1 - \sum_{j=1}^{N-1}\eta_j\right)$ for any function $g(\eta_0, \eta_1, \ldots, \eta_N)$. The explicit expressions for $\overline{X}_0$ and $\overline{X}_i$ (for all $i = 1, 2, \ldots, N$) are

$$\begin{aligned}
\overline{X}_0 = {} & \left(\boldsymbol{P}_e^T \cdot \boldsymbol{F} - \bar{J}_t \psi_e \boldsymbol{I}\right) : \overline{\boldsymbol{F}}_t^{-1} \cdot \overline{\frac{\partial \boldsymbol{F}_t}{\partial \eta_0}} - \overline{J}_t \left.\overline{\frac{\partial \psi_e}{\partial \eta_0}}\right|_{\boldsymbol{F}_e} - \rho_0(6\eta_0 - 6\eta_0^2)\Delta\psi^\theta - J\rho_0\tilde{A}\left(\sum_{i=1}^{N-2}\sum_{j=i+1}^{N-1}\eta_j^2\eta_i^2 + \right. \\
& \left.\sum_{i=1}^{N-1}\eta_i^2\eta_N^2\right)\frac{\partial\varphi(a_b,\eta_0)}{\partial\eta_0} - J\rho_0[A_{0M}(\theta) + (a_\theta - 3)\Delta\psi^\theta(\theta)](2\eta_0 - 6\eta_0^2 + 4\eta_0^3) - \frac{J}{8}\frac{\partial\tilde{\varphi}(a_\beta, a_c, \eta_0)}{\partial\eta_0} \times \\
& \left(\sum_{i=1}^{N-2}\sum_{j=i+1}^{N-1}\beta_{ij}|\nabla\eta_i - \nabla\eta_j|^2 + \sum_{i=1}^{N-1}\beta_{iN}\left|\nabla\eta_i + \sum_{j=1}^{N-1}\nabla\eta_j\right|^2\right) \\
& - \rho_0\left[\sum_{i=1}^{N-2}\sum_{j=i+1}^{N-1}K_{0ij}\eta_i^2\eta_j^2 + \sum_{i=1}^{N-1}K_{0iN}\eta_i^2\eta_N^2\right. \\
& \left. + \sum_{i=1}^{N-3}\sum_{j=i+1}^{N-2}\sum_{k=j+1}^{N-1}K_{0ijk}\eta_i^2\eta_j^2\eta_k^2 + \sum_{i=1}^{N-2}\sum_{j=i+1}^{N-1}K_{0ijN}\eta_i^2\eta_j^2\eta_N^2\right]
\end{aligned}$$

$$\times\left[2(1-\varphi(a_K,\eta_0))\eta_0-\frac{\partial\varphi(a_K,\eta_0)}{\partial\eta_0}\eta_0^2\right]+$$
$$\nabla_0\cdot\left(J\beta_{0M}\boldsymbol{F}^{-1}\cdot\nabla\eta_0\right),\quad\text{and}\tag{A.2}$$

$$\begin{aligned}\overline{X}_i=&\left(\boldsymbol{P}_e^T\cdot\boldsymbol{F}-\bar{J}_t\psi_e\boldsymbol{I}\right):\overline{\boldsymbol{F}}_t^{-1}\cdot\overline{\frac{\partial\boldsymbol{F}_t}{\partial\eta_i}}-\overline{J}_t\overline{\frac{\partial\psi_e}{\partial\eta_i}}\Bigg|_{\boldsymbol{F}_e}\\&-2J\rho_0\tilde{A}\left(\sum_{j=1,\neq i}^{N-1}\eta_j^2+\eta_N^2\right)\eta_i\varphi(a_b,\eta_0)-2\rho_0\sum_{j=1}^{N-1}K_{ij}\times\\&(\eta_i+\eta_j-1)(2\eta_i+\eta_j-1)\eta_j^2\eta_i-2\rho_0K_{iN}(\eta_i+\eta_N-1)(2\eta_i+\eta_N-1)\eta_i\eta_N^2\\&-2\rho_0\left(\sum_{j=1}^{N-1}K_{0ij}\eta_j^2+K_{0iN}\eta_N^2+\right.\\&\left.\sum_{j=1}^{N-2}\sum_{k=j+1}^{N-1}K_{0ijk}\eta_j^2\eta_k^2+\sum_{j=1}^{N-1}K_{0ijN}\eta_j^2\eta_N^2\right)\eta_0^2\eta_i(1-\varphi(a_K,\eta_0))\\&-2\rho_0\left(\sum_{j=1}^{N-2}\sum_{k=j+1}^{N-1}K_{ijk}\eta_i\eta_j^2\eta_k^2+\sum_{j=1}^{N-1}K_{ijN}\times\right.\\&\left.\eta_i\eta_j^2\eta_N^2\right)-2\rho_0\left(\sum_{j=1}^{N-3}\sum_{k=j+1}^{N-2}\sum_{l=k+1}^{N-1}K_{ijkl}\eta_i\eta_j^2\eta_k^2\eta_l^2+\sum_{j=1}^{N-2}\sum_{k=j+1}^{N-1}K_{ijkN}\eta_i\eta_j^2\eta_k^2\eta_N^2\right)\\&+\nabla_0\cdot\left(\tilde{\varphi}J\sum_{j=1,\neq i}^{N-1}\frac{\beta_{ij}}{4}\right.\\&\left.\boldsymbol{F}^{-1}\cdot(\nabla\eta_i-\nabla\eta_j)\right)+\nabla_0\cdot\left(\tilde{\varphi}J\frac{\beta_{iN}}{4}\boldsymbol{F}^{-1}\cdot\left(\nabla\eta_i+\sum_{j=1}^{N-1}\nabla\eta_j\right)\right)\qquad\text{for all } i=1,2,3,\ldots,N,\end{aligned}\tag{A.3}$$

respectively, and in Eqs. (A.2) and (A.3), $\eta_N=1-\sum_{m=1}^{N-1}\eta_m$; see Eq. (2.1). The derivatives with overbar, for example, $\overline{\frac{\partial\boldsymbol{F}_t}{\partial\eta_k}}$ in Eqs. (A.2) and (A.3) should be interpreted as follows: at first $\boldsymbol{F}_t(\eta_0,\ldots,\eta_{k-1},\eta_k,\eta_{k+1},\ldots,\eta_N)$ is differentiated with respect to η_k considering all the N order parameters $\eta_1,\ldots,\eta_{k-1},\eta_k,\eta_{k+1},\ldots,\eta_N$ to be mutually independent (see [45] for detailed derivation), and then η_N is substituted by $1-\sum_{j=1}^{N-1}\eta_j$ (see Eq. (2.1)). When $i=N$, Eq. (A.3) simplifies to

$$\begin{aligned}\overline{X}_N=&\left(\boldsymbol{P}_e^T\cdot\boldsymbol{F}-\bar{J}_t\psi_e\boldsymbol{I}\right):\overline{\boldsymbol{F}}_t^{-1}\cdot\overline{\frac{\partial\boldsymbol{F}_t}{\partial\eta_N}}-\overline{J}_t\overline{\frac{\partial\psi_e}{\partial\eta_N}}-2J\rho_0\tilde{A}\sum_{j=1}^{N-1}\eta_j^2\eta_N\varphi(a_b,\eta_0)\\&-2\rho_0\sum_{j=1}^{N-1}K_{Nj}(\eta_N+\eta_j-1)\times\\&(2\eta_N+\eta_j-1)\eta_j^2\eta_N-2\rho_0\left(\sum_{j=1}^{N-1}K_{0Nj}\eta_j^2+\sum_{j=1}^{N-2}\sum_{k=j+1}^{N-1}K_{0Njk}\eta_j^2\eta_k^2\right)\\&\times\eta_0^2\eta_N(1-\varphi(a_K,\eta_0))-2\rho_0\times\\&\sum_{j=1}^{N-2}\sum_{k=j+1}^{N-1}K_{Njk}\eta_k^2\eta_N\eta_j^2-2\rho_0\sum_{j=1}^{N-3}\sum_{k=j+1}^{N-2}\sum_{l=k+1}^{N-1}K_{Njkl}\eta_l^2\eta_N\eta_j^2\eta_k^2\end{aligned}$$

$$+\nabla_0\cdot\left(\tilde{\varphi}J\sum_{j=1}^{N-1}\frac{\beta_{Nj}}{4}\boldsymbol{F}^{-1}\cdot(\nabla\eta_N-\nabla\eta_j)\right), \tag{A.4}$$

where we have used Eq. (2.12) and $\beta_{NN}=0$.

Appendix B. Derivation of the weak forms of the governing equations and their linearizations

In Section 3 we have given an outline of the weak formulations for the equilibrium equations and the Ginzburg–Landau equations. In this appendix we provide the details of the derivations.

B.1. Derivation of the weak form of equilibrium equations and linearization

The weak form of the mechanical equilibrium equation (2.15) is given by Eq. (3.1). Considering the identity $\nabla_0\cdot(\boldsymbol{P}^T\cdot\delta\boldsymbol{u})=(\nabla_0\cdot\boldsymbol{P})\cdot\delta\boldsymbol{u}+\boldsymbol{P}^T:\nabla_0\delta\boldsymbol{u}$ and applying the Gauss divergence theorem, we rewrite Eq. (3.1) as

$$\mathscr{R}(\boldsymbol{u},\delta\boldsymbol{u})=\int_{\Omega_0}\boldsymbol{P}^T:\nabla_0\delta\boldsymbol{u}\,dV_0-\int_{S_{0T}}\boldsymbol{p}^{sp}\cdot\delta\boldsymbol{u}\,dA_0=\int_{\Omega_0}\boldsymbol{S}:\boldsymbol{F}^T\cdot\nabla\delta\boldsymbol{u}\cdot\boldsymbol{F}\,dV_0-\int_{S_{0T}}\boldsymbol{p}^{sp}\cdot\delta\boldsymbol{u}\,dA_0, \tag{B.1}$$

where the relation between the stresses $\boldsymbol{P}=\boldsymbol{F}\cdot\boldsymbol{S}$ and the relation $\nabla_0\delta\boldsymbol{u}=\nabla\delta\boldsymbol{u}\cdot\boldsymbol{F}$ have been used in the first integrand. Note that $\boldsymbol{p}:=\boldsymbol{P}\cdot\boldsymbol{n}_0$ is the traction in Ω_0, $\boldsymbol{p}^{sp}$ is the applied traction on the external boundary S_{0T}, and dA_0 is an area element on a surface in Ω_0. By using the relation between $\boldsymbol{S}$ and $\boldsymbol{\sigma}$ given by $\boldsymbol{F}\cdot\boldsymbol{S}\cdot\boldsymbol{F}^T=J\boldsymbol{\sigma}$ [57] we show that

$$\boldsymbol{S}:\boldsymbol{F}^T\cdot\nabla\delta\boldsymbol{u}\cdot\boldsymbol{F}=\boldsymbol{F}\cdot\boldsymbol{S}\cdot\boldsymbol{F}^T:sym(\nabla\delta\boldsymbol{u})=\boldsymbol{S}:\delta\boldsymbol{E}=\boldsymbol{\tau}:\delta\boldsymbol{\varepsilon}. \tag{B.2}$$

Using Eq. (B.2) in Eq. (B.1), the final expression for the weak form Eq. (3.2) is obtained.

We now linearize the weak form $\mathscr{R}(\boldsymbol{u},\delta\boldsymbol{u})$, given by Eq. (3.2), which we assume to be a differentiable functional of $\boldsymbol{u}$. Denoting the increment of the displacement field by $\Delta\boldsymbol{u}$, we express the weak form in Taylor's series about $\boldsymbol{u}$ (see e.g. Chapter 8 of [59])

$$\mathscr{R}(\boldsymbol{u}+\Delta\boldsymbol{u},\delta\boldsymbol{u})=\mathscr{R}(\boldsymbol{u},\delta\boldsymbol{u})+\Delta\mathscr{R}(\boldsymbol{u},\Delta\boldsymbol{u},\delta\boldsymbol{u})+o(\Delta\boldsymbol{u})=0, \tag{B.3}$$

where $\delta\boldsymbol{u}$ has been kept fixed, $o(\Delta\boldsymbol{u})$ is such that $\lim_{\Delta\boldsymbol{u}\to\boldsymbol{0}}o(\Delta\boldsymbol{u})/|\Delta\boldsymbol{u}|=0$, and $\Delta\mathscr{R}(\boldsymbol{u},\Delta\boldsymbol{u},\delta\boldsymbol{u})$ is the Gâteaux derivative (directional derivative) of $\mathscr{R}$, which is defined as (see e.g. [72])

$$\Delta\mathscr{F}(\boldsymbol{u},\Delta\boldsymbol{u},\delta\boldsymbol{u})=D\mathscr{F}(\boldsymbol{u},\delta\boldsymbol{u})\cdot\Delta\boldsymbol{u}=\frac{d}{d\epsilon}\mathscr{F}(\boldsymbol{u}+\epsilon\Delta\boldsymbol{u},\delta\boldsymbol{u})\bigg|_{\epsilon=0} \tag{B.4}$$

for any differentiable function or functional $\mathscr{F}$ (can be a scalar, vector, or a tensor). Assuming that the external loads are 'dead', i.e. $\boldsymbol{p}^{sp}$ is independent of $\boldsymbol{u}$, we linearize $\mathscr{R}$ in Eq. $(3.2)_1$ to obtain

$$D\mathscr{R}\cdot\Delta\boldsymbol{u}=\int_{\Omega_0}\Delta\boldsymbol{S}_e:\delta\boldsymbol{E}\,dV_0+\int_{\Omega_0}\Delta\boldsymbol{S}_{st}:\delta\boldsymbol{E}\,dV_0+\int_{\Omega_0}\boldsymbol{S}:\,\Delta(\delta\boldsymbol{E})\,dV_0, \tag{B.5}$$

where we have used the following decomposition of the second Piola–Kirchhoff stress $\boldsymbol{S}=\boldsymbol{S}_e+\boldsymbol{S}_{st}$, with $\boldsymbol{S}_e=J_t\boldsymbol{F}_t^{-1}\cdot\hat{\boldsymbol{S}}_e\cdot\boldsymbol{F}_t^{-T}$, and

$$\begin{aligned}\boldsymbol{S}_{st}=\;&J\rho_0(\breve{\psi}^{\theta}+\psi^{\nabla})\boldsymbol{C}^{-1}-J\beta_{0M}\boldsymbol{F}^{-1}\cdot\nabla\eta_0\otimes\boldsymbol{F}^{-1}\cdot\nabla\eta_0-J\tilde{\varphi}\sum_{i=1}^{N-1}\sum_{j=i+1}^{N}\frac{\beta_{ij}}{4}\big[\boldsymbol{F}^{-1}\cdot\nabla\eta_i\otimes\boldsymbol{F}^{-1}\cdot\nabla\eta_i+\\&\boldsymbol{F}^{-1}\cdot\nabla\eta_j\otimes\boldsymbol{F}^{-1}\cdot\nabla\eta_j-2\,sym(\boldsymbol{F}^{-1}\cdot\nabla\eta_i\otimes\boldsymbol{F}^{-1}\cdot\nabla\eta_j)\big],\end{aligned} \tag{B.6}$$

which were obtained using Eq. (2.16) and the relations between $\boldsymbol{P}$, $\boldsymbol{\sigma}$, and $\boldsymbol{S}$ [56]: $\boldsymbol{P}=\boldsymbol{F}\cdot\boldsymbol{S}$ and $\boldsymbol{P}=J\boldsymbol{\sigma}\cdot\boldsymbol{F}^{-T}$.

When the external load is a function of $\boldsymbol{u}$, its contribution on the right-hand side of Eq. (B.5) can be seen from e.g. [57]. We now derive an amenable form of Eq. (B.5) so that Newton's iterative method can be applied to obtain the increment of displacement $\Delta\boldsymbol{u}$. The derivations for all three integrands are shown in the following.

(i) First integral in Eq. (B.5)

Taking the increment of $\boldsymbol{S}_e=J_t\boldsymbol{F}_t^{-1}\cdot\hat{\boldsymbol{S}}_e\cdot\boldsymbol{F}_t^{-T}$ (can be obtained using $J\boldsymbol{\sigma}_e=\boldsymbol{F}\cdot\boldsymbol{S}_e\cdot\boldsymbol{F}^T$ and Eq. $(2.16)_2$) and recalling that $\boldsymbol{F}_t$ is independent of $\boldsymbol{u}$ (see Eqs. (2.4) and (2.6)), we obtain

$$\Delta\boldsymbol{S}_e=J_t\boldsymbol{F}_t^{-1}\cdot\Delta\hat{\boldsymbol{S}}_e\cdot\boldsymbol{F}_t^{-T}=J_t\boldsymbol{F}_t^{-1}\cdot(\hat{\boldsymbol{\mathcal{C}}}_e:\Delta\boldsymbol{E}_e)\cdot\boldsymbol{F}_t^{-T}, \tag{B.7}$$

where $\hat{\boldsymbol{\mathcal{C}}}_e$ is the fourth order elastic modulus tensor with respect to Ω_t given by Eq. (3.6). By using Eqs. (2.2) and $(2.3)_{1,2}$ one can easily show that $\Delta\boldsymbol{E}$ and $\Delta\boldsymbol{E}_e$ are related by

$$\Delta\boldsymbol{E}_e = 0.5\,\Delta(\boldsymbol{F}_e^T\cdot\boldsymbol{F}_e-\boldsymbol{I}) = 0.5\,\boldsymbol{F}_t^{-T}\cdot[\Delta\boldsymbol{F}^T\cdot\boldsymbol{F}+\boldsymbol{F}^T\cdot\Delta\boldsymbol{F}]\cdot\boldsymbol{F}_t^{-1} = \boldsymbol{F}_t^{-T}\cdot\Delta\boldsymbol{E}\cdot\boldsymbol{F}_t^{-1}, \tag{B.8}$$

which we use to rewrite Eq. (B.7) as

$$\Delta\boldsymbol{S}_e = J_t\boldsymbol{F}_t^{-1}\cdot(\hat{\boldsymbol{\mathcal{C}}}_e:\boldsymbol{F}_t^{-T}\cdot\Delta\boldsymbol{E}\cdot\boldsymbol{F}_t^{-1})\cdot\boldsymbol{F}_t^{-T}. \tag{B.9}$$

We can express Eq. (B.9) in the form

$$\Delta\boldsymbol{S}_e = \boldsymbol{\mathcal{C}}_e:\Delta\boldsymbol{E}, \tag{B.10}$$

where $\boldsymbol{\mathcal{C}}_e$ is the fourth order elasticity tensor defined in Ω_0, and it can be expressed in the indicial notations as

$$\mathcal{C}_{(e)ABCD} = J_t F^{-1}_{(t)A\hat{A}}F^{-1}_{(t)B\hat{B}}F^{-1}_{(t)C\hat{C}}F^{-1}_{(t)D\hat{D}}\hat{\mathcal{C}}_{(e)\hat{A}\hat{B}\hat{C}\hat{D}}, \tag{B.11}$$

where $\hat{\boldsymbol{\mathcal{C}}}_e$ was defined in Section 2; see Eq. (2.9); see Section 3.1 for the meaning of the indices. Note that we can express the incremental Lagrangian strains as (see Chapter 10 of [58]) $\Delta\boldsymbol{E} = \boldsymbol{F}^T\cdot\Delta\boldsymbol{\varepsilon}\cdot\boldsymbol{F}$, where $\Delta\boldsymbol{\varepsilon} := 0.5(\nabla\Delta\boldsymbol{u}+\nabla\Delta\boldsymbol{u}^T)$. Using Eq. (B.10) and the expressions for $\Delta\boldsymbol{E}$ and $\delta\boldsymbol{E}$ (see above and Section 3.1), we express the first integrand of Eq. (B.5) as

$$\Delta\boldsymbol{S}_e:\delta\boldsymbol{E} = \delta\boldsymbol{E}:\boldsymbol{\mathcal{C}}_e:\Delta\boldsymbol{E} = \boldsymbol{F}^T\cdot\delta\boldsymbol{\varepsilon}\cdot\boldsymbol{F}:(\boldsymbol{\mathcal{C}}_e:\boldsymbol{F}^T\cdot\Delta\boldsymbol{\varepsilon}\cdot\boldsymbol{F}) = \delta\boldsymbol{\varepsilon}:J\mathsf{C}_e:\Delta\boldsymbol{\varepsilon}, \tag{B.12}$$

where C_e is the elasticity tensor defined in the current configuration, which is related with $\boldsymbol{\mathcal{C}}_e$ and $\hat{\boldsymbol{\mathcal{C}}}_e$ by Eq. $(3.7)_1$. For obtaining Eq. $(3.7)_1$, we have used the following 'square tensor product' between two arbitrary second-order tensors $\boldsymbol{A}$ and $\boldsymbol{D}$ and its transpose given by (see e.g. Chapter 1 of [55]):

$$(\boldsymbol{A}\boxtimes\boldsymbol{D})_{abcd} = A_{ac}D_{bd} \qquad \text{and} \qquad (\boldsymbol{A}\boxtimes\boldsymbol{D})^T_{abcd} = (\boldsymbol{A}^T\boxtimes\boldsymbol{D}^T)_{abcd} = A_{ca}D_{db}. \tag{B.13}$$

We have also used

$$[(\boldsymbol{A}\boxtimes\boldsymbol{D}):\boldsymbol{\mathcal{B}}]_{abcd} = A_{af}D_{bg}\mathcal{B}_{fgcd} \quad \text{and} \quad [\boldsymbol{\mathcal{B}}:(\boldsymbol{A}\boxtimes\boldsymbol{D})^T]_{abcd} = \mathcal{B}_{abfg}A_{cf}D_{dg}, \tag{B.14}$$

which were obtained using Eq. (B.13) and the following product between two arbitrary fourth order tensors $\boldsymbol{\mathcal{A}}$ and $\boldsymbol{\mathcal{B}}$ given by $[\boldsymbol{\mathcal{A}}:\boldsymbol{\mathcal{B}}]_{abcd} = \mathcal{A}_{abfg}\mathcal{B}_{fgcd}$ [55].

(ii) Second integral in Eq. (B.5)

We now concentrate on the second integrand in Eq. (B.5). Our goal is to obtain the fourth-order tangent modulus tensor C_{st} due to structural stresses and express $\Delta\boldsymbol{S}_{st}:\delta\boldsymbol{E}$ in a form similar to Eq. (B.12). Analogous to the elasticity theory, we call the tensor C_{st} the fourth-order spatial *structural tensor*. The following linearizations will be used (see Chapter 8 of [56]):

$$\Delta J = J\nabla\cdot\Delta\boldsymbol{u} = J\,tr(\Delta\boldsymbol{\varepsilon}); \qquad \Delta\boldsymbol{F}^{-1} = -\boldsymbol{F}^{-1}\cdot\nabla\Delta\boldsymbol{u}. \tag{B.15}$$

Using Eq. $(B.15)_2$, one can easily prove the following identities

$$\Delta(\nabla\eta_k) = \Delta(\boldsymbol{F}^{-T}\cdot\nabla_0\eta_k) = \Delta\boldsymbol{F}^{-T}\cdot\nabla_0\eta_k = -(\nabla\Delta\boldsymbol{u})^T\cdot\boldsymbol{F}^{-T}\cdot\nabla_0\eta_k = -(\nabla\Delta\boldsymbol{u})^T\cdot\nabla\eta_k, \quad \text{and} \tag{B.16}$$

$$\Delta(|\nabla\eta_k|^2) = \Delta(|\boldsymbol{F}^{-T}\cdot\nabla_0\eta_k|^2) = -2\nabla\eta_k\cdot((\nabla\Delta\boldsymbol{u})^T\cdot\boldsymbol{F}^{-T}\cdot\nabla_0\eta_k) = -2\nabla\eta_k\cdot((\nabla\Delta\boldsymbol{u})^T\cdot\nabla\eta_k), \tag{B.17}$$

where we have used the fact that $\nabla_0\eta_k$ is independent of $\boldsymbol{u}$, i.e. $\Delta(\nabla_0\eta_k) = \boldsymbol{0}$. Taking an incremental derivative of $\boldsymbol{S}_{st} = J\boldsymbol{F}^{-1}\cdot\boldsymbol{\sigma}_{st}\cdot\boldsymbol{F}^{-T}$ and using Eqs. (B.15) to (B.17) we derive

$$\begin{aligned}\Delta\boldsymbol{S}_{st} &= (\Delta J)\boldsymbol{F}^{-1}\cdot\boldsymbol{\sigma}_{st}\cdot\boldsymbol{F}^{-T} + J\,\Delta\boldsymbol{F}^{-1}\cdot\boldsymbol{\sigma}_{st}\cdot\boldsymbol{F}^{-T} + J\boldsymbol{F}^{-1}\cdot\boldsymbol{\sigma}_{st}\cdot\Delta\boldsymbol{F}^{-T} + J\boldsymbol{F}^{-1}\cdot\Delta\boldsymbol{\sigma}_{st}\cdot\boldsymbol{F}^{-T}\\ &= J\boldsymbol{F}^{-1}\cdot\left[tr(\Delta\boldsymbol{\varepsilon})\,\boldsymbol{\sigma}_{st} - (\nabla\Delta\boldsymbol{u})\cdot\boldsymbol{\sigma}_{st} - \boldsymbol{\sigma}_{st}\cdot(\nabla\Delta\boldsymbol{u})^T + \Delta\boldsymbol{\sigma}_{st}\right]\cdot\boldsymbol{F}^{-T}.\end{aligned} \tag{B.18}$$

The inner product between the expressions for $\Delta\boldsymbol{S}_{st}$ given by Eqs. $(B.18)_2$ and $\delta\boldsymbol{E}$ (see Section 3.1) yields

$$\Delta\boldsymbol{S}_{st}:\delta\boldsymbol{E} = \Delta\boldsymbol{S}_{st}:\boldsymbol{F}^T\cdot\delta\boldsymbol{\varepsilon}\cdot\boldsymbol{F} = \boldsymbol{F}\cdot\Delta\boldsymbol{S}_{st}\cdot\boldsymbol{F}^T:\delta\boldsymbol{\varepsilon} = J[tr(\Delta\boldsymbol{\varepsilon})\boldsymbol{\sigma}_{st} - 2\nabla\Delta\boldsymbol{u}\cdot\boldsymbol{\sigma}_{st} + \Delta\boldsymbol{\sigma}_{st}]:\delta\boldsymbol{\varepsilon}, \tag{B.19}$$

where an amenable form of $\Delta\boldsymbol{\sigma}_{st}$ is yet to be determined. To this end, we take the increment of Eq. (2.18) to obtain

$$\Delta\boldsymbol{\sigma}_{st} = \rho_0\Delta\psi^{\nabla}\boldsymbol{I} - \Delta\Bigg[\beta_{0M}\nabla\eta_0\otimes\nabla\eta_0 + \tilde{\varphi}\sum_{i=1}^{N-1}\sum_{j=i+1}^{N}\frac{\beta_{ij}}{4}\left\{\nabla\eta_i\otimes\nabla\eta_i + \nabla\eta_j\otimes\nabla\eta_j - 2\,sym(\nabla\eta_i\otimes\nabla\eta_j)\right\}\Bigg], \tag{B.20}$$

where it should be noted that $\Delta\check{\psi}^{\theta} = 0$, as it is independent of $\boldsymbol{u}$ (see Eq. (2.10)). Note that $\rho_0\Delta\psi^{\nabla}$ appearing in Eq. (B.20) is expressed using Eqs. (2.13), (B.15)$_2$ to (B.17), and the expression for $\Delta\boldsymbol{\varepsilon}$ (see the paragraph after Eq. (B.11)) as

$$\begin{aligned}\rho_0\Delta\psi^{\nabla} &= -\beta_{0M}(\nabla\Delta\boldsymbol{u})^T : \nabla\eta_0\otimes\nabla\eta_0 - \frac{\tilde{\varphi}}{4}\sum_{i=1}^{N-1}\sum_{j=i+1}^{N}\beta_{ij}[\nabla\eta_i\cdot((\nabla\Delta\boldsymbol{u})^T\cdot\nabla\eta_i) + \nabla\eta_j\cdot((\nabla\Delta\boldsymbol{u})^T\cdot\nabla\eta_j) - \\ &\quad \nabla\eta_i\cdot(\nabla\Delta\boldsymbol{u} + (\nabla\Delta\boldsymbol{u})^T)\cdot\nabla\eta_j] \\ &= -\beta_{0M}\Delta\boldsymbol{\varepsilon} : \nabla\eta_0\otimes\nabla\eta_0 - \frac{\tilde{\varphi}}{4}\sum_{i=1}^{N-1}\sum_{j=i+1}^{N}\beta_{ij}\Delta\boldsymbol{\varepsilon} : \\ &\quad \left[\nabla\eta_i\otimes\nabla\eta_i + \nabla\eta_j\otimes\nabla\eta_j - 2sym(\nabla\eta_j\otimes\nabla\eta_i)\right],\end{aligned} \tag{B.21}$$

where we have used the following identity between an arbitrary second-order tensor $\boldsymbol{A}$ and a second-order symmetric tensor $\boldsymbol{D}$ [55], $\boldsymbol{A} : \boldsymbol{D} = sym(\boldsymbol{A}) : \boldsymbol{D}$. The other terms on the right-hand side of Eq. (B.20) can be rewritten using Eqs. (B.15)$_2$ as

$$\begin{aligned}&-\Delta\Bigg[\beta_{0M}\nabla\eta_0\otimes\nabla\eta_0 + \frac{\tilde{\varphi}}{4}\sum_{i=1}^{N-1}\sum_{j=i+1}^{N}\beta_{ij}\left(\nabla\eta_i\otimes\nabla\eta_i + \nabla\eta_j\otimes\nabla\eta_j - \nabla\eta_i\otimes\nabla\eta_j - \nabla\eta_j\otimes\nabla\eta_i\right)\Bigg] \\ &= \beta_{0M}[\nabla\eta_0\otimes(\nabla\Delta\boldsymbol{u})^T\cdot\nabla\eta_0 + (\nabla\Delta\boldsymbol{u})^T\cdot\nabla\eta_0\otimes\nabla\eta_0] + \frac{\tilde{\varphi}}{4}\sum_{i=1}^{N-1}\sum_{j=i+1}^{N}\beta_{ij}[(\nabla\Delta\boldsymbol{u})^T\cdot\nabla\eta_i\otimes\nabla\eta_i + \\ &\quad \nabla\eta_i\otimes(\nabla\Delta\boldsymbol{u})^T\cdot\nabla\eta_i + (\nabla\Delta\boldsymbol{u})^T\cdot\nabla\eta_j\otimes\nabla\eta_j + \nabla\eta_j\otimes(\nabla\Delta\boldsymbol{u})^T\cdot\nabla\eta_j - (\nabla\Delta\boldsymbol{u})^T\cdot\nabla\eta_i\otimes\nabla\eta_j - \\ &\quad \nabla\eta_i\otimes(\nabla\Delta\boldsymbol{u})^T\cdot\nabla\eta_j - (\nabla\Delta\boldsymbol{u})^T\cdot\nabla\eta_j\otimes\nabla\eta_i - \nabla\eta_j\otimes(\nabla\Delta\boldsymbol{u})^T\cdot\nabla\eta_i].\end{aligned} \tag{B.22}$$

Using Eqs. (B.21) and (B.22) in Eq. (B.20), we calculate the following inner product, which is the last term in Eq. (B.19)

$$\begin{aligned}&\Delta\boldsymbol{\sigma}_{st} : \delta\boldsymbol{\varepsilon} = -\Delta\boldsymbol{\varepsilon} : \Bigg[\beta_{0M}\nabla\eta_0\otimes\nabla\eta_0 \\ &+ \frac{\tilde{\varphi}}{4}\sum_{i=1}^{N-1}\sum_{j=i+1}^{N}\beta_{ij}\{\nabla\eta_i\otimes\nabla\eta_i + \nabla\eta_j\otimes\nabla\eta_j - 2sym(\nabla\eta_i\otimes\nabla\eta_j)\}\Bigg]\times \\ &tr(\delta\boldsymbol{\varepsilon}) + 2(\nabla\Delta\boldsymbol{u})^T\cdot\Bigg[\beta_{0M}\nabla\eta_0\otimes\nabla\eta_0 \\ &+ \frac{\tilde{\varphi}}{4}\sum_{i=1}^{N-1}\sum_{j=i+1}^{N}\beta_{ij}\{\nabla\eta_i\otimes\nabla\eta_i + \nabla\eta_j\otimes\nabla\eta_j - 2sym(\nabla\eta_i\otimes\nabla\eta_j)\}\Bigg] : \delta\boldsymbol{\varepsilon} \\ &= \left[\boldsymbol{\sigma}_{st} : \Delta\boldsymbol{\varepsilon} - \rho_0(\check{\psi}^{\theta} + \psi^{\nabla})\,tr(\Delta\boldsymbol{\varepsilon})\right]tr(\delta\boldsymbol{\varepsilon}) - 2(\nabla\Delta\boldsymbol{u})^T\cdot\left[\boldsymbol{\sigma}_{st} - \rho_0(\check{\psi}^{\theta} + \psi^{\nabla})\boldsymbol{I}\right] : \delta\boldsymbol{\varepsilon},\end{aligned} \tag{B.23}$$

where Eq. (B.23)$_2$ has been obtained from Eq. (B.23)$_1$ by eliminating the gradient of the order parameters using Eq. (2.18). Using Eq. (B.23) in Eq. (B.19) and then rearranging the terms we have the following expression for the

integrand

$$\Delta \boldsymbol{S}_{st} : \delta \boldsymbol{E} = J[tr(\Delta \boldsymbol{\varepsilon})\boldsymbol{\sigma}_{st} - 4\Delta \boldsymbol{\varepsilon} \cdot \boldsymbol{\sigma}_{st} + J\rho_0(\breve{\psi}^{\theta} + \psi^{\nabla})(2\Delta \boldsymbol{\varepsilon} - tr(\Delta \boldsymbol{\varepsilon})\boldsymbol{I}) + (\Delta \boldsymbol{\varepsilon} : \boldsymbol{\sigma}_{st})\boldsymbol{I}] : \delta \boldsymbol{\varepsilon}, \tag{B.24}$$

where we have used the relation between $\Delta \boldsymbol{E}$ and $\Delta \boldsymbol{\varepsilon}$ (see the text after Eq. (B.11)). We will use the 'square product' between two arbitrary second-order tensors $\boldsymbol{A}$ and $\boldsymbol{D}$ given by Eq. (B.13) and the following dyadic product given by (see e.g. Chapter 1 of [55]): $(\boldsymbol{A} \otimes \boldsymbol{D})_{abcd} = A_{ab}D_{cd}$. We will also use the fourth-order symmetrizer (see e.g. Chapter 1 of [55]) $\mathbb{S}_{abcd} = 0.5(\delta_{ac}\delta_{bd} + \delta_{ad}\delta_{bc})$, and the following identities $[(\boldsymbol{A} \boxtimes \boldsymbol{D}) : \mathbb{S}]_{abcd} = 0.5(A_{ac}D_{bd} + A_{ad}D_{bc})$, and $(\boldsymbol{A} \otimes \boldsymbol{D}) : \boldsymbol{G} = (\boldsymbol{D} : \boldsymbol{G}^T)\boldsymbol{A}$, where $\boldsymbol{G}$ is an arbitrary second order tensor (see Chapter 1 of [55]). Considering the definition of the tensor dyadic product and the symmetrizer in Eq. (B.24) and rearranging the terms, we finally express Eq. (B.24) as

$$\begin{aligned}
&\Delta \boldsymbol{S}_{st} : \delta \boldsymbol{E} = J[tr(\Delta \boldsymbol{\varepsilon})\boldsymbol{\sigma}_{st} - 4\Delta \boldsymbol{\varepsilon} \cdot \boldsymbol{\sigma}_{st} + J\rho_0(\breve{\psi}^{\theta} + \psi^{\nabla})(2\Delta \boldsymbol{\varepsilon} - tr(\Delta \boldsymbol{\varepsilon})\boldsymbol{I}) + (\Delta \boldsymbol{\varepsilon} : \boldsymbol{\sigma}_{st})\boldsymbol{I}] : \delta \boldsymbol{\varepsilon} \\
&= tr(\Delta \boldsymbol{\varepsilon})\boldsymbol{\tau}_{st} : \delta \boldsymbol{\varepsilon} - 2\delta \boldsymbol{\varepsilon} : [(\boldsymbol{\tau}_{st} \boxtimes \boldsymbol{I} + \boldsymbol{I} \boxtimes \boldsymbol{\tau}_{st}) : \mathbb{S}] : \Delta \boldsymbol{\varepsilon} \\
&\quad + \rho_0 J(\breve{\psi}^{\theta} + \psi^{\nabla})\,\delta \boldsymbol{\varepsilon} : (2\mathbb{S} - \boldsymbol{I} \otimes \boldsymbol{I}) : \Delta \boldsymbol{\varepsilon} + tr(\delta \boldsymbol{\varepsilon})\boldsymbol{\tau}_{st} : \Delta \boldsymbol{\varepsilon} \\
&= \delta \boldsymbol{\varepsilon} : J\mathsf{C}_{st} : \Delta \boldsymbol{\varepsilon},
\end{aligned} \tag{B.25}$$

where $\boldsymbol{\tau}_{st} = J\boldsymbol{\sigma}_{st}$ is the Kirchhoff structural stress tensor, and the structural tensor $J\mathsf{C}_{st}$ has the form given by Eq. $(3.5)_2$.

(iii) Third integrand in Eq. (B.5)

The third integrand of Eq. (B.5) can be expressed as (see [57] for the proof)

$$\boldsymbol{S} : \Delta(\delta \boldsymbol{E}) = \nabla \Delta \boldsymbol{u} \cdot \boldsymbol{\tau} : \nabla \delta \boldsymbol{u}^T, \tag{B.26}$$

which contributes to the total tangent stiffness matrix, called the geometric stiffness [57,58].

Substituting Eqs. (B.12), $(B.25)_3$, and (B.26) into the respective three integrands of Eq. (B.5), we obtain the final expression for the linearization of the weak form given by Eq. (3.3).

B.2. Weak form and its linearization for Ginzburg–Landau equations

In Section 3.2 we have given the final expressions for the weak forms for N independent Ginzburg–Landau equations given by Eq. (A.1). The derivation yields nontrivial expressions; hence, the details are discussed in this appendix.

Discretizing Eq. $(A.1)_1$ by using Eq. (3.8), the finite difference form of the equation is obtained as

$$c_1\eta_0^n - \Delta t^n L_{0M}\nabla_0 \cdot (J\beta_{M0}\boldsymbol{F}^{n-1} \cdot \nabla \eta_0^n) + \Delta t^n f_0^n + c_2\eta_0^{n-1} + c_3\eta_0^{n-2} = 0, \quad \text{where} \tag{B.27}$$

$$\begin{aligned}
f_0^n = L_{0M}\Bigg[&-\left(\boldsymbol{P}_e^{nT} \cdot \boldsymbol{F}^n - \bar{J}_t^n\psi_e^n\boldsymbol{I}\right) : \boldsymbol{W}_0 + \bar{J}_t^n\overline{\left.\frac{\partial \psi_e}{\partial \eta_0}\right|_{\boldsymbol{F}_e}} + \rho_0(6\eta_0^n - 6\eta_0^{n2})\Delta\psi^{\theta} \\
&+ J^n\rho_0\tilde{A}\left(\sum_{i=1}^{N-2}\sum_{j=i+1}^{N-1}\eta_i^{n2}\eta_j^{n2} + \right. \\
&\left.\eta_N^{n\,2}\sum_{i=1}^{N-1}\eta_i^{n2}\right)\frac{\partial \varphi(a_b, \eta_0^n)}{\partial \eta_0} + J^n\rho_0[A_{0M}(\theta) + (a_\theta - 3)\Delta\psi^{\theta}(\theta)](2\eta_0^n - 6\eta_0^{n2} + 4\eta_0^{n3}) \\
&+ \frac{J^n}{8}\frac{\partial \tilde{\varphi}(a_\beta, a_c, \eta_0^n)}{\partial \eta_0} \times \\
&\left(\sum_{i=1}^{N-2}\sum_{j=i+1}^{N-1}\beta_{ij}|\nabla\eta_i^n - \nabla\eta_j^n|^2 + \sum_{i=1}^{N-1}\beta_{iN}|\nabla\eta_i^n - \nabla\eta_N^n|^2\right) \\
&+ \rho_0\left(\sum_{i=1}^{N-2}\sum_{j=i+1}^{N-1}K_{0ij}\eta_i^{n2}\eta_j^{n2} + \sum_{i=1}^{N-1}K_{0iN}\eta_i^{n2}\eta_N^{n\,2} + \right.
\end{aligned}$$

$$\sum_{i=1}^{N-3}\sum_{j=i+1}^{N-2}\sum_{k=j+1}^{N-1} K_{0ijk}\eta_i^{n\,2}\eta_j^{n\,2}\eta_k^{n\,2}+\sum_{i=1}^{N-2}\sum_{j=i+1}^{N-1} K_{0ijN}\eta_i^{n\,2}\eta_j^{n\,2}\eta_N^{n\,2}\Bigg)$$
$$\times\left(2(1-\varphi(a_K,\eta_0^n))\eta_0^n-\frac{\partial\varphi(a_K,\eta_0^n)}{\partial\eta_0}\eta_0^{n\,2}\right)\Bigg], \tag{B.28}$$

and $\boldsymbol{W}_k^n=\overline{\boldsymbol{F}_t^n}^{-1}\cdot\overline{\frac{\partial\boldsymbol{F}_t^n}{\partial\eta_k^n}}$ for all $k=0,1,\ldots,N$.

We will now discretize the other $N-1$ independent Ginzburg–Landau equations related to the variants from Eq. (A.1)$_2$. To this end, we define

$$\overline{X}_{im}:=\overline{X}_i-\overline{X}_m=\overline{X}_{im}^{loc}+\overline{X}_{im}^{\nabla}\quad\text{for } i,m=1,2,\ldots,N, \tag{B.29}$$

where $\overline{X}_i$ was defined in Eqs. (A.3) when $i\neq N$ and in Eq. (A.4) when $i=N$. $\overline{X}_{im}^{loc}$ consists of the local terms (independent of the gradient/Laplacian terms) which do not contribute to the Laplace matrix of the final algebraic FE equation, and $\overline{X}_{im}^{\nabla}$ is the nonlocal term (depending on the gradient/Laplacian terms) which contributes to the Laplace matrix (see Appendix B.2). The explicit forms of $\overline{X}_{im}^{loc}$ and $\overline{X}_{im}^{\nabla}$ are obtained by using Eq. (A.3) in Eq. (B.29) as

$$\overline{X}_{im}^{loc}=(\boldsymbol{P}_e^{n\,T}\cdot\boldsymbol{F}^n-\bar{J}_t^n\psi_e^n\boldsymbol{I}):(\boldsymbol{W}_i^n-\boldsymbol{W}_m^n)-\bar{J}_t^n\left(\overline{\left.\frac{\partial\psi_e}{\partial\eta_i}\right|_{\boldsymbol{F}_e}}-\overline{\left.\frac{\partial\psi_e^n}{\partial\eta_m}\right|_{\boldsymbol{F}_e}}\right)-2J^n\rho_0\tilde{A}\Bigg(\sum_{j=1,\neq i}^{N-1}\eta_j^{n\,2}\eta_i^n+\eta_N^{n\,2}\eta_i^n-$$
$$\sum_{j=1,\neq m,i}^{N-1}\eta_j^{n\,2}\eta_m^n-\eta_i^{n\,2}\eta_m^n-\eta_N^{n\,2}\eta_m^n\Bigg)\varphi(a_b,\eta_0^n)-2\rho_0\Bigg[\sum_{j=1,\neq i}^{N-1}K_{ij}(\eta_i^n+\eta_j^n-1)(2\eta_i^n+\eta_j^n-1)\eta_i^n\eta_j^{n\,2}-$$
$$\sum_{j=1,\neq m,i}^{N-1}K_{mj}(\eta_m^n+\eta_j^n-1)(2\eta_m^n+\eta_j^n-1)\eta_m^n\eta_j^{n\,2}$$
$$-K_{mi}(\eta_m^n+\eta_i^n-1)(2\eta_m^n+\eta_i^n-1)\eta_m^n\eta_i^{n\,2}\Bigg]-2\rho_0[K_{iN}\times$$
$$(\eta_i^n+\eta_N^n-1)(2\eta_i^n+\eta_N^n-1)\eta_i^n-K_{mN}(\eta_m^n+\eta_N^n-1)(2\eta_m^n+\eta_N^n-1)\eta_m^n]\eta_N^{n\,2}$$
$$-2\rho_0\Bigg[\sum_{j=1,\neq i}^{N-1}K_{0ij}\eta_i^n\eta_j^{n\,2}-$$
$$\sum_{j=1,\neq i}^{N-1}K_{0mj}\eta_m^n\eta_j^{n\,2}-K_{0mi}\eta_m^n\eta_i^{n\,2}+(K_{0iN}\eta_i^n-K_{0mN}\eta_m^n)\eta_N^{n\,2}$$
$$+\sum_{j=1,\neq i}^{N-2}\sum_{k=j+1,\neq i}^{N-1}(K_{0ijk}\eta_i^n-K_{0mjk}\eta_m^n)\eta_j^{n\,2}\times$$
$$\eta_k^{n\,2}-\sum_{j=1}^{N-1}K_{0mij}\eta_m^n\eta_j^{n\,2}\eta_i^{n\,2}+\sum_{j=1,\neq i}^{N-1}(K_{0ijN}\eta_i^n-K_{0mjN}\eta_m^n)\eta_j^{n\,2}\eta_N^{n\,2}-K_{0miN}\eta_m^n\eta_i^{n\,2}\eta_N^{n\,2}\Bigg]\eta_0^{n\,2}\times$$
$$(1-\varphi(a_K,\eta_0^n))-2\rho_0\Bigg[\sum_{j=1,\neq i}^{N-2}\sum_{k=j+1,\neq i}^{N-1}(K_{ijk}\eta_i^n-K_{mjk}\eta_m^n)\eta_j^{n\,2}\eta_k^{n\,2}-\sum_{j=1}^{N-1}K_{mij}\eta_m^n\eta_i^{n\,2}\eta_j^{n\,2}$$
$$+\sum_{j=1,\neq i}^{N-1}(K_{ijN}\eta_i^n-$$
$$K_{mjN}\eta_m^n)\eta_N^{n\,2}\eta_j^{n\,2}-K_{miN}\eta_m^n\eta_N^{n\,2}\eta_i^{n\,2}\Bigg]-2\rho_0\Bigg[\sum_{j=1,\neq i}^{N-3}\sum_{k=j+1,\neq i}^{N-2}\sum_{l=k+1,\neq i}^{N-1}(K_{ijkl}\eta_i^n-K_{mjkl}\eta_m^n)\eta_j^{n\,2}\eta_k^{n\,2}\eta_l^{n\,2}-$$

$$\sum_{k=1}^{N-2}\sum_{l=k+1}^{N-1} K_{mikl}\eta_m^n\eta_i^{n2}\eta_k^{n2}\eta_l^{n2} + \sum_{j=1,\neq i}^{N-2}\sum_{k=j+1,\neq i}^{N-1}(K_{ijkN}\eta_i^n - K_{mjkN}\eta_m^n)\eta_j^{n2}\eta_k^{n2}\eta_N^{n\,2} - \sum_{k=1}^{N-1} K_{mikN}\eta_m^n\eta_i^{n2} \times$$
$$\eta_k^{n2}\eta_N^{n\,2}\Bigg] \qquad \text{for all } i,m = 1,2,\ldots,N; \tag{B.30}$$

$$\bar{X}_{im}^{\nabla} = \nabla_0\cdot\Bigg[\frac{\tilde{\varphi}}{4}J^n\boldsymbol{F}^{n-1}\cdot\Bigg\{\sum_{j=1,\neq i}^{N-1}\beta_{ij}(\nabla\eta_i^n - \nabla\eta_j^n) - \sum_{j=1,\neq m}^{N-1}\beta_{mj}(\nabla\eta_m^n - \nabla\eta_j^n)$$
$$+\beta_{iN}\left(2\nabla\eta_i^n + \sum_{j=1,\neq i}^{N-1}\nabla\eta_j^n\right) -$$
$$\beta_{mN}\left(\nabla\eta_m^n + \nabla\eta_i^n + \sum_{j=1,\neq i}^{N-1}\nabla\eta_j^n\right)\Bigg\}\Bigg] \qquad \text{for all } i,m = 1,2,\ldots,N. \tag{B.31}$$

Furthermore, because we consider a non-monolithic scheme to solve all the Ginzburg–Landau equations, the Laplacian of η_i should eventually be the only contributor to the Laplace matrix corresponding to the algebraic FE equation for η_i. Thus, we further decouple the nonlocal term $\bar{X}_{im}^{\nabla}(\nabla\eta_k^n, \nabla^2\eta_k^n)$ (for all $k = 0,1,\ldots,i-1,i,i+1,\ldots,N-1$) into $\bar{X}_{im}^{\nabla(2)}(\nabla\eta_i^n, \nabla^2\eta_i^n)$ and $\bar{X}_{im}^{\nabla(1)}(\nabla\eta_k^n, \nabla^2\eta_k^n)$ (for all $k = 0,1,\ldots,i-1,i+1,\ldots,N-1$):

$$\bar{X}_{im}^{\nabla} = \bar{X}_{im}^{\nabla(1)} + \bar{X}_{im}^{\nabla(2)} \quad \text{for all } i,m = 1,2,\ldots,N, \quad \text{where} \tag{B.32}$$

$$\bar{X}_{im}^{\nabla(1)} = \nabla_0\cdot\Bigg[\frac{\tilde{\varphi}}{4}J^n\boldsymbol{F}^{n-1}\cdot\Bigg(\beta_{iN}\sum_{j=1,\neq i}^{N-1}\nabla\eta_j^n - \sum_{j=1,\neq i}^{N-1}\beta_{ij}\nabla\eta_j^n - \sum_{j=1,\neq m}^{N-1}\beta_{mj}\nabla\eta_m^n + \sum_{j=1,\neq m,i}^{N-1}\beta_{mj}\nabla\eta_j^n -$$
$$\beta_{mN}\nabla\eta_m^n - \beta_{mN}\sum_{j=1,\neq i}^{N-1}\nabla\eta_j^n\Bigg)\Bigg], \quad \text{when } i,m = 1,\ldots,N-1 \text{ and} \tag{B.33}$$

$$\bar{X}_{im}^{\nabla(2)} = \nabla_0\cdot\left[\frac{\tilde{\varphi}}{4}J^n\bar{\beta}_{im}\boldsymbol{F}^{n-1}\cdot\nabla\eta_i^n\right] \quad \text{with } \bar{\beta}_{im} = \sum_{j=1,\neq i}^{N-1}\beta_{ij} + \beta_{mi} + 2\beta_{iN} - \beta_{mN}$$
$$\text{when } i,m = 1,\ldots,N-1. \tag{B.34}$$

The decoupling in Eq. (B.32) allows us to express the weak form in a convenient form (see Appendix B.2). Obviously, when $m = N$, Eqs. (B.30) and (B.31) reduce to

$$\bar{X}_{iN}^{loc} = (\boldsymbol{P}_e^{n\,T}\cdot\boldsymbol{F}^n - \bar{J}_t^n\psi_e^n\boldsymbol{I}) : (\boldsymbol{W}_i^n - \boldsymbol{W}_N^n) - \bar{J}_t\left(\overline{\left.\frac{\partial\psi_e^n}{\partial\eta_i}\right|_{\boldsymbol{F}_e}} - \overline{\left.\frac{\partial\psi_e^n}{\partial\eta_N}\right|_{\boldsymbol{F}_e}}\right)$$
$$-2J\rho_0\tilde{A}\left(\sum_{j=1,\neq i}^{N-1}\eta_j^{n2}\eta_i^n + \eta_N^{n\,2}\eta_i^n -\right.$$
$$\left.\sum_{j=1}^{N-1}\eta_j^{n2}\eta_N^n\right)\varphi(a_b,\eta_0^n) - 2\rho_0\Bigg[\sum_{j=1,\neq i}^{N-1}K_{ij}(\eta_i^n + \eta_j^n - 1)(2\eta_i^n + \eta_j^n - 1)\eta_i^n\eta_j^{n2}$$
$$-\sum_{j=1}^{N-1}K_{Nj}(\eta_N^n + \eta_j^n - 1)\times$$
$$(2\eta_N^n + \eta_j^n - 1)\eta_N^n\eta_j^{n2}\Bigg] - 2\rho_0 K_{iN}(\eta_i^n + \eta_N^n - 1)(2\eta_i^n + \eta_N^n - 1)\eta_i^n\eta_N^{n\,2}$$

$$
\begin{aligned}
&- 2\rho_0 \left[\sum_{j=1}^{N-1} (K_{0ij}\eta_i^n - K_{0Nj}\eta_N^n)\eta_j^{n2} + \right. \\
&\left. K_{0iN}\eta_i^n \eta_N^{n\,2} + \sum_{j=1}^{N-2}\sum_{k=j+1}^{N-1} (K_{0ijk}\eta_i^n - K_{0Njk}\eta_N^n)\eta_j^{n2}\eta_k^{n2} + \sum_{j=1}^{N-1} K_{0ijN}\eta_i^n \eta_j^{n2}\eta_N^{n\,2} \right] \\
&\times \eta_0^2(1-\varphi(a_K,\eta_0)) - 2\rho_0 \times \\
&\left[\sum_{j=1}^{N-2}\sum_{k=j+1}^{N-1} (K_{ijk}\eta_i^n - K_{Njk}\eta_N^n)\eta_j^{n2}\eta_k^{n2} + \sum_{j=1}^{N-1} K_{ijN}\eta_i^n \eta_j^{n2}\eta_N^{n\,2} \right] - 2\rho_0 \left[\sum_{j=1}^{N-3}\sum_{k=j+1}^{N-2}\sum_{l=k+1}^{N-1} (K_{ijkl}\eta_i^n - \right. \\
&\left. K_{Njkl}\eta_N^n)\eta_j^{n2}\eta_k^{n2}\eta_l^{n2} + \sum_{j=1}^{N-2}\sum_{k=j+1}^{N-1} K_{ijkN}\eta_j^{n2}\eta_k^{n2}\eta_i^n \eta_N^{n\,2} \right] \qquad \text{for all } i = 1, 2, \ldots, N, \quad \text{and} \qquad \text{(B.35)}
\end{aligned}
$$

$$
\begin{aligned}
\bar{X}_{iN}^{\nabla} = \nabla_0 \cdot \Bigg[\frac{\tilde{\varphi}}{4} J^n \boldsymbol{F}^{n-1} \cdot \Bigg(&\sum_{j=1,\neq i}^{N-1} \beta_{ij}(\nabla\eta_i^n - \nabla\eta_j^n) \\
&- \sum_{j=1,\neq N}^{N-1} \beta_{Nj}(\nabla\eta_N^n - \nabla\eta_j^n) + \beta_{iN}\Big(2\nabla\eta_i^n + \sum_{j=1,\neq i}^{N-1} \nabla\eta_j^n\Big)\Bigg)\Bigg] \\
&\text{for all } i = 1, 2, \ldots, N, \qquad \text{(B.36)}
\end{aligned}
$$

respectively, and Eqs. (B.33) and (B.34) reduce to

$$
\begin{aligned}
\bar{X}_{iN}^{\nabla(1)} = \nabla_0 \cdot \Bigg[\frac{\tilde{\varphi}}{4} J^n \boldsymbol{F}^{n-1} \cdot \Bigg(&\beta_{iN} \sum_{j=1,\neq i}^{N-1} \nabla\eta_j^n - \sum_{j=1,\neq i}^{N-1} \beta_{ij}\nabla\eta_j^n + \sum_{j=1,\neq N,i}^{N-1} \beta_{Nj}\nabla\eta_j^n + \Bigg(\sum_{j=1,\neq N}^{N-1} \beta_{Nj} \Bigg) \\
&\Bigg(\sum_{j=1,\neq i}^{N-1} \nabla\eta_j^n \Bigg) \Bigg) \Bigg], \quad \text{and} \qquad \text{(B.37)}
\end{aligned}
$$

$$
\bar{X}_{iN}^{\nabla(2)} = \nabla_0 \cdot \left[\frac{\tilde{\varphi}}{4} J^n \bar{\beta}_{iN} \boldsymbol{F}^{n-1} \cdot \nabla\eta_i^n \right], \quad \text{where } \bar{\beta}_{iN} = \sum_{j=1,\neq i}^{N-1} (\beta_{ij} + \beta_{Nj}) + 4\beta_{iN}. \qquad \text{(B.38)}
$$

By using Eqs. (B.29) through (B.38) in the Ginzburg–Landau equation (A.1)$_2$ and discretizing it by using Eq. (3.8), we rewrite it as

$$
c_1\eta_i^n - \Delta t^n \sum_{m=1,\neq i}^{N} \frac{L_{im}}{4} \nabla_0 \cdot \left(J^n \tilde{\varphi}^n \bar{\beta}_{im} \boldsymbol{F}^{n-1} \cdot \nabla\eta_i^n \right) + \Delta t^n f_i^n + c_2\eta_i^{n-1} + c_3\eta_i^{n-2} = 0, \quad \text{where} \qquad \text{(B.39)}
$$

$$
\begin{aligned}
f_i^n(\eta_j^n, \nabla\eta_k^n, \nabla^2\eta_k^n) = - \sum_{m=1,\neq i}^{N} L_{im} \left(\bar{X}_{im}^{loc} + \bar{X}_{im}^{\nabla(1)} \right) \quad &\text{for all } j = 0, 1, \ldots, N-1; \\
k = 0, 1, \ldots, i-1, i+1, \ldots, N-1. \qquad &\text{(B.40)}
\end{aligned}
$$

By multiplying Eqs. (B.27) and (B.39) by the weighted function for the order parameter $\delta\eta_k^n$ and then integrating them over the entire domain and applying the Gauss divergence theorem, we have the weak forms corresponding to N independent Ginzburg–Landau equations given by Eq. (3.9) in Section 3.2. The linearization of the weak form is obtained in Eq. (3.11), where the derivatives $\partial f_k^n / \partial \eta_k^n \big|_{\boldsymbol{F}}$ for $k = 0, 1, \ldots, N$ are calculated using Eqs. (B.28) and (B.40):

$$
\begin{aligned}
\left. \frac{\partial f_0^n}{\partial \eta_0^n} \right|_{\boldsymbol{F}} = L_{0M} \Bigg[&- \left(\boldsymbol{P}_e^{n\,T} \cdot \boldsymbol{F}^n - \bar{J}_t^n \overline{\psi}_e^n \boldsymbol{I} \right) : \left\{ \overline{\boldsymbol{F}}_t^{n-1} \cdot \frac{\partial^2 \overline{\boldsymbol{F}}_t^n}{\partial \eta_0^{n2}} - \boldsymbol{W}_0^{n2} \right\} \\
&- \left. \frac{\partial \boldsymbol{P}_e^{n\,T}}{\partial \eta_0^n} \right|_{\boldsymbol{F}} \cdot \boldsymbol{F}^n : \boldsymbol{W}_0^n + \bar{J}_t^n \overline{\psi}_e^n \, tr(\boldsymbol{W}_0^{n2}) +
\end{aligned}
$$

$$\bar{J}_t^n \left(\frac{\partial \overline{\psi}_e^n}{\partial \eta_0^n}\bigg|_{\boldsymbol{F}} + \frac{\partial \overline{\psi}_e^n}{\partial \eta_0^n}\bigg|_{\boldsymbol{F}_e} \right) tr\boldsymbol{W}_0^n + \bar{J}_t^n \frac{\partial}{\partial \eta_0^n} \left(\frac{\partial \overline{\psi}_e^n}{\partial \eta_0^n}\bigg|_{\boldsymbol{F}_e} \right)_{\boldsymbol{F}}$$
$$+ \rho_0(6 - 12\eta_0^n)\Delta\psi^\theta + J^n\rho_0\tilde{A} \left(\sum_{i=1}^{N-2} \sum_{j=i+1}^{N-1} {\eta_i^n}^2 \times \right.$$
$$\left. {\eta_j^n}^2 + \sum_{i=1}^{N-1} {\eta_i^n}^2 {\eta_N^n}^2 \right) \frac{\partial^2 \varphi(a_b, \eta_0^n)}{\partial {\eta_0^n}^2} + J^n\rho_0[A_{0M}(\theta) + (a_\theta - 3)\Delta\psi^\theta(\theta)]$$
$$(2 - 12\eta_0^n + 12{\eta_0^n}^2) + \frac{J^n}{8} \times$$
$$\frac{\partial^2 \tilde{\varphi}(a_\beta, a_c, \eta_0^n)}{\partial {\eta_0^n}^2} \left(\sum_{i=1}^{N-2} \sum_{j=i+1}^{N-1} \beta_{ij} |\nabla\eta_i^n - \nabla\eta_j^n|^2 + \sum_{i=1}^{N-1} \beta_{iN} \left| \nabla\eta_i^n + \sum_{j=1}^{N-1} \eta_j^n \right|^2 \right)$$
$$+ \rho_0 \left\{ \sum_{i=1}^{N-2} \sum_{j=i+1}^{N-1} K_{0ij} {\eta_i^n}^2 \times \right.$$
$$\left. {\eta_j^n}^2 + \sum_{i=1}^{N-1} K_{0iN} {\eta_i^n}^2 {\eta_N^n}^2 + \sum_{i=1}^{N-3} \sum_{j=i+1}^{N-2} \sum_{k=j+1}^{N-1} K_{0ijk} {\eta_i^n}^2 {\eta_j^n}^2 {\eta_k^n}^2 + \sum_{i=1}^{N-2} \sum_{j=i+1}^{N-1} K_{0ijN} {\eta_i^n}^2 {\eta_j^n}^2 {\eta_N^n}^2 \right\} \times$$
$$\left\{ 2(1 - \varphi(a_K, \eta_0^n)) - 4\frac{\partial \varphi(a_K, \eta_0^n)}{\partial \eta_0} \eta_0^n - \frac{\partial^2 \varphi(a_K, \eta_0^n)}{\partial {\eta_0^n}^2} {\eta_0^n}^2 \right\} \Bigg], \quad \text{and} \tag{B.41}$$

$$\frac{\partial f_i}{\partial \eta_i^n}(\eta_0^n, \eta_1^n, \ldots, \eta_{N-1}^n)\bigg|_{\boldsymbol{F}} = -\sum_{m=1,\neq i}^{N} L_{im} \frac{\partial \bar{X}_{im}^{loc}}{\partial \eta_i^n}\bigg|_{\boldsymbol{F}}, \quad \text{where} \tag{B.42}$$

$$\frac{\partial \overline{X}_{im}^{loc}}{\partial \eta_i^n}\bigg|_{\boldsymbol{F}} = (\boldsymbol{P}_e^{nT} \cdot \boldsymbol{F}^n - \overline{J}_t^n \overline{\psi}_e^n \boldsymbol{I}) : \overline{\boldsymbol{F}}_t^{n-1}$$
$$\cdot \left[\frac{\partial}{\partial \eta_i^n} \left(\overline{\frac{\partial \boldsymbol{F}_t^n}{\partial \eta_i}} - \overline{\frac{\partial \boldsymbol{F}_t{}^n}{\partial \eta_m}} \right) - \frac{\partial \overline{\boldsymbol{F}}_t^n}{\partial \eta_i^n} \cdot (\boldsymbol{W}_i^n - \boldsymbol{W}_m^n) \right] + \frac{\partial \boldsymbol{P}_e^{nT}}{\partial \eta_i^n}\bigg|_{\boldsymbol{F}} \cdot \boldsymbol{F}^n :$$
$$(\boldsymbol{W}_i^n - \boldsymbol{W}_m^n) - \overline{J}_t^n \left[\overline{\psi}_e^n tr \left\{ \overline{\boldsymbol{F}}_t^{n-1} \cdot \frac{\partial \overline{\boldsymbol{F}}_t^n}{\partial \eta_i^n} \right\} + \frac{\partial \overline{\psi}_e^n}{\partial \eta_i^n}\bigg|_{\boldsymbol{F}} \right] tr(\boldsymbol{W}_i^n - \boldsymbol{W}_m^n)$$
$$- \overline{J}_t^n \left(\overline{\frac{\partial \psi_e^n}{\partial \eta_i^n}\bigg|_{\boldsymbol{F}_e}} - \overline{\frac{\partial \psi_e^n}{\partial \eta_m^n}\bigg|_{\boldsymbol{F}_e}} \right) \times$$
$$tr \left\{ \overline{\boldsymbol{F}}_t^{n-1} \cdot \frac{\partial \overline{\boldsymbol{F}}_t^n}{\partial \eta_i^n} \right\} - \overline{J}_t^n \frac{\partial}{\partial \eta_i^n} \left(\overline{\frac{\partial \psi^e}{\partial \eta_i^n}\bigg|_{\boldsymbol{F}_e}} - \overline{\frac{\partial \psi^e}{\partial \eta_m^n}\bigg|_{\boldsymbol{F}_e}} \right)$$
$$- 2J^n\rho_0\tilde{A} \left(\sum_{j=1,\neq i}^{N-1} {\eta_j^n}^2 + {\eta_N^n}^2 - 2\eta_i^n\eta_m^n - 2\eta_N^n \times \right.$$
$$\left. (\eta_i^n - \eta_m^n) \right) \varphi(a_b, \eta_0^n) - 2\rho_0 \left[\sum_{j=1,\neq i}^{N-1} K_{ij}(6{\eta_i^n}^2 + {\eta_j^n}^2 \right.$$
$$+ 6\eta_i^n\eta_j^n - 6\eta_i^n - 2\eta_j^n + 1){\eta_j^n}^2 - K_{im}(4{\eta_i^n}^2 +$$
$$4{\eta_m^n}^2 + 9\eta_i^n\eta_m^n - 6\eta_i^n - 6\eta_m^n + 2)\eta_i^n\eta_m^n + K_{iN}(\eta_i^n + \eta_N^n - 1)$$
$$\times \{{\eta_N^n}^2 - 4{\eta_i^n}^2 + \eta_i^n\eta_N^n + 2\eta_i^n - \eta_N^n\}\eta_N^n -$$

$$K_{mN}\{4{\eta_N^n}^2+4{\eta_m^n}^2+9\eta_m^n\eta_N^n-6\eta_N^n-6\eta_m^n+2\}\eta_m^n\eta_N^n\Big]$$
$$-2\rho_0\Bigg[\sum_{j=1,\neq i}^{N-1}K_{0ij}{\eta_j^n}^2-2K_{0mi}\eta_m^n\eta_i^n+$$
$$K_{0iN}({\eta_N^n}^2-2\eta_i^n\eta_N^n)+2K_{0mN}\eta_m^n\eta_N^n+\sum_{j=1}^{N-2}\sum_{k=j+1}^{N-1}K_{0ijk}{\eta_j^n}^2{\eta_k^n}^2-\sum_{j=1}^{N-1}2K_{0mji}\eta_i^n\eta_m^n{\eta_j^n}^2$$
$$+\sum_{j=1}^{N-1}K_{0ijN}{\eta_j^n}^2({\eta_N^n}^2-2\eta_i^n\eta_N^n)-2K_{0miN}(\eta_N^n-\eta_i^n)\eta_m^n\eta_i^n\eta_N^n\Bigg]{\eta_0^n}^2(1-\varphi(a_K,\eta_0^n))-$$
$$2\rho_0\Bigg[\sum_{j=1}^{N-2}\sum_{k=j+1}^{N-1}K_{ijk}{\eta_j^n}^2{\eta_k^n}^2-\sum_{j=1}^{N-1}2K_{mji}\eta_i^n\eta_m^n{\eta_j^n}^2+\sum_{j=1}^{N-1}K_{ijN}{\eta_j^n}^2({\eta_N^n}^2-2\eta_i^n\eta_N^n)+$$
$$\sum_{j=1,\neq i}^{N-1}2K_{mjN}\eta_m^n\eta_N^n{\eta_j^n}^2-2K_{miN}(\eta_N^n-\eta_i^n)\eta_i^n\eta_m^n\eta_N^n\Bigg]$$
$$-2\rho_0\Bigg[\sum_{j=1}^{N-3}\sum_{k=j+1}^{N-2}\sum_{l=k+1}^{N-1}K_{ijkl}{\eta_j^n}^2{\eta_k^n}^2{\eta_l^n}^2-$$
$$\sum_{k=1}^{N-2}\sum_{l=k+1}^{N-1}2K_{mikl}\eta_m^n\eta_i^n{\eta_k^n}^2{\eta_l^n}^2+\sum_{j=1}^{N-2}\sum_{k=j+1}^{N-1}\{K_{ijkN}({\eta_N^n}^2-2\eta_i^n\eta_N^n)+2K_{mjkN}\eta_m^n\eta_N^n\}{\eta_j^n}^2{\eta_k^n}^2-$$
$$\sum_{j=1}^{N-1}2K_{mjiN}(\eta_N^n-\eta_i^n)\eta_i^n\eta_m^n{\eta_j^n}^2\eta_N^n\Bigg]\quad\text{when } i,m=1,\ldots,N-1. \tag{B.43}$$

The expressions for $\frac{\partial X_{iN}^{loc}}{\partial\eta_i^n}$ can be obtained in a similar manner using Eq. (B.35). The meaning of the overline is described in Section 2. The explicit forms of some of the terms in Eq. (B.43) are

$$\left.\frac{\partial {\boldsymbol{P}_e^n}^T}{\partial\eta_i^n}\right|_{\boldsymbol{F}}\cdot\boldsymbol{F}^n=\Bigg[\overline{J}_t^n tr\left(\overline{\boldsymbol{F}}_t^{n-1}\cdot\frac{\partial\overline{\boldsymbol{F}}_t^n}{\partial\eta_i^n}\right)\overline{\boldsymbol{F}}_t^{n-1}\cdot\hat{\boldsymbol{S}}_e^n\cdot\overline{\boldsymbol{F}}_t^{n-T}$$
$$-2\,sym(\boldsymbol{Z}_i^n)+\overline{J}_t^n\overline{\boldsymbol{F}}_t^{n-1}\cdot\left.\frac{\partial\overline{\hat{\boldsymbol{S}}_e^n}}{\partial\eta_i^n}\right|_{\boldsymbol{F}}\cdot\overline{\boldsymbol{F}}_t^{n-T}\Bigg]\cdot\boldsymbol{C}^n; \tag{B.44}$$

$$\boldsymbol{Z}_i^n=\boldsymbol{S}_e^n\cdot\frac{\partial{\overline{\boldsymbol{F}}_t^n}^T}{\partial\eta_i^n}\cdot\overline{\boldsymbol{F}}_t^{n-T};\qquad\left.\frac{\partial\overline{\hat{\boldsymbol{S}}_e^n}}{\partial\eta_i^n}\right|_{\boldsymbol{F}}=\left.\frac{\partial\overline{\hat{\boldsymbol{C}}_e^n}}{\partial\eta_i^n}\right|_{\boldsymbol{F}}:\boldsymbol{E}_e^n+\overline{\hat{\boldsymbol{C}}_e^n}:\left.\frac{\partial\boldsymbol{E}_e^n}{\partial\eta_i^n}\right|_{\boldsymbol{F}}; \tag{B.45}$$

$$\left.\frac{\partial\boldsymbol{E}_e^n}{\partial\eta_i^n}\right|_{\boldsymbol{F}}=-sym\left(\boldsymbol{C}_e^n\cdot\frac{\partial\overline{\boldsymbol{F}}_t^n}{\partial\eta_i^n}\cdot\overline{\boldsymbol{F}}_t^{n-1}\right);\qquad\overline{\left.\frac{\partial\psi_e^n}{\partial\eta_i^n}\right|_{\boldsymbol{F}_e}}=0.5\boldsymbol{E}_e^n:\overline{\left.\frac{\partial\hat{\boldsymbol{C}}_e^n}{\partial\eta_i^n}\right|_{\boldsymbol{F}_e}}:\boldsymbol{E}_e^n; \tag{B.46}$$

$$\left.\frac{\partial\overline{\psi}_e^n}{\partial\eta_i^n}\right|_{\boldsymbol{F}_e}=0.5\boldsymbol{E}_e^n:\left.\frac{\partial\overline{\hat{\boldsymbol{C}}_e^n}}{\partial\eta_i^n}\right|_{\boldsymbol{F}_e}:\boldsymbol{E}_e^n;\qquad\left.\frac{\partial\overline{\psi}_e^n}{\partial\eta_i^n}\right|_{\boldsymbol{F}}=0.5\boldsymbol{E}_e^n:\left.\frac{\partial\overline{\hat{\boldsymbol{C}}_e^n}}{\partial\eta_i^n}\right|_{\boldsymbol{F}}:\boldsymbol{E}_e^n+\boldsymbol{E}_e^n:\overline{\hat{\boldsymbol{C}}_e^n}:\left.\frac{\partial\boldsymbol{E}_e^n}{\partial\eta_i^n}\right|_{\boldsymbol{F}};\quad\text{and} \tag{B.47}$$

$$\frac{\partial}{\partial\eta_k^n}\left(\overline{\left.\frac{\partial\psi_e^n}{\partial\eta_i^n}\right|_{\boldsymbol{F}_e}}\right)_{\boldsymbol{F}}=0.5\boldsymbol{E}_e^n:\frac{\partial}{\partial\eta_k^n}\left(\overline{\left.\frac{\partial\hat{\boldsymbol{C}}_e^n}{\partial\eta_i^n}\right|_{\boldsymbol{F}_e}}\right)_{\boldsymbol{F}}:\boldsymbol{E}_e^n+\boldsymbol{E}_e^n:\overline{\left.\frac{\partial\hat{\boldsymbol{C}}_e^n}{\partial\eta_i^n}\right|_{\boldsymbol{F}_e}}:\left.\frac{\partial\boldsymbol{E}_e^n}{\partial\eta_k^n}\right|_{\boldsymbol{F}}. \tag{B.48}$$

While deriving Eq. (B.44), we have differentiated $\boldsymbol{P}_e^n=\overline{J}_t^n\boldsymbol{F}^n\cdot\overline{\boldsymbol{F}}_t^{n-1}\cdot\hat{\boldsymbol{S}}_e^n\cdot\overline{\boldsymbol{F}}_t^{n-T}$ (obtained using $\boldsymbol{P}=\boldsymbol{F}\cdot\boldsymbol{S}$ and $\boldsymbol{P}=J\boldsymbol{\sigma}\cdot\boldsymbol{F}^{-T}$ [57]) with respect to η_k^n, and for Eq. (B.46)$_1$ we have differentiated Eq. (2.3)$_2$ and used Eq. (2.2).

Appendix C. Supplementary data

Supplementary material related to this article can be found online at https://doi.org/10.1016/j.cma.2018.08.006.

References

[1] N. Provatas, K. Elder, Phase-Field Methods in Materials Science and Engineering, Wiley-VCH, Weinheim, 2010.
[2] S.M. Allen, J.W. Cahn, A microscopic theory for antiphase boundary motion and its application to antiphase domain coarsening, Acta Mater. 27 (1979) 1085–1095.
[3] W.J. Boettinger, J.A. Warren, C. Beckermann, A. Karma, Phase-field simulation of solidification, Annu. Rev. Mater. Res. 32 (2002) 163–194.
[4] I. Steinbach, Phase-field models in materials science, Modelling Simul. Mater. Sci. Eng. 17 (2009) 073001.
[5] I. Steinbach, F. Pezzolla, B. Nestler, M. Seeßelberg, R. Prieler, G.J. Schmitz, J.L.L. Rezende, A phase field concept for multiphase systems, Physica D 94 (1996) 135–147.
[6] R. Folch, M. Plapp, Quantitative phase-field modeling of two-phase growth, Phys. Rev. E 72 (2005) 011602.
[7] J. Rosam, P.K. Jimack, A. Mullis, A fully implicit fully adaptive time and space discretisation method for phase-field simulation of binary alloy solidification, J. Comput. Phys. 225 (2007) 1271–1287.
[8] A. Basak, V.I. Levitas, Phase field study of surface-induced melting and solidification from a nanovoid: Effect of dimensionless width of void surface and void size, Appl. Phys. Lett. 112 (2018) 201602.
[9] D.M. Anderson, G.B. McFadden, A.A. Wheeler, A phase-field model with convection: sharp-interface asymptotics, Physica D 151 (2001) 305–331.
[10] J. Slutsker, K. Thornton, A.L. Roytburd, J.A. Warren, G.B. McFadden, Phase field modeling of solidification under stress, Phys. Rev. B 74 (2006) 014103.
[11] H. Garcke, B. Nestler, B. Stoth, A multiphase field concept: Numerical simulations of moving phase boundaries and multiple junctions, Phys. Rev. B 78 (2008) 024113.
[12] L.Q. Chen, Phase-field models for microstructure evolution, Annu. Rev. Mater. Res. 32 (2002) 113–140.
[13] R. Kobayashi, J.A. Warren, Modeling the formation and dynamics of polycrystals in 3D, Physica A 356 (2005) 127–132.
[14] N. Moelans, B. Blanpain, P. Wollants, Quantitative analysis of grain boundary properties in a generalized phase field model for grain growth in anisotropic systems, Phys. Rev. B 78 (2008) 024113.
[15] S.G. Kim, D.I. Kim, W.T. Kim, Y.B. Park, Computer simulations of two-dimensional and three-dimensional ideal grain growth, Phys. Rev. E 74 (2006) 061605.
[16] G.I. Tóth, T. Pusztai, L. Gránási, Consistent multiphase-field theory for interface driven multidomain dynamics, Phys. Rev. B 92 (2015) 184105.
[17] A.Y. Woldman, C.M. Landis, Phase-field modeling of ferroelectric to paraelectric phase boundary structures in single-crystal barium titanate, Smart Mater. Struct. 25 (2016) 035033.
[18] A. Artemev, J. Slutsker, A.L. Roytburd, Phase field modeling of self-assembling nanostructures in constrained films, Acta Mater. 53 (2005) 3425–3432.
[19] M. Mamivand, M.A. Zaeem, H.E. Kadiri, A review on phase field modeling of martensitic phase transformation, Comput. Mater. Sci. 77 (2013) 304–311.
[20] V.I. Levitas, A.M. Roy, D.L. Preston, Multiple twinning and variant-variant transformations in martensite: Phase-field approach, Phys. Rev. B 88 (2013) 054113.
[21] V.I. Levitas, A.M. Roy, Multiphase phase field theory for temperature- and stress-induced phase transformations, Phys. Rev. B 91 (2015) 174109.
[22] J.C.H. Lei, L.J. Li, Y.C. Shu, J.Y. Li, Austenite-martensite interface in shape memory alloys, Appl. Phys. Lett. 96 (2010) 141910.
[23] Y.M. Jin, A. Artemev, A.G. Khachaturyan, Three-dimensional phase field model of low-symmetry martensitic transformation in polycrystal: Simulation of ζ_2 martensite in AuCd alloys, Acta Mater. 49 (2001) 2309–2320.
[24] F.E. Hildebrand, C. Miehe, A phase field model for the formation and evolution of martensitic laminate microstructure at finite strains, Phil. Mag. 92 (2012) 1–41.
[25] K. Tůma, S. Stupkiewicz, Phase-field study of size-dependent morphology of austenite-twinned martensite interface in CuAlNi, Int. J. Solids Struct. 97–98 (2016) 89–100.
[26] K. Tůma, S. Stupkiewicz, H. Petryk, Size effects in martensitic microstructures: Finite-strain phase field model versus sharp-interface approach, J. Mech. Phys. Solids 95 (2016) 284–307.
[27] J.D. Clayton, J. Knap, A phase field model of deformation twinning: Nonlinear theory and numerical simulations, Physica D 240 (2011) 841–858.
[28] J.D. Clayton, J. Knap, Phase field modeling of twinning in indentation of transparent crystals, Model. Simul. Mater. Sci. Eng. 19 (2011) 085005.
[29] V.I. Levitas, Phase field approach to martensitic phase transformations with large strains and interface stresses, J. Mech. Phys. Solids 70 (2014) 154–189.
[30] V.I. Levitas, D.L. Preston, Three-dimensional Landau theory for multivariant stress-induced martensitic phase transformations. I. Austenite ↔ Martensite, Phys. Rev. B 66 (2002) 134206.

[31] V.I. Levitas, Phase-field theory for martensitic phase transformations at large strains, Int. J. Plast. 49 (2013) 85–118.
[32] A. Artemev, Y. Wang, A.G. Khachaturyan, Three-dimensional phase field model and simulation of martensitic transformation in multilayer systems under applied stresses, Acta Mater. 48 (2000) 2503–2518.
[33] A. Artemev, Y. Jin, A.G. Khachaturyan, Three-dimensional phase field model of proper martensitic transformation, Acta Mater. 49 (2001) 1165–1177.
[34] D.J. Seol, S.Y. Hu, Y.L. Li, L.Q. Chen, K.H. Oh, Computer simulation of martensitic transformation in constrained films, Mater. Sci. Forum 408–412 (2002) 1645–1650.
[35] H.M. Paranjape, S. Manchiraju, P.M. Anderson, A phase field-Finite element approach to model the interaction between phase transformations and plasticity in shape memory alloys, Int. J. Plast. 80 (2016) 1–18.
[36] V.I. Levitas, M. Javanbakht, Interaction between phase transformations and dislocations at the nanoscale.Part 1. General phase field approach, J. Mech. Phys. Solids 82 (2015) 287–319.
[37] J. Kundin, D. Raabe, H. Emmerich, A phase-field model for incoherent martensitic transformations including plastic accommodation processes in the austenite, J. Mech. Phys. Solids 59 (2011) 2082–2102.
[38] K. Bhattacharya, Microstructure of Martensite: Why It Forms and how It Gives Rise To the Shape-Memory Effect, Oxford University Press, Oxford, 2004.
[39] M. Pitteri, G. Zanzotto, Continuum Models for Phase Transitions and Twinning in Crystals, Chapman & Hall/CRC, Boca Raton, 2003.
[40] T. Waitz, K. Tsuchiya, T. Antretter, F.D. Fischer, Phase transformations of nanocrystalline martensitic materials, MRS Bull. 34 (2009) 814–821.
[41] M.E. Gurtin, A. Murdoch, A continuum theory of elastic material surfaces, Arch. Ration. Mech. Anal. 57 (1975) 291–323.
[42] J. Diao, K. Gall, M.L. Dunn, Surface-stress-induced phase transformation in metal nanowires, Nature Mater. 2 (2003) 656–660.
[43] S. Li, X. Ding, J. Li, X. Ren, J. Sun, E. Ma, T. Lookman, Inverse martensitic transformation in Zr nanowires, Phys. Rev. B 81 (2010) 245433.
[44] V.I. Levitas, M. Javanbakht, Surface tension and energy in multivariant martensitic transformations: Phase-field theory,simulations, and model of coherent interface, Phys. Rev. Lett. 105 (2010) 165701.
[45] A. Basak, V.I. Levitas, Nanoscale multiphase phase field approach for stress- and temperature-induced martensitic phase transformations with interfacial stresses at finite strains, J. Mech. Phys. Solids 113 (2018) 162–196.
[46] A.V. Idesman, V.I. Levitas, D.L. Preston, J.Y. Cho, Finite element simulations of martensitic phase transitions and microstructure based on strain softening model, J. Mech. Phys. Solids 53 (2005) 495–523.
[47] N. Moelans, F. Wendler, B. Nestler, Comparative study of two phase-field models for grain growth, Comput. Mater. Sci. 46 (2009) 479–490.
[48] A. Vidyasagar, W.L. Tan, D.M. Kochmann, Predicting the effective response of bulk polycrystalline ferroelectric ceramics via improved spectral phase field methods, J. Mech. Phys. Solids 106 (2017) 133–151.
[49] J.Y. Cho, A.V. Idesman, V.I. Levitas, T. Park, Finite element simulations of dynamics of multivariant martensitic phase transitions based on Ginzburg-Landau theory, Int. J. Solids Struct. 49 (2012) 1973–1992.
[50] V.A. Levin, V.I. Levitas, K.M. Zingerman, E.I. Freiman, Phase-field simulation of stress-induced martensitic phase transformations at large strains, Int. J. Solids Struct. 50 (2013) 2914–2928.
[51] V.I. Levitas, V.A. Levin, K.M. Zingerman, E.I. Freiman, Displacive phase transitions at large strains: Phase-field theory and simulations, Phys. Rev. Lett. 103 (2009) 025702.
[52] H. She, Y. Liu, B. Wang, D. Ma, Finite element simulation of phase field model for nanoscale martensitic transformation, Comput. Mech. 52 (2013) 949–958.
[53] A. Basak, V.I. Levitas, Interfacial stresses within boundary between martensitic variants: analytical and numerical finite strain solutions for three phase field models, Acta Mater. 139 (2017) 174–187.
[54] C.S. Jog, The explicit determination of the logarithm of a tensor and its derivatives, J. Elasticity 93 (2008) 141–148.
[55] C.S. Jog, Foundations and Applications of Mechanics. Volume I: Continuum Mechanics, Narosa, New Delhi, 2007.
[56] G.A. Holzapfel, Nonlinear Solid Mechanics: A Continuum Approach for Engineering, John Wiley & Sons Ltd, Sussex, 2000.
[57] P. Wriggers, Nonlinear Finite Element Methods, Springer-Verlag, Heidelberg, 2008.
[58] O.C. Zienkiewicz, R.L. Taylor, The Finite Element Method: Volume 2- Solid Mechanics, Butterworth-Heinemann, Woburn, 2000.
[59] J. Bonet, R.D. Wood, Nonlinear Continuum Mechanics for Finite Element Analysis, Cambridge University Press, Cambridge, 2008.
[60] O.C. Zienkiewicz, R.L. Taylor, The Finite Element Method: Volume 1- the Basis, Butterworth-Heinemann, Woburn, 2000.
[61] W. Hundsdorfer, J. Verwer, Numerical Solution of Time-Dependent Advection-Diffusion-Reaction Equations, Springer, Heidelberg, 2003.
[62] P. Neff, Local existence and uniqueness for quasistatic finite plasticity with grain boundary relaxation, Quart. Appl. Math. LXIII (2005) 88–116.
[63] A. Raoult, Non-polyconvexity of the stored energy function of a Saint Venant-Kirchhoff material, Apl. Mat. 31 (1986) 417–419.
[64] D.M. Kochmann, K. Hackl, The evolution of laminates in finite crystal plasticity: a variational approach, Contin. Mech. Thermodyn. 23 (2011) 63–85.
[65] A. Vidyasagar, A.D. Tutcuoglu, D.M. Kochmann, The evolution of laminates in finite crystal plasticity: a variational approach, Comput. Methods Appl. Mech. Engrg. 335 (2018) 584–609.
[66] P.C. Clapp, C.S. Besquart, Y. Shao, Y. Zhao, J.A. Rifkin, Transformation toughening explored via molecular dynamics and Monte Carlo simulations, Modell. Simul. Mater. Sci. Eng. 2 (1994) 551.
[67] V.I. Levitas, D.L. Preston, Three-dimensional Landau theory for multivariant stress-induced martensitic phase transformations. II. Multivariant phase transformations and stress-space analysis, Phys. Rev. B 66 (2002) 134207.
[68] F.D. Fischer, J. Svoboda, K. Hackl, Modelling the kinetics of a triple junction, Acta Mater. 60 (2012) 4704–4711.

[69] W. Bangerth, D. Davydov, T. Heister, L. Heltai, G. Kanschat, M. Kronbichler, M. Maier, B. Turcksin, D. Wells, The deal.II library, version 8.4, J. Numer. Math. 24 (2016).
[70] A. Basak, V.I. Levitas, Supplementary material for Finite element procedure and simulations for a multiphase phase field approach to martensitic phase transformations at large strains and with interfacial stresses.
[71] J.M. Ball, R.D. James, Fine phase mixtures as minimizers of energy, Arch. Ration. Mech. Anal. 100 (1987) 13–52.
[72] M. Giaquinta, S. Hildebrandt, Calculus of Variations I, Springer, Heidelberg, 2004.
[73] V.I. Levitas, Phase field approach for stress- and temperature-induced phase transformations that satisfies lattice instability conditions. Part 1. General theory, Int. J. Plast. 106 (2018) 164–185.